

AD-A258 973



AFIT/GAE/ENY/92D-21

1

DTIC
ELECTE
JAN 6 1993
S c D

CHARACTERIZATION OF STALL INCEPTION IN
HIGH-SPEED SINGLE-STAGE COMPRESSORS

THESIS

Keith M. Boyer, Captain, USAF

AFIT/GAE/ENY/92D-21

Approved for public release; distribution unlimited

012225
93-00157
151

93 1 04 017

CHARACTERIZATION OF STALL INCEPTION IN
HIGH-SPEED SINGLE-STAGE COMPRESSORS

THESIS

Presented to the Faculty of the School of Engineering
of the Air Force Institute of Technology
Air University
in Partial Fulfillment of the
Requirements for the Degree of
Master of Science in Aeronautical Engineering

Keith M. Boyer, B.S.

Captain, USAF

November 1992

Accession For	
NTIS GRA&I	<input checked="checked" type="checkbox"/>
DTIC TAB	<input type="checkbox"/>
Unannounced	<input type="checkbox"/>
Justification	
By _____	
Distribution/	
Availability Codes	
Dist	Avail and/or Special
A-1	

Approved for public release; distribution unlimited

DTIC QUALITY INSPECTED 5

ACKNOWLEDGEMENTS

I am indebted to many people for the success of this research. Many thanks must go to my advisor, Professor Paul King, for not only his insights and suggestions, but also for allowing me the freedom to attack the research in my own manner (indeed, more than once that manner had to be readjusted). Professor King also played a big role in my selection to be an instructor at the USAF Academy; for this, I will be eternally grateful. Additionally, I am thankful for the suggestions and comments received from the other members of my thesis committee, Professor William Elrod and Captain Thomas Buter.

For their contributions, Dr Bill Copenhaver and the entire Compressor Research Group (WL/POTX) deserve to be at the start of a new paragraph. Not only did they ensure timely gathering of the test data, but they also went above and beyond the call of duty in many aspects of the research - from improving my understanding of the facility operation, to steady-state data processing, to fierce technical exchanges, etc. I am especially grateful to Bill for being an advisor, colleague, friend, and all-around beacon of light over the 5-plus years we've known each other. Special thanks must also go to Steve Puterbaugh and Derek Sellin (pronounced Sa-lean) for showing genuine interest in the work and helping me with many of the logistical aspects of this report. Derek was my office-mate during my time spent in Building 450 and had to listen to numerous periodic updates regarding the status of the report (as well as the status of my house for sale; which by the way is still available as of the writing of this thesis).

Charlotte Coleman (645C-CSG/SCSA) of the Scientific and Engineering Applications Section, Communications-Computer Systems Group also deserves special recognition for her help in digitizing the large amounts of data generated during this research. The data were sneaker-netted over to Building 676 on magnetic tape and Charlotte and her Real-Time Simulation Support Facility took it from there. Charlotte and I set goals and we achieved them all, in spite of the problems with the time code and tape system.

I am also grateful to Professors Alan Epstein and Jim Paduano of MIT for their insights and suggestions. Special thanks to Professor Paduano for copies of the MATLAB scripts, sample data set, and tutoring which allowed me to have my analysis package all ready and waiting for the acquired data.

Finally, and most important, a special thanks to my family. To my Mom and Dad (Loretta and Ken) for instilling in me values that have served me well throughout my Air Force career and personal life. Also, to my two daughters, Jennifer and Kelly, who constantly remind me that there's so much more to life than stall behavior in compressors. And of course, to my best friend and wife, Joyce, who is a constant source of support and inspiration. It is to Joyce that I dedicate this thesis.

TABLE OF CONTENTS

Acknowledgements.....	i
List of Tables.....	v
List of Figures.....	vi
Symbols/Abbreviations.....	x
Abstract.....	xi
1.0 INTRODUCTION.....	1
1.1 Motivation.....	1
1.2 Compressor Performance - Surge and Rotating Stall.....	3
1.3 Stability Audit - Stall Margin.....	6
1.4 Intent of Current Work.....	8
2.0 BACKGROUND.....	11
2.1 Preliminary Remarks.....	11
2.2 Early Works.....	12
2.2.1 Basic Mechanism of Rotating Stall.....	13
2.2.2 Linearized Theories of Stall Inception.....	14
2.3 Recent Works.....	16
2.3.1 Modal Waves as a Stall Inception Indication...	16
2.3.2 Finite Cells as a Stall Inception Indication..	20
2.3.3 Active Control Experiments.....	21
2.4 Potential Factors Affecting Stall Precursor.....	22
3.0 TEST APPARATUS.....	25
3.1 Facility Description.....	25

TABLE OF CONTENTS (continued)

3.2	Test Vehicle and Designs Tested.....	26
3.2.1	Fan Rig Description.....	26
3.2.2	Rotor Designs Tested.....	27
3.3	Instrumentation.....	28
3.3.1	Test Facility Instrumentation.....	28
3.3.2	Compressor Instrumentation.....	29
3.3.3	Calibration and Measurement Uncertainty.....	30
3.3.4	Data Acquisition System (DAS).....	31
3.3.5	Unsteady Pressure Measurement.....	31
4.0	TEST PROCEDURE AND DATA PROCESSING OF UNSTEADY PRESSURES..	34
4.1	Test Procedure.....	34
4.2	Data Sampling.....	35
4.3	Additional Digital Filtering.....	37
4.4	Forms of Data Presentation.....	39
4.4.1	Filtered Raw Pressure Signals.....	39
4.4.2	Spatial Fourier Coefficients.....	40
4.4.3	Power Spectral Densities.....	42
5.0	RESULTS AND DISCUSSION.....	43
5.1	Introductory Remarks.....	43
5.2	Low Frequency Planar Oscillations.....	43
5.3	Analysis of Results.....	45
5.3.1	60% Design Speed.....	47

TABLE OF CONTENTS (continued)

5.3.2	70% Design Speed.....	48
5.3.3	80, 90, and 100% Design Speed.....	51
5.4	Stall Warning Time.....	55
5.5	Effect of Speedline Characteristic on Stall Precursor.....	56
5.6	Effect of Shock Waves on Stall Precursor.....	58
5.7	Comparison With Previous Investigations.....	60
6.0	CONCLUSIONS AND RECOMMENDATIONS.....	63
6.1	Summary.....	63
6.2	Conclusions.....	63
6.3	Recommendations.....	66
7.0	REFERENCES.....	69
	Tables.....	72
	Figures.....	77
	Appendix Fourier Analysis.....	139
	Vita.....	143

LIST OF TABLES

3.1	Facility Operating Parameters.....	72
3.2	Rotor/Stator Design Features.....	73
3.3	Steady-State Uncertainty Analysis.....	74
3.4	Kulite Performance Characteristics.....	75
3.5	Kulite Calibration Data.....	75
4.1	Frequency Range of Band-Pass Filters.....	76
5.1	Stall Warning Time.....	76

LIST OF FIGURES

1.1	Schematic of compressor map.....	77
1.2	Compressor instabilities - surge and rotating stall.....	78
1.3	Compressor stability audit.....	79
1.4	Active compressor stabilization.....	80
2.1	Emmons model of rotating stall.....	81
2.2	Typical compressor stability criterion.....	81
2.3	Modal wave view of compressor instabilities.....	82
2.4	Spatial Fourier coefficient analysis of modal waves [28].....	83
2.5	Coupling between modal waves and finite cells [7].....	84
2.6	Stall inception via finite cells [7].....	84
3.1	Compressor Aerodynamic Research Laboratory (CARL).....	85
3.2	Schematic of 2000-hp test facility.....	86
3.3	Cross-section of compressor rig [29].....	86
3.4	Rotor 4 installed.....	87
3.5	Rotor 6 installed.....	88
3.6	Close-up of Rotor 4 showing Kulite location.....	89
3.7	Close-up of Rotor 6 showing Kulite location.....	90
3.8	Rotor tip clearances.....	91
3.9	Compressor instrumentation.....	92
3.10	Vane leading edge and discharge plane rake instrumentation [29].....	93
3.11	CARL control room.....	94
3.12	Kulite location and signal path.....	95
4.1	Steady-state map of Rotor 4.....	96

LIST OF FIGURES (continued)

4.2	Steady-state map of Rotor 6.....	97
4.3a	Transient behavior of an isolated airfoil.....	98
4.3b	Transient behavior of a compressor stage.....	98
4.4	Characteristics of Butterworth analog filter.....	99
4.5	Spectrum from Kulite #2 - no additional filtering.....	100
4.6	Spectrum from Kulite #2 - band-pass filtered.....	100
4.7	Analyses used for stall inception characterization.....	101
4.8	Pressure traces showing rotating waves.....	102
4.9	Illustration of SFC #1 analysis - 90% speed transient...	103
4.10	PSD of an SFC - 90% speed transient.....	104
5.1	Low frequency planar oscillations - 60% speed, Rotor 4..	105
5.2	Surge-like instability at 80% speed, Rotor 4.....	106
5.3	Hypothetical behavior of compressor during transient to stall with planar oscillations.....	107
5.4	Pressure traces (no additional filtering) - 60% speed transient, Rotor 4.....	108
5.5	Amplitude and phase of SFC #1 - 60% speed, Rotor 4.....	109
5.6	Comparison of PSD of SFC #1 at two steady throttle positions - 60% speed, Rotor 4.....	110
5.7	Pressure traces during 70% speed transient, Rotor 4.....	111
5.8	Stall inception at 70% speed, Rotor 4.....	112
5.9	First and second spatial Fourier modes - 70% speed, Rotor 4.....	113
5.10	Spectra of SFC #1 transient data at 70% speed, Rotor 4..	114
5.11	Spectra of SFC #2 transient data at 70% speed, Rotor 4..	115
5.12	SFC #1 of 70% speed transient data, Rotor 6.....	116

LIST OF FIGURES (continued)

5.13	Pressure traces - 80% speed transient, Rotor 4.....	117
5.14	Stall inception at 80% speed, Rotor 4.....	117
5.15	Amplitude and phase of SFC #1 - 80% speed, Rotor 4.....	118
5.16	PSD of SFC #1 using transient data set up to stall - 80% speed, Rotor 4.....	119
5.17	Pressure traces during 90% speed transient, Rotor 4.....	120
5.18	Stall inception at 90% speed, Rotor 4.....	120
5.19	SFC #1 amplitude and phase - 90% speed, Rotor 4.....	121
5.20	SFC #1 amplitude and phase - 90% speed, Rotor 6.....	121
5.21	PSD of SFC #1 using transient data set up to stall - 90% speed, Rotor 6.....	122
5.22	Pressure traces during 100% speed transient, Rotor 6....	123
5.23	Stall inception at 100% speed, Rotor 6.....	123
5.24	SFC #1 amplitude and phase - 100% speed, Rotor 6.....	124
5.25	PSD of SFC #1 using different lengths of transient data set - 100% speed, Rotor 6.....	125
5.26	Example of smoothed SFC #1 phase data - 90% speed.....	126
5.27	Slope of SFC #1 phase - 70% speed, Rotor 4.....	127
5.28	Slope of SFC #1 phase - 70% speed, Rotor 6.....	128
5.29	Slope of SFC #1 phase - 80% speed, Rotor 4.....	129
5.30	Slope of SFC #1 phase - 80% speed, Rotor 6.....	130
5.31	Slope of SFC #1 phase - 90% speed, Rotor 4.....	131
5.32	Slope of SFC #1 phase - 90% speed, Rotor 6.....	132
5.33	Slope of SFC #1 phase - 100% speed, Rotor 4.....	133
5.34	Slope of SFC #1 phase - 100% speed, Rotor 6.....	134

LIST OF FIGURES (continued)

5.35	Speedline characteristics of Rotor 4 extended to show transient stall line observed during testing.....	135
5.36	Speedline characteristics of Rotor 6 extended to show transient stall line observed during testing.....	135
5.37	Effect of local speedline slope on stall warning time...	136
5.38	Shock structure in transonic rotors at near-stall.....	137
5.39	Steady-state speedline characteristics of both rotors...	138

SYMBOLS/ABBREVIATIONS

ADP	- Aerodynamic design point
AFB	- Air Force Base
A_c	- equivalent compressor area (ft ²)
a	- speed of sound (ft/s)
CARL	- Compressor Aerodynamic Research Facility
CI	- confidence interval
C_k	- spatial Fourier coefficient
DAS	- data acquisition system
DC	- direct current
DFT	- discrete Fourier transform
deg	- degrees
FIR	- finite impulse response
FFT	- fast Fourier transform
FM	- frequency modulation
k	- Fourier mode or wave harmonic
L_c	- equivalent compressor length (ft)
N	- rotor speed (rpm)
N_c	- corrected rotor speed ($N_c = N/\sqrt{\theta}$)
PBS	- parametric blade studies
P_d	- differential pressure (psi)
PSD	- power spectral density
P_s	- static pressure (psia or psig)
P_t	- total pressure (psia or psig)
rad	- radians
revs	- revolutions
rpm	- rotations per minute
SFC	- spatial Fourier coefficient (same as C_k)
SM	- stall margin
T_t	- total temperature (F or R)
t	- time
V	- volts
V_p	- discharge plenum volume (ft ³)
W	- mass flow rate (lbm/s)

Greek

$\delta\phi$	- non-axisymmetric component of flow coefficient
θ	- circumferential position (rad or deg); ratio of inlet total temperature to 518.69 R
σ	- growth rate or damping of wave (1/s)
ϕ	- flow coefficient
$\bar{\phi}$	- mean component of flow coefficient
ω	- wave frequency (rad/s); Helmholtz frequency (Hz)

ABSTRACT

Two single-stage, transonic compressor designs were tested under various undistorted operating conditions to characterize the process leading up to aerodynamic stall. In addition to extensive instrumentation to measure the compressor steady performance, the rig case was instrumented with eight high-response pressure transducers equally spaced around the annulus for stall development detection. High-response measurements were low-pass filtered and both spatially and temporally analyzed using discrete Fourier techniques.

At all speeds tested for both designs, stall inception was characterized by growth of a small amplitude rotating wave. The waves did not grow significantly until just prior to the instability, when exponential growth into fully-developed rotating stall occurred very rapidly, within 6-10 rotor revolutions. The amount of time the rotating waves could be detected prior to stall varied considerably with compressor operating condition and was largely dependent on the local slope of the compressor speedline characteristics. Stall warning times ranged from less than one-tenth of a second to more than two seconds for the same machine operated at different high speeds. The influence of compressibility effects are also discussed.

1.0 INTRODUCTION

1.1 Motivation

The search for an incipient stall signal in aircraft gas turbine engine compressors is not new. The interest is primarily motivated by a desire to actively control compressor aerodynamic instabilities (stall). Because of the need to avoid these instabilities, substantial stall margin (or stability margin or surge margin) is designed into fan and compressor components. The margin is required for the engine to maintain adequate performance under the most severe aircraft engine transients and flight conditions. As a result, component performance is sacrificed at more favorable engine operating conditions. A reliable indicator of an impending instability (stall precursor), if detected with sufficient warning time, would allow for active controls to take action to avoid or suppress the stall. In its crudest form, this active stall control would use bleed air, variable blades, and/or fuel control to back away from the instability. In a more elaborate form, compressor unsteady performance would be controlled to provide a dynamic compressor stabilization. With this scheme, stall margin would be added only for the duration needed and amount required to maintain suitable engine performance over the particular transient encountered.

Active stall control offers the potential for significant reductions in current stall margin requirements. Consequently,

substantial increases in fan and compressor performance and reductions in component weight would be expected. This translates into increased engine thrust-to-weight and reduced specific fuel consumption. Also, improvements in engine operability and durability would be likely as current control schemes could be designed to be less restrictive (i.e., greater throttle movement, fewer afterburner restrictions), and fewer compressor stalls encountered.

If any or all of the benefits described above are to be realized, the key is the existence and detection of an accurate and robust (able to be detected under mild and severe operating conditions) stall precursor signal. In the 1960's, limitations of hydromechanical controls prevented any practical use of a stall precursor signal even if one could have been shown to exist. Stall control schemes have generally relied on detecting the presence of stall (rather than a stall precursor), then controlling some variable geometry feature of the compressor to lower the operating point. Ludwig and Nenni [1] demonstrated such a scheme on a turbojet engine and met with only limited success, largely due to insufficient warning time prior to the instability. The lack of adequate stall warning time necessitated the use of large control forces to move the compressor operating point.

Recent investigations by McDougall, et al. [2] and Garnier, et al. [3] have identified small amplitude rotating waves (modal waves) as a potential stall precursor. In cases where the pre-

stall waves have been shown to exist, signals have been detected much sooner than previous schemes, thus offering potential for an active control system to take action. Because of the substantial benefits already mentioned, these recent works have generated a lot of interest in both the research and jet engine manufacturing communities (Aviation Week [4], Hosny, et al [5], and Paduano, et al [6]). Although results to date have been promising, several key issues must be resolved, namely, the generality and robustness of the rotating waves. Indeed, a recent investigation by Day [7] indicated that modal waves were not always present prior to stall, and when present, did not necessarily show a strong coupling to the stall formation process. Day [7] suggested it was the formation and subsequent growth of finite stall cells (nonlinear) that governed the stall inception process. The works of McDougall, et al. [2], Garnier, et al. [3], and Day [7] are discussed in more detail in Chapter 2.0.

1.2 Compressor Performance - Surge and Rotating Stall

As one of the major components of gas turbine engines (the others being the inlet, combustor, turbine, and nozzle), the compressor develops some or all of the pressure rise required by the system thermodynamic cycle. The compression system (fan and compressor) must operate stably and with high efficiency over the entire engine performance envelope, otherwise, engine operability will be compromised. Overall performance is typically displayed on a compressor map, as shown in Fig. 1.1.

The compressor operating region is bounded on the high flow side by blade passage choking and on the low flow side by blade and endwall stalling. Note that peak pressure rise over the useful operating range of the compressor occurs right at the stall line. This behavior is characteristic of most machines and explains the desire to reduce stall margin requirements (discussed in section 1.3). Flow breakdown (stall) occurs to the left of the stall line (or surge line) and manifests itself as either of two distinct phenomena - surge or rotating stall.

Surge is a violent planar dynamic instability characterized by large amplitude oscillations in mass flow and pressure (Fig. 1.2). The frequencies of the oscillations are governed by the compressor and inlet and exit (combustor) volumes, and are usually in the three to fifteen hertz range. Because of the high energy levels required to sustain the cycles, surge is encountered at high compressor speeds (above engine idle). Most surges are self-clearing, provided the initial disturbance has been removed.

Rotating stall is a highly three-dimensional localized event in which one or more packets of stalled air (stall cells) propagate circumferentially around the compressor at speeds between twenty and seventy percent of rotor speed (Fig. 1.2). The circumferential extent of the stall cells can range from only a few blade passages to over 180 degrees of the annulus. The cells can be full or part span and may or may not cover the full axial extent of the compressor. Rotating stalls can be

classified as abrupt or progressive, in relation to the performance behavior as viewed on a compressor map. Figure 1.2b is schematically representative of an abrupt stall, evidenced by the sudden discontinuous decrease in performance once stall occurs. Progressive stall is characterized by a smooth, continuous decrease in performance, typical of a part-span stall which grows slowly in circumferential and radial extent (Greitzer [12]). Both types of rotating stall (abrupt and progressive) were observed in the current set of experiments.

Rotating stall is characterized by quasi-steady (globally stable in a mass-averaged sense) performance at a reduced flow rate and pressure rise. It is generally accompanied by recovery hysteresis; that is, once rotating stall is fully developed, recovery to normal operation requires a significant increase in exit throttle area (applicable in test cells; note in engines, bleed flow, variable vanes and/or fuel control must be used) beyond that at which stall inception occurred (Fig. 1.2b). Extensive hysteresis can prevent recovery altogether, thus leading to a "hung" stall. This condition has become known as stagnation or non-recoverable stall.

In aircraft gas turbine engines, surge is the predominant compressor instability encountered. However, continuous surge cycles (non-clearing) result in decreasing rotor speed which can cause the instability to degenerate into a rotating stall and possible non-recoverable condition (Benrey [8]). In either case, consequences are damaging and can be severe. Both surge and

rotating stall lead to large vibratory stresses in the compressor blading and possible turbine inlet overtemperature.

Additionally, the reduced performance levels associated with rotating stall can result in an engine cycle that is not self-sustaining.

It is worth mentioning that most engine compressor stalls are caused from a highly transient event (hard afterburner light, severe inlet distortion from a sudden maneuver, hot gas ingestion from an armament firing, etc.). In a compressor rig test, stall is typically induced by increasing the backpressure via a downstream throttle (as was done in the current investigation). Thus, from a practical standpoint, it is useful to study the effects of different throttle closure rates on the stalling behavior of compressor rigs (faster rates more closely associated with actual engine stalls). In the present experiments, only one throttle rate was available (discussed in detail in section 4.1). The effects of throttle closure rate are discussed further in section 2.4.

1.3 Stability Audit - Stall Margin

The need to avoid the severe consequences of rotating stall and surge imposes a significant dilemma on the engine designer; the engine must optimally satisfy the conflicting requirements of high thrust, low fuel consumption, low weight, long life, low cost, and adequate engine stability. The stability audit (or stackup) is a procedure currently used to establish required

surge margins. Figure 1.3 shows the stability audit items or destabilizing influences that must be included in determining the design stall margin of a high pressure compressor. Many of the factors are not usually present (or not present all at the same time); consequently, the compressor operates with more stability margin than is required. Typical design values of stall margin range from 15-25% (Wisler [9]), defined as

$$SM = \frac{PR_{stall} - PR_{design}}{PR_{design}} \quad (1.1)$$

at a constant flow.

A signal that consistently precedes a stall event (rotating stall or surge) with enough warning time to take action to avoid or suppress the instability could significantly reduce the surge margin requirements of fan and compressor components. Ideally, if a robust stall precursor did exist, active controls would be used to interfere with the unsteady aerodynamic damping of the compressor in a manner that moved the point of instability onset to lower flows. This idea of an actively stabilized stall line was first proposed in the open literature by Epstein, et al.

[10], and is illustrated in Fig. 1.4. In Fig. 1.4, a compressor is allowed to accelerate at a maximum rate (transient operating line) and actually operate to the left of the steady-state stall boundary (net stall line). Once the acceleration is complete, the additional margin is not required and the stall line is returned to the base stall line. Thus, the compressor operating line is raised and adequate stall margin provided only for the

duration and amount needed to maintain stable performance over the transient event. The work of Paduano, et al. [6] and Day [11] are two recent examples of the use of active compressor stabilization.

1.4 Intent of Current Work

The primary objective of the current investigation is to characterize the stall inception behavior in two high-speed, advanced design compressors. Results are intended to provide a sound physical understanding of the stall development process in machines that are typical of those used in current and future aircraft engine applications. It is emphasized that the majority of reported stall investigations performed to date have been carried out on low-speed, low pressure rise machines (compressibility effects are assumed negligible). Questions regarding the applicability of these results to high-speed (compressible) machines must be answered. Thus, the current stall investigation work attempts to provide information that will be useful in assessing this applicability.

The two single-stage rotor designs differ primarily in their amount of leading edge sweep (one has a conventional straight leading edge, the other is swept back). Both were tested at several speeds under various clean inlet (undistorted) operating conditions. In addition to numerous instrumentation to quantify the compressor steady performance, the rig case was instrumented with eight high-response pressure transducers equally spaced

around the annulus for stall development detection. The data were analog recorded, then post-processed as the intent of the current work is to characterize the stall inception behavior, and not to demonstrate a real-time control strategy.

A critical question that must be answered is which process, modal waves or finite cells (last paragraph, section 1.1), dominates the formation of fully developed stall (rotating stall or surge). Resolution of this issue is key if improvements in the modelling of compressor stability are to be realized and the most beneficial approaches to active control defined. The current work focuses on this issue, and in particular addresses the following questions:

(1) What is the relationship between modal waves and finite cells, and is the relationship consistent or does it vary with compressor design, operating condition, etc?

(2) What is the effect of compressor operating condition on the pre-stall indication?

(3) Where precisely on the compressor pressure rise characteristic do the first signs of pre-stall behavior occur? Does the shape of the characteristic affect the pre-stall behavior?

(4) How do the features of the stall inception process in high-speed machines compare to those in low-speed machines?

(5) Are there potential stall warning signs that might be peculiar to high-speed compressors?

Additionally, a whole series of questions regarding the

robustness of the pre-stall indications (influence of distorted flow fields, various throttle rates, etc.) must be addressed, but these are not examined in this work.

2.0 BACKGROUND

2.1 Preliminary Remarks

As noted by Greitzer [12], the subject of axial compressor stall (rotating stall and surge) can be separated conceptually into two main areas:

(1) Stall inception - This area deals with the examination of the basic fluid mechanics associated with the onset of stall. Important aspects include the influence of inlet distortion and rapid throttle transients, the effects of downstream system components, and stability enhancements such as rotor casing treatments and active controls.

(2) Post-stall behavior - In this area, behavior subsequent to the onset of the initial instability is of prime concern. Topics of interest include large amplitude surge oscillations, transient performance into and out of rotating stall, structure of the rotating stall flow field and in-stall operation, and recovery hysteresis extent.

Because of the nature of the current work this literature survey will focus on the first area, stall inception. In particular, those theories and investigations that relate to the two currently popular explanations of stall development, modal waves and finite cells, will be emphasized. Excellent summaries of previous work in the area of post-stall performance are provided by Davis [13], Copenhaver [14], and Gorrell [15].

As was mentioned in section 1.4, the majority of stall

investigations performed to date (both analytical and experimental) have been carried out on low-speed, high aspect ratio machines with limited number of stages (low pressure rise). The theories that have developed from these investigations have been able to add considerable insight into the fluid mechanics of stability onset and stall behavior. However, they have limited use in regards to the high-speed, high pressure ratio aircraft engine applications which are of practical interest. The limitations of the theories are imposed by the assumptions that are inherent in their development, one of the most crucial being incompressible treatment of the flow. The addition of compressibility adds much complexity to the theories, but is essential if practical use is to come from the investigations. The work that has been performed on high-speed compressors has largely been involved with post-stall and recovery behavior. Recent examples (1985-1991) include Davis [13], Copenhaver [14], Gorrell [15], Small and Lewis [16], Hosny and Steenken [17], Boyer and O'Brien [18], [19], and Bonnaure [20]. Of these, only Bonnaure's work [20] focused on the stall inception process through the development of a two-dimensional model of high-speed compressor stability. The present research focuses on an experimental investigation of the stall development process in high-speed, advanced design compressors.

2.2 Early Works

For the purpose of this literature review, work dealing with

stall inception performed prior to 1980 is classified as early. An excellent review of these earlier analyses is provided by Greitzer [12].

2.2.1 Basic Mechanism of Rotating Stall

A simple and still widely used explanation of the mechanism of rotating stall was initially proposed by Emmons, et al [21] and recently applied by Day [7]. Consider a row of blades operating on the verge of stall (large angle of attack) as in Fig. 2.1. If some flow disturbance causes one (or several adjacent) of the blades to momentarily stall, then the flow through that passage will be restricted by the separated boundary layer on the suction side of the stalled blade (blade A of Fig. 2.1). Consequently, the incoming flow will be diverted to surrounding passages, increasing the incidence on blade B and decreasing the incidence on blade C. Thus, the stall will propagate from blade to blade in a direction opposite of rotation relative to the blades, but in the direction of rotation in an absolute reference frame. If the initial flow disturbance is not relieved or is worsened, the stall can grow into a fully developed cell covering more than half of the compressor annulus. Experimental evidence has shown rotating stall cells to propagate anywhere between twenty and seventy percent of the rotational speed of the blades, depending on the size and extent of the cell.

The Emmons model (Fig. 2.1) thus suggests a possible cause

of rotating stall inception; namely, an instability associated with the stalling of a blade passage(s). Day [7] recently used this flow model to offer an explanation of stall inception based on disturbances of a short length scale (a few blade passages). Day's work is discussed in more detail in section 2.3.2.

2.2.2 Linearized Theories of Stall Inception

The basis for the modal wave explanation of stall development stems from hydrodynamic stability analysis, which deals with small amplitude disturbances and thus linearized flow equations. The stability issue involves examination of the growth or decay of the disturbances. Rotating stall and surge are viewed as limit cycles whose final strength is governed by non-linear effects.

The linearized stability analyses for rotating stall onset share many common features in their treatment of the compressor flow field. Typically, the models are two-dimensional and incompressible, and describe the evolution of a small amplitude perturbation superimposed on a mean compressor operating condition. The wavelength of the perturbations is taken to be much larger than the blade pitch so that the blade rows are represented as actuator or semi-actuator disks¹. Conditions applied across the blade row to link the flow quantities upstream

¹Defined as a model of a blade row as a plane across which mass flow is continuous, but other properties can be discontinuous. The semi-actuator model attempts to represent compressor inertial effects, usually through a first-order lag equation (Greitzer [12]).

and downstream are mass conservation, an inlet/exit flow angle relation, and a momentum relation. Differences between the models are usually manifested in the form of the momentum relation used by each. These forms have included static pressure rise (Stenning [22]), total pressure loss (Fabri [23]), and vorticity conservation with friction losses (Nenni and Ludwig [24]), all described as functions of inlet flow angle. The linearized equations of motion are solved to determine the eigenvalues which define the stability of the flow field, or to examine the growth of the initially prescribed small perturbation (until the disturbance is too large that the linearized treatment is no longer valid).

All of the theories require blade row or stage performance data as input, which typically must be determined by experiment². Additionally, a stability criterion to define the onset of stall development must be specified. This is usually defined to be the neutral stability criterion, taken as the zero slope point on the compressor total-to-static pressure characteristic (Fig. 2.2). As pointed out by Greitzer [12], this zero slope condition provides a rough "rule of thumb," but is not applicable to all machines.

Despite their limitations, the linearized theories have been useful in improving the understanding of the axisymmetric flow breakdown process in axial-flow compressors. Additionally, they

²The prediction of compressor performance characteristics at off-design conditions is difficult, and at present, cannot be done with the required accuracy.

have been used to study the stage (and/or blade row) interaction and overall compressor system effects on stability. These interactions alter the stage stalling behavior from that of the same stage operating in isolation. These areas continue to be of prime interest (Longley and Hynes [25]).

2.3 Recent Works

As noted in the Introduction of this report, two explanations of the compressor stall inception process are currently popular; small amplitude rotating waves (modal waves) and short length scale finite disturbances (finite cells). This section of the literature survey will examine these two flow models in more detail. Additionally, recent experimental applications of both models in the area of active suppression of rotating stall will be briefly discussed.

2.3.1 Modal Waves as a Stall Inception Indication

The wave model of flow field dynamics evolved partly from the early theories described above and more directly from the theory of rotating stall transients proposed by Moore [26] and Moore and Greitzer [27]. In their rotating stall analysis, Moore and Greitzer represent the upstream flow coefficient, ϕ , as consisting of a steady mean flow component, $\bar{\phi}$, and a non-axisymmetric disturbance, $\delta\phi$:

$$\phi = \bar{\phi} + \delta\phi \quad (2.1)$$

Garnier [28] took the equation which models the evolution of the

non-axisymmetric component and linearized it for the case of small amplitude disturbances. The resulting governing equation for the non-axisymmetric disturbance was shown to be of the form:

$$\delta\phi = \sum_{k \neq 0} e^{ik\theta} e^{(i\omega + \sigma)t} \quad (2.2)$$

where:

- k = a Fourier mode ($k=0$ corresponds to surge-like disturbances)
- ω = wave frequency (according to theory, Garnier [28], should correspond to rotating stall frequency)
- σ = growth rate or damping of the wave
- θ = circumferential position
- t = time

In essence, the modal wave view treats the compressor system as a harmonic oscillator with stall onset associated with the growth of long wavelength (long compared to blade pitch) circumferential disturbances. Surge and rotating stall are viewed as eigenmodes of the system (Fig. 2.3), with surge being of zero order and rotating stall-like disturbances being higher order. For example, a velocity perturbation with a wavelength equal to the circumferential length of the compressor annulus would be considered a mode of order one. The growth or decay of the instabilities depend upon the stability criteria related to the operating point of the compressor. If the compressor were throttled towards the stall point, the stall cell would grow smoothly out of the small amplitude modal waves.

Recent experimental investigations by McDougall, et al. [2] and Garnier, et al. [3] have provided support to the wave model of stall inception. McDougall, et al. [2] were the first to demonstrate the rotating disturbances on a single-stage, low-speed axial compressor. Two methods were used for detection: (1) cross-correlation of the unsteady part of signals from two hot wires set 90 degrees apart 0.6 mean radii upstream of the rotor, and (2) spatial and temporal Fourier analysis of signals simultaneously logged from six hot wires equally spaced around the circumference, again 0.6 radii upstream. Resolution of the circumferential harmonics showed the first order Fourier mode to be the dominant one, rotating in sympathy with the variation in endwall blockage at rotor exit. The small amplitude upstream perturbations (about 0.5% of the mean axial velocity near the stall point) were shown to rotate around the annulus at about 49% of rotor speed and transition into fully developed rotating stall with no discontinuity in phase or frequency. The waves could be detected as much as two seconds prior to stall, rising and falling in amplitude, but were of significant amplitude only at conditions very close to stall (one rotational speed was examined and the stall was initiated in a quasi-steady manner). McDougall, et al. [2] concluded that the stalling process was closely related to large length scale disturbances (lower order modes) and not to events occurring in individual blade passages.

Garnier, et al. [3] detected rotating waves in two low-speed compressors (a single-stage and a three-stage) and one high-

speed, three-stage compressor. The compressors were operated in uniform inlet flow, distorted inlet flow, and subject to various throttle rates at a single rotational speed. Discrete Fourier analysis of the signals was used to extract the modal information (hot wires were used for the low-speed rigs, high response static pressure transducers for the high-speed machine). Sets of high-response instrumentation were mounted at several axial stations to examine sensor placement influence. Again, the waves were initially of small amplitude and evolved into rotating stall without sharp changes in phase or frequency. The signals were clearest when measured by the sensors nearest to the stage which initiated the stall. Figure 2.4 presents a sample of Garnier's, et al. low-speed results [3] using the Fourier coefficients. The amplitude of the first Fourier harmonic is shown to be non-zero for about ninety rotor revolutions prior to stall. Additionally, the phase speed of the first harmonic is essentially constant over the same period, and approximately equal to the rotating stall speed (35% rotor speed before stall, 38% speed in fully developed stall). Note as with McDougall's, et al. work [2], the first order mode was dominant in the low-speed results. Results from Garnier's, et al. high-speed investigations [3] were qualitatively similar to the low-speed results, but also revealed significant influence by the second harmonic. No explanations have been offered for the dominance of one mode over another.

Garnier, et al. [3] concluded that the modal waves and fully developed rotating stall are two stages of the same phenomenon.

He also noted that simple Fourier techniques were inadequate for determination of the waves in distorted flow fields, and suggested a signal processing method based on the true system eigenmodes.

2.3.2 Finite Cells as a Stall Inception Indication

Day's recent experimental work with two low-speed compressors [7, 11] has resulted in an alternative view of the stall development process; namely, the importance of small length scale disturbances (finite cells). Using similar instrumentation and data processing as McDougall, et al. [2] and Garnier, et al. [3], Day [7] showed that modal waves did not always precede stall, and when present did not necessarily show a strong coupling to the stall development process. Day's work showed the stall inception process to be governed by the formation and subsequent growth of finite cells of length scales he classified as small and large with respect to blade pitch. Increased coupling of the modal waves and finite cells was more likely when the length scales of the waves and stall cell were comparable (i.e., when the stall cell covered a large region of the annulus). Tip clearance appeared to be important in determining which stall inception model applied, with increased clearance more likely to reveal modal waves prior to the development of a longer length scale finite cell (Fig. 2.5). Tighter tip clearance favored the formation of a smaller length scale cell with no evidence of modal waves beforehand (Fig. 2.6). Day

concluded that modal perturbations and the formation of finite stall cells were not necessarily related; either disturbance might be the first to appear.

2.3.3 Active Control Experiments

Although not directly related to the scope of the present work, recent experiments by Paduano, et al. [6] and Day [11] using active controls to suppress rotating stall and delay its onset demonstrate the potential benefits of identifying a reliable stall precursor signal. Paduano, et al. [6] applied the modal wave flow model by "wiggling" inlet guide vanes to damp the perturbations in the same single-stage compressor used by Garnier, et al. [3]. This resulted in a 20% gain in compressor mass flow range when the first two Fourier modes were controlled.

Day [11] used fast-acting air injection valves both globally (the entire annulus) to damp out modal waves (when present) and locally (a portion of the annulus) to remove emerging finite stall cells. Results indicated a 4% increase in flow range when the waves were damped and a 6% increase in range when the finite cells were removed (the valves could not be operated in both global and local modes simultaneously). Both Paduano's, et al. [6] and Day's [11] active control schemes required minimal power to implement compared to the power of the compressor (a major difference from previous stall control schemes), and demonstrated the feasibility of actively suppressing compressor instabilities.

2.4 Potential Factors Affecting Stall Precursor

It is appropriate to provide some discussion regarding the influence (or potential influence) of a variety of factors on stall precursor signals (or the ability to detect such signals). These factors include compressor environment (inlet distortion), operating conditions (rotational speed, mass flow transients), sensor location, speedline shape and factors which influence that shape (i.e., tip clearance), and compressibility effects (shock waves, stage mismatching, etc.). Investigating the influence of these factors is important for developing a sound physical understanding of the stall inception process so that the factors (or their effects) can be included in advanced modelling of compressor stability.

Several of these factors have been documented in previous investigations. Garnier [28] showed that inlet distortion (spatially non-uniform inlet total pressure) hindered detection of the pre-stall waves (using Fourier techniques). He further suggested an analysis technique based on the true system eigenmodes (independent of wave shape). The effect of sensor location was also studied by Garnier [28] in his single-stage, low-speed and three-stage, high-speed compressor investigations. The low-speed results indicated no major differences in terms of when wave propagation could be detected versus axial position of sensors. The high-speed results showed much stronger dependence on axial sensor location, with maximum stall warning time obtained from the measurements (leading edge of the first stator)

closest to the stage which initiated the stall. Additionally, Garnier [28] examined the effect of different throttle closure rates (mass flow transients), and found the stall warning time to be roughly inversely proportional to the time rate of change of mass flow at stall. It is important to note that the throttle closure rates used by Garnier [28] (maximum $d\phi/dt = -0.00073$ 1/s) all resulted in quasi-steady compressor stalling (i.e., the compressor steady stall line was valid). Rapid closure rates would likely result in transient compressor stalling (steady stall line no longer valid), discussed further in section 4.1.

The importance of speedline shape on compressor stalling behavior has been well documented in several experimental and analytical investigations (i.e., Greitzer [31], Bonnaure [20]). In fact, all of the compressor post-stall and/or stability models rely on accurate compressor characteristics (speedlines) to represent the physical behavior. As discussed in section 2.2.2, the zero slope condition is typically taken as the onset of compressor unstable performance. For advanced stall warning time, a characteristic with a local positive slope at stall might be desirable. A speedline that is bent over (positively sloped) is identified with thickening boundary layers, larger wakes, and in the extreme, endwall or tip stalling. These are all features of impending flow breakdown - stall. Note that tighter tip clearances would tend to reduce the positively sloped region of the characteristic (less losses) and result in potentially less stall warning. Indeed, Day's results [7] showed that increased

tip clearance appeared to favor formation of modal waves which evolved smoothly into rotating stall (see Fig. 2.5).

The influence of compressibility effects on compressor pre-stall behavior has not received as much attention as the before-mentioned factors (largely due to the lack of high-speed experimental results). In his recent analytical investigation, Bonnaure [20] found the influence of compressible unsteady perturbations (local mass flow perturbations which vary along the compressor length; in low-speed case, these are the same everywhere) to be key in determining compressor stability. Indeed, Bonnaure's work [20] appeared to confirm the high-speed results of Garnier [28] which showed strong dependence on axial sensor location (preceding paragraph).

The effect of shock waves on the stalling process of transonic designs (as are those in the current investigation) is not, in general, well understood. For example, much work is currently ongoing in the facility where the current tests were conducted (see section 3.1) to characterize the rotor tip shock structure of several designs at near-stall operating conditions. Although the current set of experiments did not quantify the rotor shock strength, the one significant design difference (backwards sweep versus straight leading edge) allowed some inferences to be made regarding the potential influence of shock waves on stall precursor signals. A discussion of this influence is provided in section 5.6.

3.0 TEST APPARATUS

3.1 Facility Description

The facility used for all the testing was the Aero Propulsion and Power Directorate's 2000 horsepower (hp) Compressor Aerodynamic Research Laboratory (CARL) located at Wright-Patterson AFB, Ohio. An artist's rendition of the facility is illustrated in Fig. 3.1. Table 3.1 summarizes the test cell operating parameters. The CARL is a closed loop facility shown schematically in Fig. 3.2.

Air passes through the 30-inch diameter inlet duct to a Universal venturi tube located six pipe diameters downstream of the return tube elbow. The air is turned 90-deg with the aid of turning vanes and passes through a tube bundle into a 48-inch diameter settling chamber. The screens installed both upstream and downstream of the turning vanes are used to prevent feedback related to flow separation on the vanes from reaching the venturi. From the settling chamber, air enters the compressor through a direct-coupled bellmouth. The flow leaving the compressor is deflected radially outward to a peripheral throttle. The throttle consists of one stationary and one rotating cylindrical ring, each with 16 circumferentially distributed holes. The throttle is designed to vary continuously from fully open to fully closed, and throttling takes place at a diameter of about 47 inches. A surge valve is opened to bypass the throttle when recovering from compressor stall. Downstream

of the throttle, the air enters a collector and then passes through a 24-inch diameter duct to a heat exchanger and filter. The air is filtered to remove 5-micron particles and then returned to the facility through the 30-inch diameter inlet duct.

3.2 Test Vehicle and Designs Tested

One of the primary missions of the CARL is to conduct Parametric Blade Studies (PBS) to investigate the effects of specific rotor blade design parameters (maximum thickness location, surface angles, leading edge sweep, etc.) on the performance of one compressor configuration. To date, ten rotor designs and one baseline have been tested under the PBS series. For the current research, two of these rotors were used. This section provides brief descriptions of the rig configuration and rotors tested specifically for the present work. More general information regarding the PBS tests can be found in a report by Law and Puterbaugh [29].

3.2.1 Fan Rig Description

A cross-section of the rig is shown in Fig. 3.3. The rotor tip diameter is constant at 17 inches. The configuration used no inlet guide vanes. The rotor shaft is mounted on an oil-damped roller bearing at the forward location and a ball bearing at the aft location. The rotors were machined from single forgings³ of

³These single castings are commonly referred to as blisks for bladed disks, or IBRs for integrally bladed rotors.

6Al-4V titanium. The stator was also fabricated as an integral ring machined from AMS 5616. The backward swept stator design used a controlled diffusion airfoil (CDA) approach for controlling suction surface diffusion to prevent boundary layer separation. Stator design parameters are summarized in Table 3.2.

3.2.2 Rotor Designs Tested

Rotors 4 and 6 of the PBS series were investigated for the current stall precursor research. Table 3.2 provides some of the design features of the rotors. Both are considered low-aspect ratio, high-throughflow, transonic designs. At design conditions, rotor tip speed is 1500 ft/s, and approximately 60% of the blade span sees supersonic relative flow velocities. The leading edge of Rotor 6 is swept backwards to reduce shock losses. Rotor 4 has a more conventional straight leading edge. Photographs of the rotors installed in the rig are shown in Figs. 3.4 and 3.5. The location of the high-response pressure transducers (Kulites) relative to the leading edge tip of each rotor is also indicated. Close-ups of this area (Figs. 3.6 and 3.7) reveal that the distance from the blade tips to the Kulites was the same for both rotors, 2.5 inches.

Tip clearance as a function of rotor speed for Rotors 4 and 6 is shown in Fig. 3.8. Note that the clearances are nearly identical for both designs. Hot (rotating) clearance was measured with an active, non-touching, spark-gap type clearance

system at the rotor leading edge and mid-chord regions (encircled areas 1 and 2, respectively, in Fig. 3.3) at two circumferential locations. The average clearance at design speed was about 0.020 to 0.025 inches, approximately 0.6% of the rotor tip chord. Since both sensor location and tip clearances were virtually identical for both designs, these were not considered as possible explanations for any measured differences in stalling behavior between the two rotors.

3.3 Instrumentation

Certain steady-state compressor and facility instrumentation is considered standard for all tests conducted in the CARL. These were used for the current tests and will be described briefly in this section. More detail is provided by Law and Puterbaugh [29]. The main focus of this section is on the high-response static pressure transducers used for stall precursor detection.

3.3.1 Test Facility Instrumentation

Rotor speed was measured by a Bentley Model 306 proximity transducer which senses six grooves machined into the gearbox/rotor driveshaft coupling. The output was conditioned and directly recorded by the data acquisition system (DAS). A tachometer provided visual indication of rotor speed accurate to about 10 rpm.

Inlet mass flow was metered through a 30-inch venturi (see

Fig. 3.2) with a 17.4-inch throat. Meter accuracy has been calibrated to $\pm 0.5\%$ by the manufacturer (B.I.F. Industries).

Inlet total pressure and temperature were measured just downstream of the last screen in the plenum (see Fig. 3.2). Because of the low plenum velocities, compressor inlet total pressure was assumed equal to plenum static pressure measured by four static pressure taps manifolded into two pressure sources. At maximum flow rate, the error is no worse than 0.003 psi, verified by calibration. Total temperature was averaged from nine bare junction thermocouples located in the same axial plane as the pressure taps at three different radii. Additionally, relative humidity was measured in the inlet for every steady-state test point and subsequently treated in the data processing software for the calculation of mass flow rate.

3.3.2 Compressor Instrumentation

Compressor steady-state instrumentation is shown schematically in Fig. 3.9. A total of 276 sensors were used to measure aerodynamic parameters at various locations throughout the stage. Nine thermocouples were mounted in the stator vane leading edges and eighty were located in ten discharge plane rakes. The thermocouples are of the slot vented type shown in Fig. 3.10.

A total of 125 pressures were measured in the flowpath; 36 static pressures and 89 total pressures. Casing static pressures were made at fifteen axial locations, twelve of these

over the rotor tip (see Fig. 3.9). The total pressure probes were all Kiel stagnation tube design (Fig. 3.10) and were divided in a manner identical to the thermocouples. Both discharge plane total pressure and temperature rakes were uniformly distributed around the circumference and spaced to divide a single exit vane passage into ten equal parts.

The only compressor measurements used for the current analysis were the total pressures and temperatures measured by the discharge rakes (Fig. 3.9). These were averaged and used with the inlet measurements in the computation of stage pressure ratio and adiabatic efficiency for each steady-state data point acquired during the test program (i.e., Figs. 4.1 and 4.2).

3.3.3 Calibration and Measurement Uncertainty

Since the main concern of the present work is the analysis of unsteady pressure signals, the steady-state pressure and temperature calibrations will not be discussed here. Details of the calibrations are provided by Law and Puterbaugh [29]. The steady-state measurements were used in the current research to define where precisely on the fan performance map the first signs of pre-stall behavior occur. Table 3.3 indicates the accuracy to which this could be done. The uncertainties reported in Table 3.3 were determined through a combination of measurement device performance specifications (for bias error) and facility historical performance (for precision error). Each measured value (pressure, temperature, etc.) was perturbed slightly to

obtain the performance sensitivities to changes in various parameters.

3.3.4 Data Acquisition System (DAS)

Fan rig performance and calibration data were collected by the DAS. The DAS consists of a MODCOMP MODACS digital and analog I/O subsystem, a MODCOMP ATC communications I/O subsystem, and a high frequency analog data recording subsystem, all controlled by a host computer. The host computer is a MODCOMP Classic II/15 16-bit microprocessor with 512 kilobytes of memory and additional peripherals. Additional information can be found in the report by Law and Puterbaugh [29].

Facility and rig controls and compressor operating parameters are all patched to a control room for monitoring during testing. A photograph of the CARL control room is provided in Fig. 3.11. The DAS software capabilities include real-time update of compressor performance parameters, automated data recording, and DAS health monitoring.

3.3.5 Unsteady Pressure Measurement

Eight high-response static pressure transducers (Kulite model XCEW-1-187-100 G) were located in the compressor inlet for detection of unsteady pressure perturbations. Table 3.4 summarizes the performance characteristics of the transducers. The transducers were equally spaced around the circumference casing approximately 0.3 rotor radii (2.5 inches) upstream of the

rotor tips (exact locations for each rotor shown in Figs. 3.6 and 3.7). Actual circumferential location of each transducer is indicated in Fig. 3.12. As noted in the Appendix, the equal spacing around the annulus simplifies the Fourier analysis that is useful in determining the presence of modal waves.

Since the present work was concerned with unsteady pressure signals, the Kulites were operated in a differential mode. The reference side of each transducer was manifolded to a static pressure tap located at approximately the same measurement plane as the Kulites. A long tube length was used to effectively filter any unsteadiness from the reference side. Thus, measured signals were true unsteady pressure perturbations.

The path of each of the Kulite signals is shown in Fig. 3.12. A B&F model input conditioner provided 15-volt excitation and completed the electronic bridge. Variable gain amplifiers (Bell and Howell, and Neff) were adjusted to allow for maximum sensitivity without driving the background noise levels too high. The signals of interest were expected to be on the order of one-tenth of a psi, thus it was desirable to keep the background noise below this level. After amplification, the signals were analog recorded (FM on 100 khz carrier) on a 14-channel Bell and Howell model VR-3700B recorder and patched to oscilloscopes for on-line monitoring. A spectrum analyzer was also available for on-line use. All data processing was performed post-test, and is described in the next chapter.

In-place calibration of the Kulites was accomplished using a

Druck DPI 510 pressure controller/calibrator, sequentially applying the calibration pressure to each transducer. Amplifier gains were adjusted (resulting gains were about 200) so that 5.0 psig provided a 2.0-volt DC transducer output. Static (non-rotating) noise levels with these amplification settings were no greater than 10 mV peak-to-peak for each of the eight channels.

Each transducer was calibrated with 5.0, 2.0, 1.0, 0.5, 0.2, and 0.1 psig control pressures. The calibration data is summarized in Table 3.5. An important consideration from the calibration process was that any signal less than approximately 0.1 psi would be lost in the noise. All the calibration curves were linear down to about 0.5 psig. In fact, only Kulites 2, 3, and 5 displayed significant non-linearities (see Table 3.5) at the very low pressures (<0.5 psig). Despite the non-linearities of the three transducers, linear calibration curves (all with a slope of 2.5) were applied to each Kulite signal for the following reasons:

(1) The unfiltered measured pressures all contained high amplitude, high frequency components (i.e., blade passing frequency) that placed the Kulites in their linear operating range over most of the low-frequency period of interest (the fundamental frequency of interest is approximately 50% of the rotor frequency).

(2) The prime concern is frequency content rather than exact amplitude definition.

4.0 TEST PROCEDURE AND DATA PROCESSING OF UNSTEADY PRESSURES

4.1 Test Procedure

All of the Kulite data were obtained at both steady-state and transient operating conditions at five different speeds (60, 70, 80, 90, and 100% design speed) for each rotor. For both rotors, a detailed steady-state performance map was generated prior to the acquisition of any unsteady pressures. The maps, shown in Figs. 4.1 (unswept, Rotor 4) and 4.2 (backward swept, Rotor 6), were used for determining throttle settings for starting the transients to stall and for the near-stall steady operating conditions.

The steady-state data were obtained very systematically. Upon reaching a desired speed, a three-minute settling time was used to allow system transients and thermals to steady out. After this, a throttle position was set and another two minutes of settling time was used before acquiring thirty seconds of Kulite data. The procedure was repeated for each change in throttle position and compressor speed.

Only one throttle closure rate was available for obtaining the compressor transient data to stall. At each speed, the throttle was initially set so that the compressor was at some nominal unchoked operating condition (about 7.0% greater flow than that at the near-stall steady-state condition). The FM recording tape was then turned on and Kulite data recorded while the throttle was continuously closed. Once stall was detected

(both audibly and by monitoring the Kulites), the surge valve was immediately opened and the stall was cleared. A typical throttle closure to stall (transient) took between thirteen and fifteen seconds. The throttle closure rate was approximately -0.3 lbm/s/s, calculated as defined below:

$$\frac{dW}{dt} = \frac{W_{stall} - W_{initial}}{\Delta t} \approx -0.3 \frac{\text{lbm/s}}{s} \quad (4.1)$$

During the transients, it was observed that the compressor stalled at a lower mass flow than the steady-state stall point (the indicated throttle position was about 5% more closed during transient stall). This was not unexpected given the rather fast closure rate (compare eqn. 4.1 with the rates used by Garnier [28] discussed in section 2.4) and the well-known fact that most separation phenomena seem to have a time constant associated with them. Figure 4.3 schematically demonstrates the transient behavior of both an isolated airfoil and compressor. This unsteady flow behavior helps explain why rotating disturbances could be detected prior to stall during the transients, but were not discernible in the majority of steady-state points (discussed in Chapter 5.0). Unfortunately, other than the inlet Kulites, no transient measurements were available for the test programs. Consequently, accurate location of the transient stall line could not be determined.

4.2 Data Sampling

As noted previously, all unsteady pressure signals were

recorded on analog tape and post-processed after the testing was complete. The tapes were played back on a Honeywell model Ninety-six Magnetic Tape System and all signals were low-pass filtered using a Rockland Multi-channel Filter System 816. The filtering was used to prevent massive file storage problems, and because the maximum frequencies of interest were expected to be approximately 600-700 Hz (the third harmonic of 50% of the rotor frequency, the fundamental frequency of interest). Consequently, an 8-pole Butterworth low-pass filter with a cutoff frequency, f_c , of 1 kHz was configured. Filter characteristics are shown in Fig. 4.4. Also, since the concern was on the pressure perturbations, any DC-bias was removed from the signals.

Taking the sampling theorem (accurate reproduction of an analog signal requires sampling greater than twice the highest frequency of interest, Stearns and Hush [33]) and filter characteristics (Fig. 4.4) into account, the signals were sampled at a rate of 4 kHz. Note that a 4 kHz sample rate places the Nyquist frequency (one-half the sample rate) of 2 kHz at twice the filter cutoff frequency, $2f_c$. Any signal greater than 2 kHz and sampled at 4 kHz has the potential to be artificially introduced as a lower frequency (aliasing); however, according to Fig. 4.4, a frequency at $2f_c$ is down in amplitude by 48 db. Thus, the 4 kHz sample rate was chosen as a good tradeoff between controlling file size and minimizing any aliasing. Examination of the spectrums of the unfiltered and filtered signals revealed that no aliasing occurred. Thus, with 8 channels digitized at 4

kHz, sampling a 10-second record resulted in a 2.56-Mbyte data file (8 bytes per sample per channel). All data were stored in standard ASCII format with each column containing the sampled filtered signal from one of the eight Kulites.

4.3 Additional Digital Filtering

In addition to the analog filtering, unwanted frequencies were removed by using digital finite impulse response (FIR) filters. These were chosen for their desirable characteristic of linear phase shift (constant time delay).

Upon examination of the raw analog filtered traces and spectrums of those traces, it was found that several unwanted frequencies were present from many different sources. All traces showed a 1/rev rotating wave (i.e., at the rotor frequency) and a very strong low frequency planar wave (and several harmonics). Further, several channels had strong 60 Hz (and harmonics) electrical noise components. Figure 4.5 shows an example of a frequency spectrum that was obtained from Kulite #2 at 90% speed (310 Hz). All of the just-mentioned frequencies are evident in the spectrum. The planar wave with fundamental frequency at approximately 13.5 Hz is believed to be a system resonance. It had a significant effect on the results and is discussed further in the next chapter.

Among the many alternatives for handling the unwanted frequencies, it was decided to digitally band-pass filter the data around the rotating stall frequency. This limited the

examination of the modal waves to the first harmonic (SFC #1), but was done for the following reasons:

(1) It was the simplest means for removing the majority of the unwanted frequencies.

(2) Examination of the first three rotating modes (via Fourier techniques discussed in section 4.4.2) revealed that most of the modal wave energy appeared to be contained in the first harmonic and the additional filtering enhanced its features.

(3) The frequency of the first harmonic for all speeds was approximately 50% of rotor frequency (the rotating stall frequency). Consequently, the second modal wave harmonic showed up right around the 1/rev frequency making it difficult to resolve.

Shown in Fig. 4.6 is the same trace as in Fig. 4.5, but band-pass filtered between 130 Hz and 230 Hz. Comparison of the two figures reveals no attenuation of the frequencies in the range of interest. Additionally, no new information has been introduced as a result of the filtering. The before and after spectra of each filter application were checked in this manner to ensure no erroneous results were introduced. Table 4.1 contains a summary of the frequency band-pass applied to the data at each compressor speed. In each case, a 248-order, Hamming-windowed, FIR filter was applied using MATLAB [30] tools. Unless otherwise indicated, all plots presented in the next chapter were generated from the band-pass filtered data with frequency range given in Table 4.1.

4.4 Forms of Data Presentation

Three basic forms of data presentation were used to aid in the analysis of the measured unsteady pressures. These included plots of the filtered raw traces, magnitude and phase of spatial Fourier coefficients (SFCs), and power spectral densities (PSDs) of the SFCs. Figure 4.7 summarizes the signal processing techniques used for characterizing the stalling process. MATLAB [30] was the software package used for the signal processing and plot generation. Each form provided valuable information as is seen in the next chapter. The details of each are provided below.

4.4.1 Filtered Raw Pressure Signals

Prior to any Fourier analysis, the filtered raw pressure signals were examined extensively. In particular, the last 20-100 rotor revolutions (rotor revs) prior to stall were carefully studied for any evidence of a stall precursor. Calibration curves were applied to all pressure signals so that plots of the filtered data traces reveal actual pressure perturbations in psi (rather than volts). Figure 4.8 is an example of a raw signal plot which clearly indicates the presence of a rotating disturbance. The traces were artificially separated to help view the individual signals (otherwise they would lay on top of each other) and track the rotating phenomena. In all the plots which display the eight individual signals, Kulite #1 (see Fig. 3.12) provides the bottom trace and Kulite #8

the top trace.

4.4.2 Spatial Fourier Coefficients

The pressure signals were spatially resolved through the use of the discrete Fourier transform (DFT). A review of Fourier techniques with application to the current work is provided in the Appendix. By taking the period to be eight, the SFCs can be computed at each discrete time from:

$$c_k = \frac{1}{8} \sum_{n=0}^7 p(\theta_n, t) e^{\frac{-j2\pi nk}{8}} \quad (4.2)$$

where k is the mode number, or wave harmonic. As discussed in the Appendix, the c_k 's are complex conjugates, but for the case of eight equally spaced measurements, only the c_k of the first 3 modes (c_{-1} , c_{-2} , c_{-3}) need be computed. Thus, it is seen from Eqn. (4.2) that eight pressure traces are reduced to a single complex number at each instant in time. The complex number (SFC) contains the desired phase and amplitude information for each spatial wave number, k , which can then be tracked in time. If:

$$c_k = x + jy \quad (4.3)$$

Then:

$$|c_k| = c_k c_k^* = \sqrt{x^2 + y^2} \quad (4.4a)$$

$$\angle c_k = \tan^{-1} \left(\frac{y}{x} \right) \quad (4.4b)$$

If a sinusoid is present, the phase, $\angle c_k$, represents the angular position of its peak.

Plotting the amplitude and phase of each SFC as functions of time helps reveal any rotating perturbations that might be present in the system. Of these, the unwrapped phase plots⁴ can be the most revealing as a rotating disturbance propagating at a constant speed will show up as a constant slope. However, care must be taken in interpreting these plots as the $\angle c_k$ will "lock on" to the most dominant rotating disturbance.

Figure 4.9 illustrates the usefulness and potential pitfalls of applying the spatial DFT. The plots show 70 rotor revs up to and including the start of a rotating stall at 90% speed (stall @ $t=464$). Both phase plots indicate the presence of a rotating disturbance. However, calculations of the slopes reveal that in Fig. 4.9a, the disturbance is propagating at the rotor frequency ($1/\text{rev}=310$ Hz). This is further evidenced by the change in slope at approximately $t=461$ when the rotating stall frequency dominates. In Fig 4.9b, the undesired rotor frequency has been removed prior to performing the DFT, and the phase plot now reveals the desired rotating stall frequency prior to stall (no change in slope at $t=461$). It is also of interest to compare the amplitude plots of both cases. Note that the $1/\text{rev}$ disturbance is the major contributor to the amplitude prior to the actual stall as evidenced by the reduced magnitude plot (Fig. 4.9b)

⁴Phase plots are typically confined between π and $-\pi$. For the case of a rotating disturbance, it is convenient to unwrap the phase and allow it to grow with time.

after the 1/rev component is removed.

4.4.3 Power Spectral Densities

By performing a temporal Fourier transform or standard fast Fourier transform (FFT) on each SFC, the power spectral density (PSD) of an SFC can be computed. Examination of the PSDs can reveal pre-stall waves that otherwise would be masked by other rotating phenomena, for example, a strong 1/rev signal. Figure 4.10 is an example of a PSD taken on the same data used to generate Fig. 4.9a (but not including the stall itself). Note that in addition to the expected strong peak at 1/rev, a peak is revealed at approximately 50% rotor frequency. No evidence of this frequency was apparent in the phase plot of Fig. 4.9a.

When computing the spectrum, only data up to the stall event must be used. If any of the in-stall data is included, the stall will dominate the spectrum and no conclusions will be able to be made regarding the small amplitude pre-stall behavior. To alleviate this problem, PSDs were performed on the near-stall steady-state data (as close to stall as possible without inadvertently dropping into stall) and the portion of the transient data up to (but not including) stall. Also, as described in the Appendix, because the SFCs are complex numbers, the PSDs are not necessarily symmetric about zero frequency. Only those PSD peaks which do not exist at identical positive and negative frequencies indicate rotating disturbances. Thus, both the positive and negative frequencies were overplotted.

5.0 RESULTS AND DISCUSSION

5.1 Introductory Remarks

Presentation of results is provided primarily in sections 5.3 and 5.4 along with some discussion. Because of their effect on the results, the low frequency planar oscillations mentioned in section 4.3 are discussed first in the next section. Additional discussions regarding the effects of compressor speedline characteristic and shock waves are presented in sections 5.5 and 5.6. In the last section, results are compared with those from previous investigations.

5.2 Low Frequency Planar Oscillations

As noted in section 4.3, planar waves with fundamental frequency of about 13.5 Hz were evident in all transient and near-stall steady data obtained on both rotors. As exemplified in Fig. 4.5, the second harmonic of this wave (27 Hz) was dominant at all rotor speeds except 100% speed for both designs. At 100% speed, the fundamental frequency dominated. Although the precise nature of the planar oscillations could not be determined (these type oscillations have been observed in previous investigations; see Greitzer [31]), they are believed to be the result of some overall system resonance (rig and facility) for the following reasons:

- (1) the frequency did not change with compressor speed.
- (2) the waves were seen in the near-stall steady-state

data, thus eliminating the notion that they might be induced by the throttle ramp rate.

(3) the facility is closed-loop and believed to be more susceptible to resonances than an open-loop facility.

In order to verify the system resonance theory, the compressor and inlet and exit ducting were modeled as a Helmholtz resonator in a manner similar to Emmons, et al. [21] and Greitzer [31]. The Helmholtz frequency, ω , is defined as:

$$\omega = a \sqrt{\frac{A_c}{V_p L_c}} \quad (5.1)$$

where A_c and L_c are the area and length of the equivalent compressor with constant area inlet duct, V_p is the discharge plenum volume, and a is the speed of sound. For the current set of tests, the discharge volume was fixed and the throttle choked; thus, V_p was calculated with a high degree of confidence. However, choosing A_c and L_c were somewhat arbitrary, especially with a closed loop facility. Two attempts were made, first including inlet volume only up to the screens in the inlet plenum (see Fig. 3.2), then adding the remaining inlet plenum volume up to the perforated cone (Fig. 3.2). The first attempt produced an $\omega = 149$ Hz, the second, $\omega = 80$ Hz. The question as to which inlet volume should or should not be included is undecided, and certainly by including enough, a 13.5 Hz (or 27 Hz) resonator could be established.

The presence of the planar oscillations complicated the signal processing procedures used for detection of the rotating

phenomena of interest here. This complication arises because the oscillations were observed close to the onset of stall and were consistently detected before any rotating perturbations were observed (i.e., planar waves could be seen in the near-stall steady data, rotating waves were not).

As seen in Fig. 5.1a, the planar waves were initially of small amplitude and grew as the machine was continually throttled to stall. Even when the data were high-pass filtered above 60 Hz, the effect of the waves was clear (Fig. 5.1b); the oscillations effectively throttled the stage into and out of stall. A clearer picture of this is provided by Fig. 5.2, which shows the in-stall behavior at 80% speed. The behavior shown is quite consistent with surge-like oscillations (see, for example, Greitzer [31]). Of particular interest to the current work is the small-amplitude "surging" that occurred prior to stall and its influence on the rotating disturbances. This influence is shown schematically in Fig. 5.3 and is evidenced in the majority of the results presented in the next section.

5.3 Analysis of Results

Because the rotors studied are so close in design, it is appropriate to present results via speedline (for both rotors) rather than by rotor. This allows for direct comparison between designs and facilitates a discussion regarding any significant differences in stalling behavior. Signal processing of the data was performed as described in Chapter 4.0. Some examples of

signal traces without the additional filtering (Table 4.1) are also provided. Plots presented as functions of time use rotor revolutions (rotor revs) as the time scale since this is the scale of the phenomena of interest. In most time plots, only the last 1-2 seconds prior to the stall event are shown since the current investigation is concerned with stall inception.

Rotating stall frequencies for all cases were between 50-56% of rotor frequency. A single stall cell was identified in all the cases examined. As noted in section 1.2, both progressive and abrupt rotating stall were observed. Progressive stall was seen at low-speed operation (60% speed for the unswept rotor, #4, and 60 and 70% speed for the swept rotor, #6), as would be expected (Greitzer [12]).

At all speeds for both rotors, stall was preceded by small amplitude rotating waves which grew rapidly once the onset of the instability was reached. Thus, the plots presented for either rotor are meant to be representative of the stall inception behavior of both designs. The only significant difference was in the amount of time the modal waves could be detected prior to stall. The differences in stall warning time will be discussed qualitatively in this section, and more quantitatively in the following section (section 5.4).

The data digitizing system described in section 4.2 became inoperative before any steady-state data for Rotor 6 could be sampled. In this sense, the data analysis was not as complete as it could have been. However, given the data that were examined

(Rotor 4 steady-state and transient and Rotor 6 transient), a high level of confidence is placed in the results and conclusions that follow.

5.3.1 60% Design Speed

This was the only speed where the relative rotor flow velocities were subsonic across the entire span. As noted above, a progressive rotating stall was observed for both designs at this speed. The data traces for Rotor 4 (unswept) were previously presented in Fig. 5.1; the traces for Rotor 6 were quite similar and are not shown. The progressive nature of the stall can be seen in Fig. 5.1b as the pressure perturbations experience a relatively slow growth (compare the traces in Fig. 5.1b to those of Fig. 5.7b). As indicated in Fig. 5.4, initial signs of the stall became evident at around $t=196$. Note the small amplitude rotating wave (≈ 0.2 psi peak-to-peak) at approximately 50% rotor frequency ($0.5/\text{rev}$) emerging at $t=196$ and being attenuated by $t=201$.

From a stall warning viewpoint, this case of a progressive stall is relatively uninteresting as one can throttle in and out of stall without sudden changes in compressor performance. However, for completeness, the amplitude and phase plots for SFC #1 are provided in Fig. 5.5 and do indicate the presence of the rotating disturbance from about $t=190$ on. Note that traces of the disturbance can be seen prior to $t=190$.

Figure 5.6 shows the PSD of SFC #1 at the near-stall steady

condition (DV053) and next higher flow condition (DV050) for which data were obtained. The insert identifies the compressor operating conditions (% design pressure ratio versus % design flow) corresponding to these two throttle settings. The peak at 110 Hz (about 51% of rotor frequency; see Fig. 5.5 phase plot) at the near-stall condition provides further evidence of the pre-stall rotating waves. No discernible peak at 110 Hz is evident at throttle setting DV050; hence, no rotating wave behavior is apparent. This was the only speed in which a pre-stall indication was evident in the near-stall steady-state data.

5.3.2 70% Design Speed

As evidenced in Fig. 5.7, the stall at 70% speed for Rotor 4 was abrupt and relatively clean (the effects of the low frequency oscillations were minimal). The planar oscillations described in section 5.2 were still present (their effect can be seen best in Fig. 5.7b through low frequency modulation of the rotating stall frequency), but were not as strong. Examination of the last twenty rotor revs prior to stall (Fig. 5.8) reveals the stall cell emerging smoothly from small amplitude rotating waves (at about $t=483$). Prior to $t=483$, it is difficult to detect any coherent rotating disturbance in the raw traces.

Because the Kulite traces were relatively clean of unwanted frequencies, higher order Fourier modes were also examined at this speed. Shown in Fig. 5.9 are the amplitude and phase plots of the first two spatial modes (SFC #3 contained virtually no

energy). As indicated in the magnitude plot prior to stall (stall at $t=485^5$), the energy content of the first two modes is quite similar, with SFC #1 displaying slightly more activity. Both phase plots appear to show a reduced slope change at about $t=470$ (from 1/rev to ≈ 0.52 /rev). The slope from $t=470$ on corresponds to a rotating disturbance traveling around the annulus at about 52% of the rotor frequency (note the slope remains the same subsequent to stall onset at $t=485$), indicative of the impending stall. Using the phase plot data of Fig. 5.9, it appears that minimal stall warning time (15 rotor revs) is provided at this speed for Rotor 4.

Plotting the PSD of the spatial Fourier coefficients provides another tool for examining the stall inception behavior of the compressor. The data obtained during the transient to stall can be used provided the stall event itself is not included. The power spectra will then reveal any small amplitude resonances in the system even if they are present only for a short duration. This was the procedure followed since the steady-state data provided no insights into the stalling mechanism.

Shown in Fig. 5.10 are PSDs of SFC #1 at 70% speed obtained using the transient data including stall (5.10a) and up to stall (5.10b). The same plots are shown for the second mode in Fig. 5.11. Because the SFCs are complex, their spectra are not

⁵For consistency at all speeds, the onset of stall was taken to be when the amplitude of SFC #1 reached 50% of its final value.

necessarily symmetric (explained in the Appendix and Chapter 4.0); consequently, positive and negative frequencies are overplotted. Peaks that exist at identical positive and negative frequencies indicate a standing wave (note the twin peaks at 120 Hz in Figs. 5.10b and 5.11 which imply an amplitude oscillation of a standing wave; due, in this case, to electrical noise which was strongly present on some channels and not evident at all on others). Thus, only those signals which do not occur at identical peaks indicate rotating disturbances. A further complication for this particular speed is that the rotating stall frequency is quite close to the 120 Hz noise frequency. Nevertheless, the stall frequency did show up to be slightly higher (123 Hz) in the data which included the stall (Fig. 5.10a). The same is true in Fig. 5.11a for the second harmonic (246 Hz). Examination of Figs. 5.10b and 5.11b reveals no peaks at the stall frequency. Given the 120 Hz complication and the complexity added by the low frequency planar waves, the spectra offered no additional information regarding the stalling process.

The stall of Rotor 6 (swept) at 70% speed was quite different from that of Rotor 4. The behavior of Rotor 6 was characterized by a progressive stall very similar to that described in section 5.3.1 for both rotors at 60% speed. The progressive nature of the stall is represented in the SFC #1 amplitude plot of Fig. 5.12, where one can see a relatively gradual increase in the energy content. Also, the effects of the low frequency planar oscillations are apparent in the amplitude

plot of Fig. 5.12, as can be seen clearly from about $t=570$ on (note the modulations at approximately 27 Hz). Comparison with the SFC #1 amplitude plot in Fig. 5.9 shows that Rotor 4 stalls quite abruptly relative to the Rotor 6 stall at this speed, and the effect of the planar oscillations is minimal. Further evidence of a slowly developing (progressive) stall is provided in the phase plot of Fig. 5.12, which shows a relatively constant slope (for the entire 200 rotor revs plotted) corresponding to a rotating disturbance at about 0.5/rev. Despite the differences in the type of rotating stall encountered (abrupt, Rotor 4; progressive, Rotor 6) by the two designs at 70% speed, the basic mechanism of the stall development process of the two rotors was identical - growth of small amplitude rotating waves (Figs. 5.9 and 5.12).

5.3.3 80, 90, and 100% Design Speed

At the higher compressor speeds, abrupt stall (sudden, discontinuous decrease in performance at stall onset) was observed for both designs. As will be shown in this section, the stall inception process was governed by the growth of small amplitude rotating waves. Again, the plots presented for either rotor are meant to be representative of the stall inception behavior of both designs. It is worth noting that evidence of the upcoming stall could be seen in the unfiltered (no analog or digital filtering) raw Kulite signals. At the higher rotational speeds, the pressure traces were dominated by a strong signal at

the blade passing frequency (believed to be caused by shock waves passing the Kulites). As stall was approached, the 1/blade signal started oscillating in both frequency and amplitude, approximately 1-2 seconds prior to stall onset. This was observed both on-line while testing and during playback of the data. This observation is discussed further in section 5.7.

The filtered data traces obtained from the 80% speed transient for Rotor 4 (unswept) are shown in Figs. 5.13 and 5.14. The longer period indicated between the first two "pulses" of rotating stall (seen best in Fig. 5.2) was repeatable with the same rotor and was also seen in the Rotor 6 data at the same speed. Development of the rotating stall from the small amplitude modal waves can be seen clearly in Fig. 5.14. Figure 5.15 presents the amplitude and phase data of the first mode and points out some interesting features. Using the information presented in Fig. 5.15, there does not appear to be a lot of warning time prior to the instability as evidenced in both the magnitude and phase plots. Note the apparent exponential growth of the rotating waves (from $t=464$ on) just prior to stall onset. This is predicted by the stability theory discussed in section 2.3.1 (Garnier [28]). The 1/rev disturbance indicated between $t=423$ and 435 is believed to be an anomaly, as the data was filtered using a 248-pole FIR filter between 125 and 230 Hz.

The spectra obtained using the transient data set (up to, but not including stall) for Rotor 4 at 80% speed is shown in Fig. 5.16. As evidenced by the lack of any definitive peak, the

PSD does not appear to offer any additional insights into the process leading up to stall. Several of the peaks (i.e., 150 Hz, 175 Hz) are believed to be harmonics of the strong low frequency planar oscillations (fundamental frequency of 13.5 Hz) evident in all the data (see Fig. 4.5).

The stall behavior at 90% speed provided one of the more interesting comparisons between the two designs. Indeed, the development of stall from rotating waves for both rotors was again observed. Figures 5.17 and 5.18 are representative of the process for both designs. Small amplitude wave growth can be seen clearly in Fig. 5.18. The most interesting feature of the stalling process at this speed for both designs was that the waves were detected much sooner than those for any other speed examined. Evidence of this is provided in Figs. 5.19 (Rotor 4, unswept) and 5.20 (Rotor 6, swept). Both phase plots show relatively long periods of constant slope prior to stall, corresponding to a rotating disturbance at about 50% rotor frequency. Of particular interest are the SFC #1 magnitude and phase plots for Rotor 6 (Fig. 5.20). Both plots in Fig. 5.20 reveal significant energy contained in the first spatial mode for at least 260 rotor revs (0.84 s) prior to stall. The reason for this advanced stall warning time is strongly suggested by examination of the compressor overall characteristic at 90% speed (Fig. 4.2). Note that the 90% characteristics for both rotors (Figs. 4.1 and 4.2) exhibit positively-sloped regions, with the speedline for Rotor 6 being most pronounced. The effect of

speedline shape on stall precursor behavior is discussed in more detail in section 5.5.

The PSD plot of SFC #1 for Rotor 6 (swept) using the transient data up to stall is shown in Fig. 5.21. As with 80% speed (Fig. 5.16), the spectra does not reveal any distinct peaks that might be indicative of small amplitude rotating waves. The lack of information from Fig. 5.21 does not invalidate the results just described from the phase plot of Fig. 5.20. Figure 5.21 simply shows that the spectra of the first Fourier mode is complicated and contains a lot of frequencies (rotating, planar) of approximately the same magnitude.

At design speed, the stalling process was identical to that described at the other high speeds - abrupt stall characterized by growth of small amplitude circumferentially travelling waves. This is evidenced in Figs. 5.22-5.24 for the swept rotor (Rotor 6). The PSD plots of SFC #1 for Rotor 6 are shown in Fig. 5.25 using 100% speed transient data up to stall, and 0.25 and 0.5 seconds prior to stall. A very distinct rotating disturbance can be seen at approximately 170 Hz in all three plots (Fig. 5.25). Note how the peak attenuates and widens as data further from the stall was used (Figs. 5.25b and c). This attenuation suggests that the rotating waves are being damped out as the compressor moves away from the stall point, consistent with the stability theory described in section 2.3.1. Although not shown, the spectra of SFC #1 for Rotor 4 at design speed was similar to those shown in Fig. 5.16 and 5.21; no definitive peak was seen.

5.4 Stall Warning Time

In order to arrive at a more quantitative description of the stall warning time, the following procedure was adopted. The phase data of SFC #1 were smoothed using a cubic spline smoothing function (i.e., Fig. 5.26). The choice of the smoothing function inevitably affects the stall warning time, but as noted below, the criterion was developed for comparison purposes (the same order smoothing function was applied to each data set). Since the slope of the phase plot corresponds to the frequency of a rotating disturbance, the slope (derivative) of the smoothed data was calculated and plotted as a function of time up to and including stall. The stall warning time was then taken to be the last stretch of slope up to stall that fell between 30-70% rotor frequency (2-4.4 rad/rev). This criterion was developed merely to provide a consistent means of determining a stall warning time for comparison purposes. In the plots that follow, the criterion band and the onset of fully-developed stall are indicated, as well as the start time taken for stall warning (arrow).

Plots of the phase slope of SFC #1 for both rotors are shown in Figs. 5.27-5.34 for 70, 80, 90, and 100% design speed. The 60% speed data were not included because of the previously described progressive stall exhibited at this speed. The speedline characteristics provided as inserts in each figure help stimulate discussion in the next section. Emphasis is placed on the shape of the speedlines, hence they are plotted as % design

pressure ratio versus % design mass flow (refer to Figs. 4.1 and 4.2).

Table 5.1 summarizes the stall warning times as calculated following the above criterion. As can be seen from the plots and Table 5.1, Rotor 6 consistently provided more stall warning time than did Rotor 4. With the exception of 90% speed (Figs. 5.31 and 5.32), the shape of the speedlines for each rotor were quite similar. The advanced stall warning times for the swept rotor (Rotor 6) suggests a potential effect of shock waves on stall precursor waves, since the leading edge of Rotor 6 was swept back deliberately to reduce shock wave strength. Shock wave effects are also discussed later in section 5.6. In addition, essentially all of the plots show evidence of the impending stall 200-300 rotor revs prior to the instability (i.e., slope within the criterion for a 30-60 rotor rev period well before the stall, but followed by a significant stretch of the slope outside the criterion). Very good examples of this can be seen in Figs. 5.33 and 5.34 at design speed for both rotors.

5.5 Effect of Speedline Characteristic on Stall Precursor

Figures 5.35 and 5.36 show the steady-state performance characteristics of the two designs as determined using the steady conditions for which Kulite data were obtained. The high-flow condition (wide-open throttle) data points are included to provide a better determination of the speedline shape. The low-flow points at each speed provide a good indication of the

steady-state stall line. Also indicated is a best guess for the transient stall line (refer to section 4.1) determined by extending the general shape of the speedlines as shown (better indications of the speedline shapes can be seen in Figs. 4.1 and 4.2). Examination of the extended speedlines offers a potential explanation as to why the small amplitude waves were not detected at the near-stall steady conditions, but were detected in the transients very close to stall. By operating transiently to the left of the steady stall line, more of the positively sloped region of the speedlines is reached. It appears that a positively sloped characteristic (also discussed in section 2.4) could be an important consideration for advanced pre-stall indications.

This hypothesis is further substantiated by examining the stall warning times (Table 5.1 and Figs. 5.27-5.34) in relation to the speedline shapes. As seen in Figs. 5.29 and 5.30, the slope of the 80% speedline for both rotors is nearly flat (maybe slightly positive) and the stall warning time is minimal compared to the other speeds. In sharp contrast to the 80% speedline shape (and all other speeds for that matter) is the very large region of positively sloped characteristic at 90% speed for the swept design (Rotor 6). This condition provided more than 2.0 seconds of stall warning time. Note that from a design standpoint, operating in a region of large positive slope is undesirable - performance penalties are large (see for example the efficiency curve of Rotor 6 at 90% speed, Fig. 4.2).

However, operating at peak efficiency in a region of flat or slightly positive slope is desirable (i.e., maximum pressure rise), and may be beneficial from a stall warning standpoint.

Figure 5.37 is an attempt to provide some quantitative relationship between speedline slope and stall warning time. The slopes were calculated by extending a straight line through the near-stall steady-state data point following the general shape of the speedline. Results of this rather crude approximation (Fig. 5.37) point out the difficulty encountered in trying to correlate stall precursor behavior with various compressor parameters. Another potential problem here is that the statistical data sample is quite limited (i.e., each rotor was stalled transiently only once at each speed tested). Since the stalling process has a lot of random phenomena affecting its behavior, it might be more appropriate to look at some average behavior for many stalls repeated at each speed. Additionally, speedline slope is just one factor. Other important considerations were discussed in section 2.4 and include sensor location and sensitivity, throttle transient rate, flow field distortion, shock waves, and others.

5.6 Effect of Shock Waves on Stall Precursor

Figure 5.38 schematically shows the shock structure at operation close to stall of the transonic rotors tested in the current experiments. At a high-flow operating condition (unthrottled), the leading edge shock is attached and oblique to the inlet relative flow. As the flow is throttled to stall, the

shock becomes more normal to the relative flow and moves upstream to form a bow shock (Fig. 5.38). Also shown in Fig. 5.38 is the location of the Kulites used for stall precursor detection in the current investigation. With this arrangement, the modal waves rotating at about 0.5 rotor frequency must travel upstream (decaying exponentially as predicted by theory, Garnier [28]) and pass through the shock structure rotating at the blade passing frequency (40 times the modal wave frequency) in order to be detected. Within this complicated flow field, a quantitative description regarding the effect of shock waves is difficult; however, qualitatively, attenuation of the rotating waves would appear reasonable.

As indicated in Table 5.1, Rotor 6 consistently displayed more stall warning time than did Rotor 4, even in cases when the speedline shapes were virtually identical. Figure 5.39 shows the performance characteristics of both rotors on the same map to provide a good comparison of the speedline shapes. A good example can be seen in the 80% speed data for both designs; Rotor 6 had more than double the warning time of Rotor 4, yet the speedline shapes were quite similar. In fact, all the characteristics were very similar in shape except at 90% speed. Also, the tip clearances and sensor location for both designs were essentially the same, as noted in section 3.2.2. Thus, it appears that the reduced shock strength of the swept rotor (Rotor 6) had a positive effect on the ability to detect the pre-stall waves and supports the discussion in the preceding paragraph.

Although not the focus of this research, it is also interesting to note that the swept rotor stalls appeared to be less severe than the unswept rotor stalls. At 70% speed, Rotor 6 exhibited a progressive stall (Fig. 5.12), while the Rotor 4 stall was more abrupt (Fig. 5.9). Additionally, the SFC #1 amplitude plots for the swept rotor showed consistently less energy in fully-developed stall than did the unswept design (for example, see Figs. 5.19 and 5.20). The reduced severity of the Rotor 6 stalls appears to confirm the weakened shock structure of the swept design.

5.7 Comparison With Previous Investigations

Compressor stall inception for the two rotors examined was characterized by growth of small amplitude rotating waves. As measured 0.3 rotor radii upstream at the blade tips, the perturbations were initially 0.2 psi peak-to-peak. The waves did not grow significantly until just prior to the instability, when exponential growth into fully-developed stall occurred very rapidly, typically within 6-10 rotor revolutions.

The features described in the preceding paragraph support the modal wave representation of the stall inception process, schematically shown in Fig. 2.3. Results are qualitatively quite similar to those obtained from recent experiments on low-speed compressors (McDougall, et al. [2] and Garnier, et al. [3]) and one high-speed compressor (Garnier, et al. [3]). Figure 2.4 provides an example of Garnier's, et al. [3] results from a low-

speed machine. The similarities of the results from the current work (see, for example Figs. 5.19 and 5.20) with the features shown in Fig. 2.4 are readily apparent. The planar oscillations evident in the present results probably affected when the modal waves could initially be detected (see Fig. 5.3). Regardless, the basic mechanism of stall inception was clear - stall evolved smoothly from small amplitude circumferentially travelling waves.

It is worth mentioning that the high-speed results presented by Garnier, et al. [3] showed the second harmonic of the rotating waves (SFC #2) to be at least as important as the first mode. The present work focused on the first mode for reasons discussed in section 4.3 (a lot of unwanted frequencies, most of the energy appeared to be in SFC #1, etc.). The higher harmonics were examined only briefly and probably warrant more study. Given that the rotating stall frequencies of both designs were approximately 50% of rotor frequency, examination of higher order modes would require additional signal processing in order to resolve the second harmonic and the 1/rev signal. Time did not allow this additional processing to be performed in the current investigation.

Finally, another aspect of the stalling process that deserves some discussion is the high-frequency content that was filtered out of all the data presented here. As mentioned in section 5.3.3, the raw (unfiltered) Kulite signals obtained at 70% speed and above were dominated by a very strong (3-4 psi peak-to-peak) 1/blade frequency generated by the passing shock

waves (see Fig. 5.38). At 60% speed, the entire span was subsonic and the 1/blade frequency was not as evident. It was observed both on-line and during data playback that during the transients to stall, the 1/blade signals would start modulating in both frequency and amplitude (perhaps at 27 Hz). The modulations could be seen approximately 1-2 seconds prior to stall and would grow as stall was approached. This observation raises the question of whether the high-frequency signals due to shock passing (6.9 kHz at design for the current rotors) might provide a useful indicator of impending stall, particularly in high-speed machines.

6.0 CONCLUSIONS AND RECOMMENDATIONS

6.1 Summary

Two single-stage, transonic compressor designs were tested to characterize the process leading up to aerodynamic stall. The two rotors had identical design points (speed, pressure ratio, mass flow) and were tested in the same rig under the same operating conditions. This allowed for comparison of the stall inception behavior of the two rotors in terms of the one parameter that defined their design difference - leading edge sweep (shock wave strength). To quantify the stalling behavior, measurements were obtained from eight high-response pressure transducers equally spaced in a plane 0.3 rotor radii (2.5 inches) upstream of the blade leading edge tips. Data were obtained under both near-stall steady and transient compressor operating conditions. In addition to studying the raw pressure traces, the signals were spatially and temporally resolved using Fourier techniques. Only low-frequency content was examined in detail, and additional digital filtering was used to enhance features in the frequency range of interest (50% of rotor frequency).

6.2 Conclusions

The following conclusions are aimed at answering the questions posed in section 1.4 of this report. As is the case with most research activities, the results of the current work

introduced several additional key issues. These are addressed primarily in the recommendations section.

(1) The transient stalling process of both rotors was associated with the growth of small amplitude rotating waves (modal waves) for all speeds tested. Initial wave amplitude was approximately 0.2 psi and did not grow significantly until 6-10 rotor revolutions prior to stall. The waves were evident regardless of the type of stall - progressive or abrupt - and in the presence of small amplitude, surge-like oscillations.

(2) Compressor operating condition did not seem to affect the basic mechanism of stall inception - small amplitude wave growth. However, the length of time the waves could be detected prior to compressor stall (stall warning time) did appear to be related to the shape of the pressure rise - mass flow characteristic (speedline).

(3) A positively sloped region of speedline characteristic appeared to be key for detection of the modal waves. The small amplitude rotating waves were not apparent in any of the near-stall steady data taken at speeds that exhibited an abrupt stall. When the compressor was operated transiently at the same speeds, the rotating waves were detected. Transient stall occurred at a lower flow rate than at the steady-state stall (Figs. 5.35 and 5.36), and resulted in more of the positively sloped characteristic being reached. Additionally, speedlines with relatively large positively sloped regions resulted in more advanced stall warning times (Figs. 5.31 and 5.32).

(4) The presence of shock waves in the compressor flow field appeared to interfere with detection of the rotating waves, probably by attenuating the perturbations. In all cases where the speedline shapes of the two rotors were virtually identical, the swept rotor (Rotor 6) exhibited more stall warning time than the unswept design. The intent of leading edge sweep on Rotor 6 was to minimize shock losses by reducing shock strength; the reduced shock strength⁶ appeared to favor advanced detection of the modal waves.

(5) The effects of speedline shape and shock waves discussed above and in sections 5.5 and 5.6 are important to sensor location, particularly in a multistage environment. In a multistage compressor, one would have to be concerned with individual stage characteristics as well as operating condition (a multistage compressor is more likely to stall in the front stages during low-speed operation (starting); this is not necessarily true at high-speed operation). Results of the current investigation, as well as those from previous investigations (Garnier [28] and Bonnaure [20]; see section 2.4) indicate that maximum stall warning times would require multiple sensor locations and/or advanced knowledge of the stage which initiates the stall.

(6) A considerable amount of digital data processing was

⁶Note that shock wave strength was not characterized in the current test programs. However, the swept rotor consistently exhibited less severe stalls than the unswept design, offering further evidence of a weakened shock structure (section 5.6).

required to obtain the stall warning times listed in Table 5.1. The processing included band-pass filtering, spatial Fourier transformation, data smoothing, and slope calculation. Ideally, for use of the modal waves as a pre-stall indicator for an active engine control scheme, one would desire minimal processing. Each required processing step would increase the amount of stall warning time needed to evaluate the signals and take action to avoid or suppress the impending stall.

6.3 Recommendations

Results presented in this report have contributed to the physical understanding of the stall development process in two compressor designs that are typical of those used in aircraft gas turbine engine applications. These results and the potential benefits of identifying a reliable stall precursor (discussed in section 1.1) warrant continued exploration of the stall inception process in compressors. Questions regarding the general application of the current results, as well as the robustness of the small amplitude waves, must be addressed before any practical applications can be realized. The following recommendations outline a few of these issues, with emphasis on the experimental side. It should be noted, however, that quantitative experimental results are essential if improvements in the modelling of high-speed compressor stability are to be realized.

- (1) Stall inception investigations should continue on various single-stage and multistage compressor designs, with

emphasis on high-speed machines. The stability theories appear to predict quite well the behavior of low-speed machines, but are in need of quantitative compressibility effects (blade passage choking, shock waves, stage mismatching, etc.) to accurately model high-speed compressor stall inception.

(2) Whenever possible, several axial locations for high-response measurements should be used. Ideally, a measurement set would be made at the inlet, exit, and each compressor stage to help quantify the effects mentioned above. From a practical standpoint, this would result in very large data storage problems (see section 4.2) and/or very expensive analog recording equipment.

(3) If the equipment is available, storage of the unfiltered stall inception data on magnetic tape should be considered as the most attractive alternative. As was evidenced with the current data set, the advantages of magnetic tape storage - re-examining raw signals, investigating different filter/sampling combinations, etc. - proved to be quite useful, and more importantly, provided additional information.

(4) Examination of the high frequency content in stall inception data should be performed. A good starting point would be the data set collected from the current study. As discussed in section 5.7, the strong signal at the blade passing frequency exhibited modulations in both frequency and amplitude as stall was approached. The nature of these modulations should be studied to investigate their potential as a stall warning

indication in high-speed compressors. An attractive feature of these 1/blade signals is that axial sensor location would not be as critical as it appears to be for detection of the small amplitude modal waves. The strong 1/blade signal is closely tied to the passing shock waves, which are typically confined to the first (and maybe second) compressor stage.

(5) Additional investigations should include sets of closely spaced transducers to better examine short length scale phenomena on the stalling process (i.e., 2 or 3 transducers over 1 or 2 blade passages). Ideally, these measurements would be obtained simultaneously with the equally spaced measurements, but could be performed separately provided advanced provisions had been made (i.e., holes drilled in the rig).

Finally, it is appropriate to make some comments that apply specifically to the Compressor Aerodynamic Research Laboratory (CARL), the facility used in the current study. The nature of the work conducted in the CARL regarding parametric blade studies makes it ideally suited for continued stall inception investigations. Transient data recording capabilities would have to be increased in order to address the issues presented above, and provide a complete picture of the stall inception process. Tests conducted with different throttle closure rates and distorted inlet flow fields would also be important.

7.0 REFERENCES

1. Ludwig, G.R., and Nenni, J.P., "Tests of an Improved Rotating Stall Control System on a J-85 Turbojet Engine," ASME Journal of Engineering for Power, October 1980, Vol. 102, pp. 903-911.
2. McDougall, N.M., Cumpsty, N.A., and Hynes, T.P., "Stall Inception in Axial Compressors," Transactions of the ASME, Journal of Turbomachinery, January 1990, Vol. 112, pp. 116-125.
3. Garnier, V.H., Epstein, A.H., and Greitzer, E.M., "Rotating Waves as a Stall Inception Indication in Axial Compressors," ASME Paper 90-GT-156, June 1990.
4. "MIT Seeks Methods of Controlling Engine Compressor Surges, Stalls," Aviation Week & Space Technology, November 28, 1988, pp. 71-73.
5. Hosny, W.M., Leventhal, L., and Steenken, W.G., "Active Stabilization of Multistage Axial-Compressor Aerodynamic System Instabilities," ASME Paper 91-GT-403, June 1991.
6. Paduano, J., Epstein, A.H., Valavani, L., Longley, J.P., Greitzer, E.M., and Guenette, G.R., "Active Control of Rotating Stall in a Low Speed Axial Compressor," ASME Paper 91-GT-88, June 1991.
7. Day, I.J., "Stall Inception in Axial Flow Compressors," ASME Paper 91-GT-86, June 1991.
8. Benrey, R. (ed.), "Goodbye Stagnation: America's finest fighter outgrows a childhood ailment," Technology In Brief, United Technologies, Hartford, Connecticut, 1979, Issue Two.
9. Wisler, D.C., "Advanced Compressor and Fan Systems," A Short Course on Aeropropulsion, Dayton, Ohio, December 1987.
10. Epstein, A.H., Ffowcs Williams, J.E., and Greitzer, E.M., "Active Suppression of Aerodynamic Instabilities in Turbomachines," AIAA Journal of Propulsion and Power, March-April 1989, Vol. 5, No. 2, pp. 204-211.
11. Day, I.J., "Active Suppression of Rotating Stall and Surge in Axial Compressors," ASME Paper 91-GT-87, June 1991.
12. Greitzer, E.M., "REVIEW-Axial Compressor Stall Phenomena," Transactions of the ASME, Journal of Fluids Engineering, June 1980, Vol. 102, pp. 134-151.
13. Davis, M.W., Jr., "A Post-Stall Compression System Modeling Technique," AEDC-TR-86-34, Arnold AFB, TN, February 1987.

14. Copenhaver, W.W., Stage Effects on Stalling and Recovery of a High-Speed 10-Stage Axial-Flow Compressor," WRDC-TR-90-2054, Wright-Patterson AFB, OH, June 1990.
15. Gorrell, S.E., "An Experimental Study of Exit Flow Patterns in a Multistage Compressor in Rotating Stall," WRDC-TR-90-2083, Wright-Patterson AFB, OH, November 1990.
16. Small, C.J., and Lewis, J.T., "High Speed Compressor Rig as a Stall Recovery Research Tool," AIAA Paper 85-1428, July 1985.
17. Hosny, W.M., and Staenken, W.G., "Aerodynamic Instability Performance of an Advanced High-Pressure-Ratio Compression Component," AIAA Paper 86-1619, June 1986.
18. Boyer, K., and O'Brien, W., "Model Predictions for Improved Recoverability of a Multistage Axial-Flow Compressor," AIAA Paper 89-2687, July 1989.
19. O'Brien, W.F., and Boyer, K.M., "Stall and Recovery in Multistage Axial Flow Compressors," AGARD Conference Proceedings No. 468, Unsteady Aerodynamic Phenomena in Turbomachines, February 1990, pp. 26-1 - 26-11.
20. Bonnaure, L.P., "Modelling High Speed Multistage Compressor Stability," Master's Thesis, Massachusetts Institute of Technology Dept. of Aeronautics and Astronautics, September 1991.
21. Emmons, H.W., Pearson, C.E., and Grant, H.P., "Compressor Surge and Stall Propagation," Transactions of the ASME, Vol. 77, May 1955, pp. 455-469.
22. Stenning, A.H., "Rotating Stall and Surge," ASME Journal of Fluids Engineering, Vol. 102, March 1980.
23. Fabri, J., "Growth of a Perturbation in an Axial Flow Compressor," Transactions of the ASME, Journal of Engineering for Power, Vol. 101, January 1979, pp.87-94.
24. Nenni, J.P., and Ludwig, G.R., "A Theory to Predict the Inception of Rotating Stall in Axial Flow Compressors," AIAA Paper 74-528, June 1974.
25. Longley, J.P., and Hynes, T.P., "Stability of Flow Through Multistage Axial Compressors," Transactions of the ASME, Journal of Turbomachinery, Vol. 112, January 1990, pp.126-132.
26. Moore, F.K., A Theory of Rotating Stall of Multistage Axial Compressors, NASA Contractor Report 3685, Lewis Research Center, July 1983.

27. Moore, F.K., and Greitzer, E.M., A Theory of Post-Stall Transients in Multistage Axial Compression Systems, NASA Contractor Report 3878, Lewis Research Center, March 1985.
28. Garnier, V.H., Experimental Investigation of Rotating Waves as a Rotating Stall Inception Indication in Compressors, GTL Report #198, Gas Turbine Laboratory, Massachusetts Institute of Technology, November 1989.
29. Law, C.H., and Puterbaugh, S.L., "Parametric Blade Study Test Report Rotor Configuration No. 4," AFWAL-TR-88-2110, Wright-Patterson AFB, OH, November 1988.
30. "PRO-MATLAB for Sun Workstations, User's Guide," The MathWorks, Inc., 21 Eliot Street, South Natick, MA 01760, January 1990.
31. Greitzer, E.M., "Surge and Rotating Stall in Axial Flow Compressors," Parts I and II, Transactions of the ASME, Journal of Engineering for Power, Volume 98, April 1976, pp. 190-217.
32. Oppenheim, A.V., and Schafer, R.W., Discrete-Time Signal Processing, Prentice-Hall, Inc., Englewood Cliffs, NJ, 07632, 1989.
33. Stearns, S.D., and Hush, D.R., Digital Signal Analysis, Prentice-Hall, Inc., Englewood Cliffs, NJ, 07632, 1990.
34. Paduano, J.M., "Active Control of Rotating Stall in Axial Compressors," Ph.D. Dissertation, Massachusetts Institute of Technology, Dept of Aeronautics and Astronautics, February 1992.

Table 3.1 Facility Operating Parameters

Speed Range	6000 - 21,500 rpm
Flow Range	20 - 60 lbm/sec
Rotor Tip Diameter	14 - 19 inches
Inlet Total Pressure	6 - 15 psia
Steady-State Pressures	160 + channels
High Frequency Pressures	12 channels
Dynamic Strain	10 channels rotating
	20 channels stationary
Rotor Tip Clearance	8 channels

Table 3.2 Rotor/Stator Design Features¹

Design Speed	20,222 rpm
# of Stages	1
IGVs	None
Tip Radius ²	8.50
Hub Radius ²	2.65
Mean Radius ²	5.58
Rotor/Stator Gap	0.88 tip; 0.29 hub

	# Blades	Mid-Chord	Camber ³	Stagger ⁴	Twist ⁴	Solidity ⁵	Aspect Ratio ⁵
Rotor 4	20	3.95	12.98	44.62	46.86	2.20	1.32
Rotor 6	20	4.34	11.97	30.10	41.85	2.28	1.25
Stator	31	2.25	45.30	14.75	4.86	1.78	1.25

Notes:

1. all dimensions in inches and degrees
2. at leading edge
3. at mean radius
4. Twist defined as tip stagger - hub stagger
5. Aspect Ratio defined as mean span divided by the average of chord at hub, mean, and tip

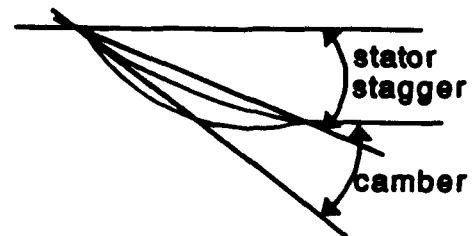
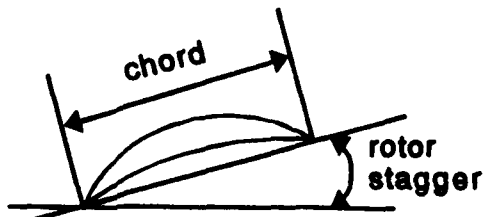


Table 3.3 Steady-State Uncertainty Analysis

a. Mass Flow Calculation Uncertainty

%N _c	Parameter Magnitude (lbm/s)	Uncertainty: 95% CI		Uncertainty: 99% CI	
		± Actual	± % Read	± Actual	± % Read
40	22.611	0.339	1.500	0.474	2.095
80	49.309	0.264	0.536	0.373	0.756
100	61.913	0.260	0.420	0.366	0.591

b. Pressure Ratio Calculation Uncertainty

%N _c	Parameter Magnitude	Uncertainty: 95% CI		Uncertainty: 99% CI	
		± Actual	± % Read	± Actual	± % Read
40	1.122	0.005	0.404	0.005	0.490
80	1.580	0.001	0.063	0.002	0.127
100	1.921	0.001	0.077	0.003	0.161

Table 3.4 Kulite Performance Characteristics

Rated Pressure	100 psig
Maximum Pressure	200 psig
Operational Mode	Differential
Excitation Voltage	15 VDC
Maximum Excitation	20 VDC
Sensitivity	1.50 mV/psi
Zero Pressure Output	< \pm 5% Full Scale
Temperature Range	-40 °F to 500 °F

Table 3.5 Kulite Calibration Data

Input Press. (psig)	Output Voltage (V)							
	Kulite #							
	1	2	3	4	5	6	7	8
5.0	2.000	2.000	2.000	2.000	2.000	2.000	2.000	2.000
2.0	0.796	0.783	0.770	0.796	0.851	0.806	0.800	0.791
1.0	0.396	0.376	0.359	0.396	0.458	0.409	0.403	0.386
0.5	0.195	0.174	0.155	0.200	0.270	0.208	0.203	0.186
0.2	0.075	0.053	0.032	0.080	0.150	0.089	0.085	0.067
0.1	0.032	0.013	0.013	0.040	0.111	0.049	0.044	0.026

Table 4.1 Frequency Range of Band-pass Filters

% SPEED	FREQUENCY BAND-PASS (HZ)
60	60-180
70	60-220
80	125-230
90	130-230
100	130-230

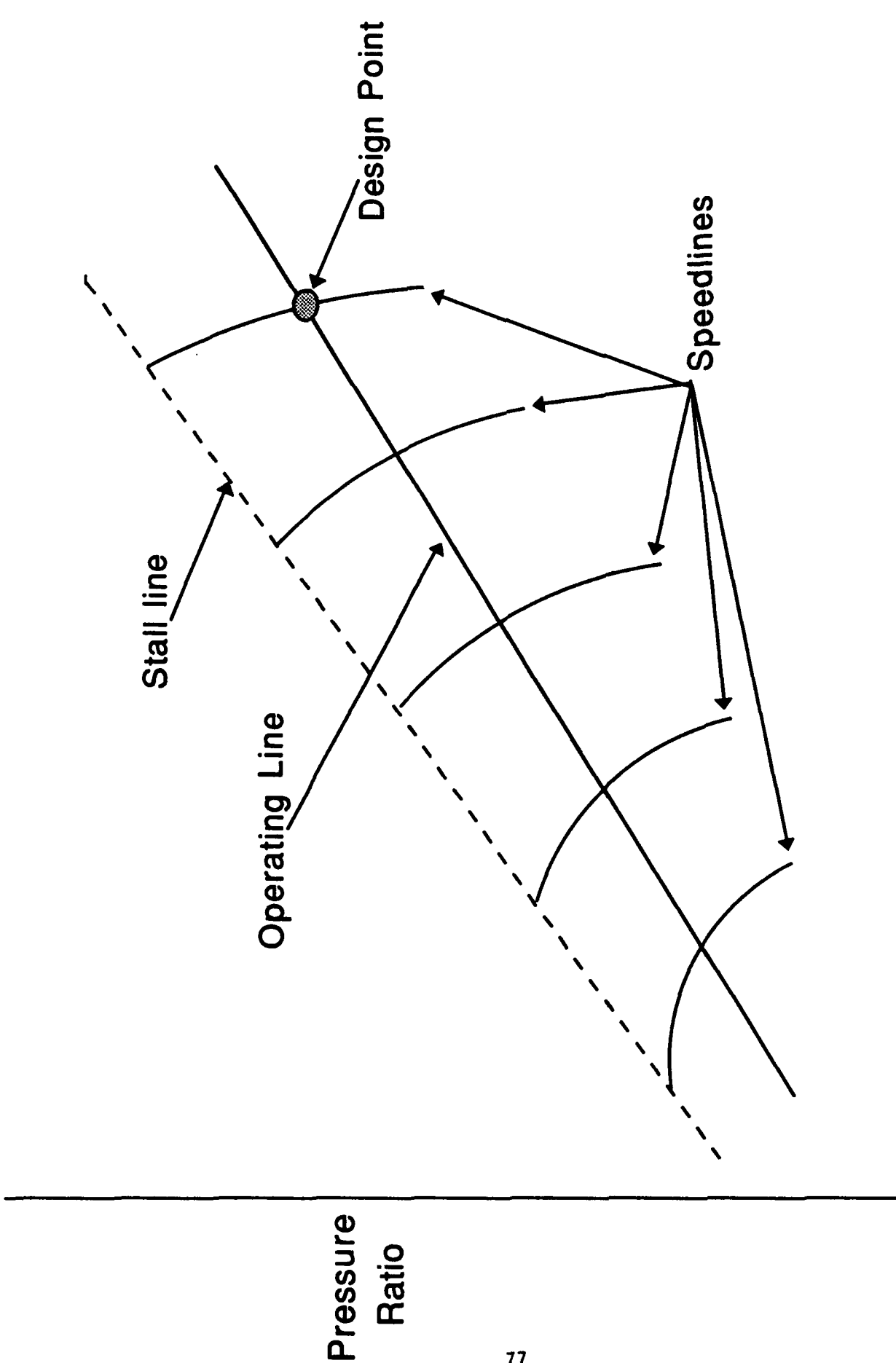
Table 5.1 Stall Warning Time

**Criterion: Last stretch of slope up to stall of SFC #1
between 30-70% rotor frequency**

% SPEED	ROTOR 4 (UNSWEPT)	ROTOR 6 (BACKWARD SWEPT)
60	slow, progressive stall	slow, progressive stall
70	<0.10 sec ¹	slow, progressive stall
80	<0.10 sec ¹	0.2 sec ²
90	0.35 sec ²	>2.0 sec ²
100	0.1 sec ¹	0.2 sec ^{1,2}

Notes:

1. significant period where criterion met (30-60 rotor revs) well before the stall, but separated by a significant period of random slope.
2. includes brief periods with slope outside criterion.



Compressor Airflow

Figure 1.1 Schematic of compressor map

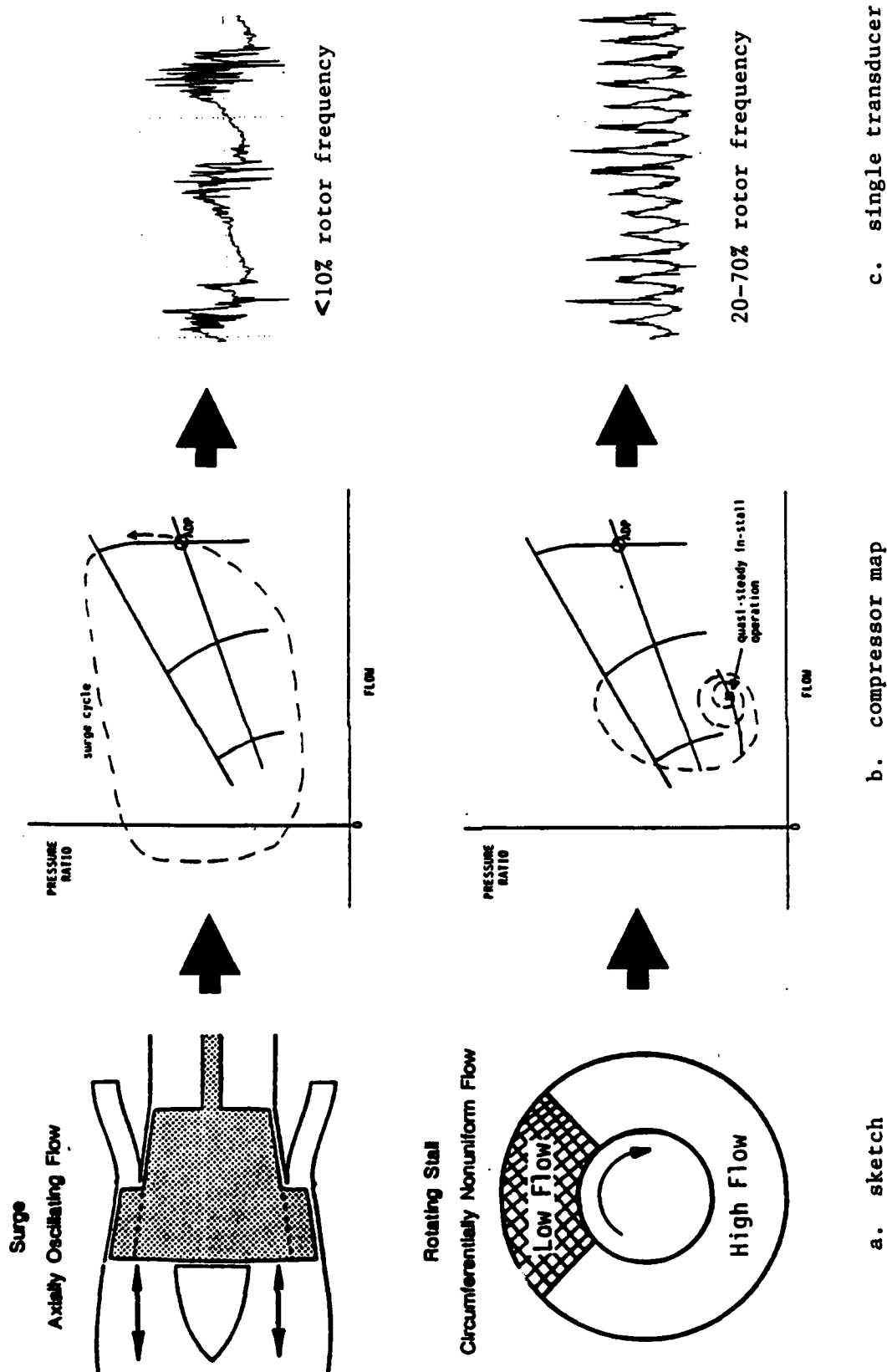
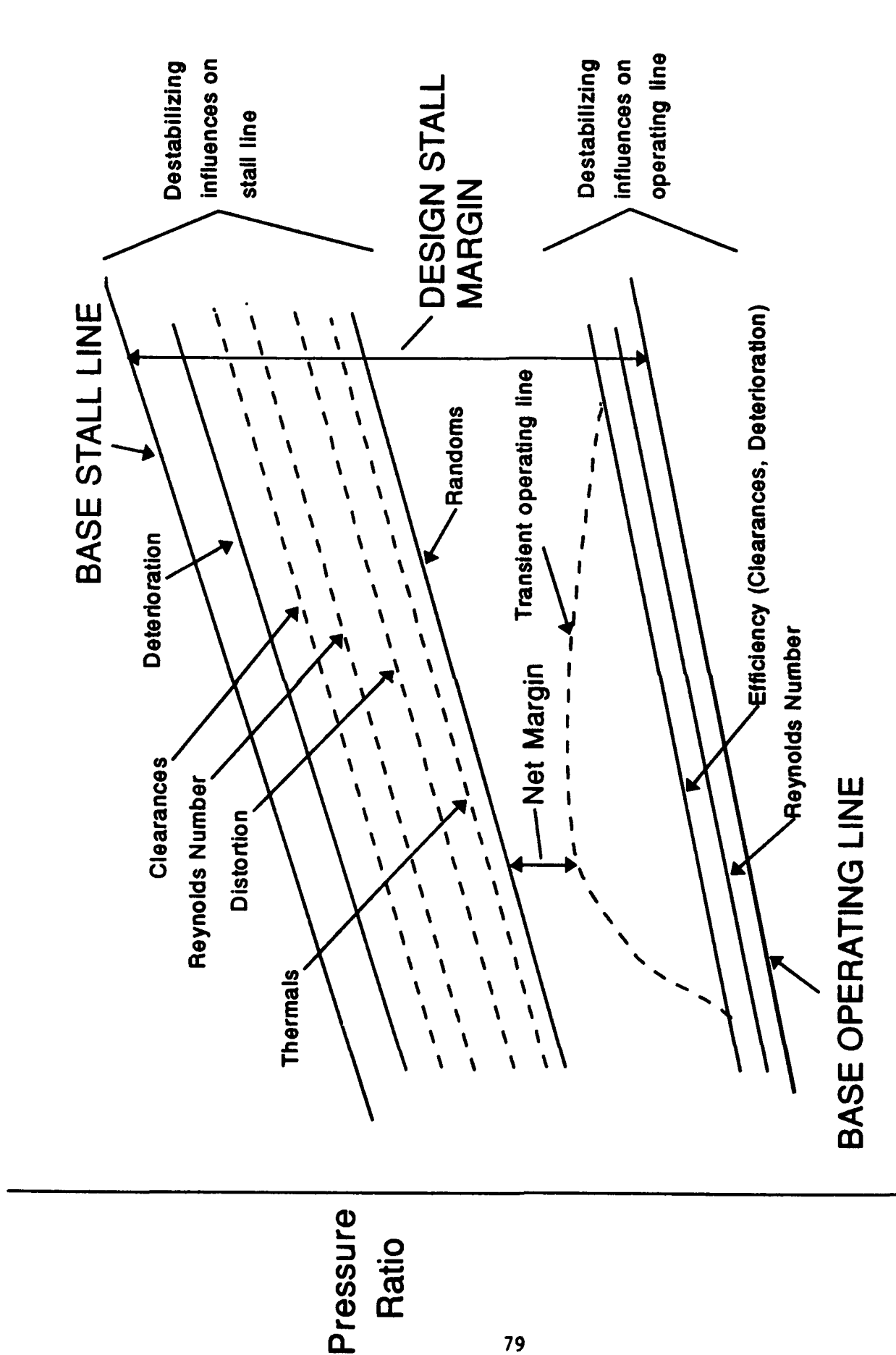


Figure 1.2 Compressor instabilities - surge and rotating stall



Compressor Airflow

Figure 1.3 Compressor stability audit

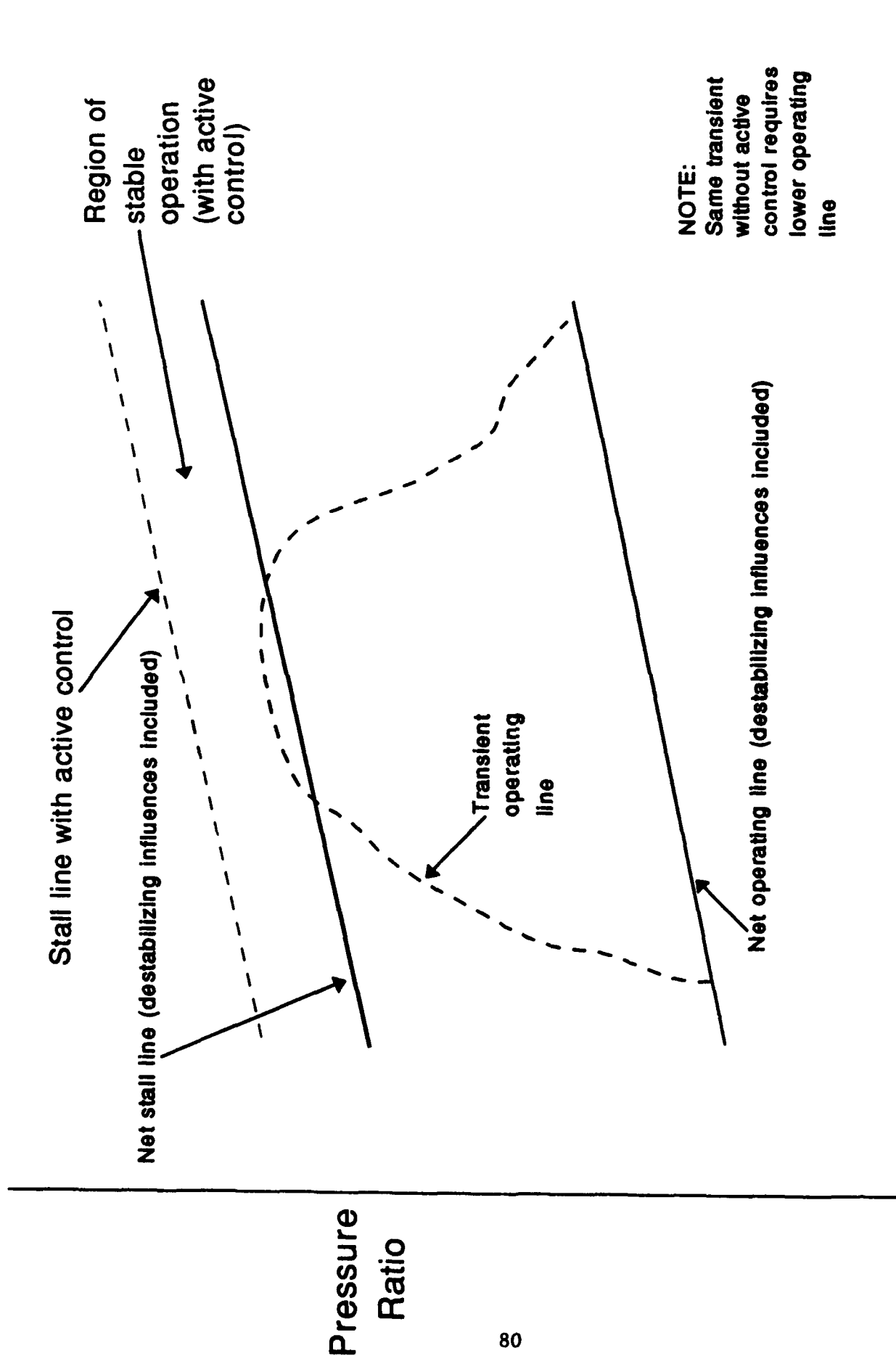


Figure 1.4 Active compressor stabilization

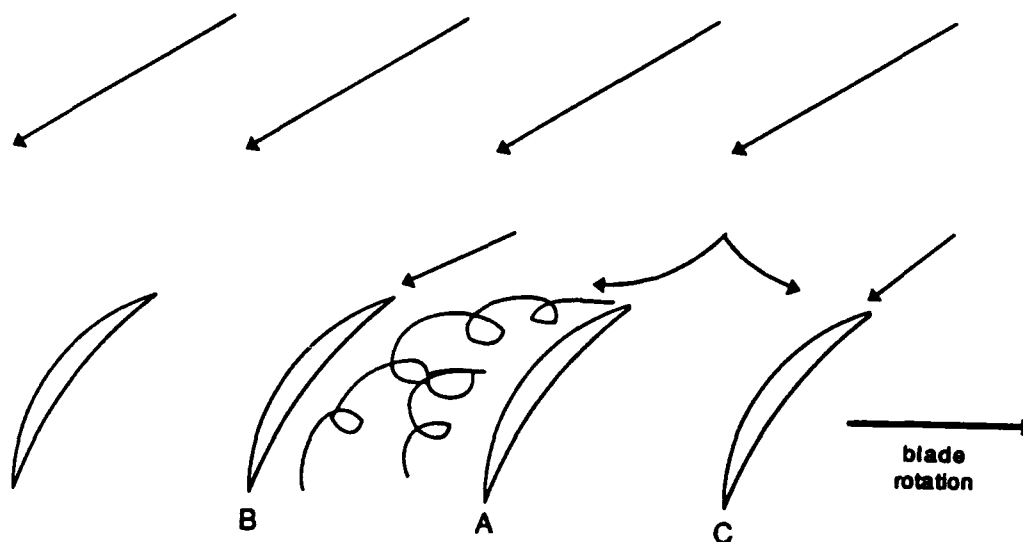


Figure 2.1 Emmons model of rotating stall

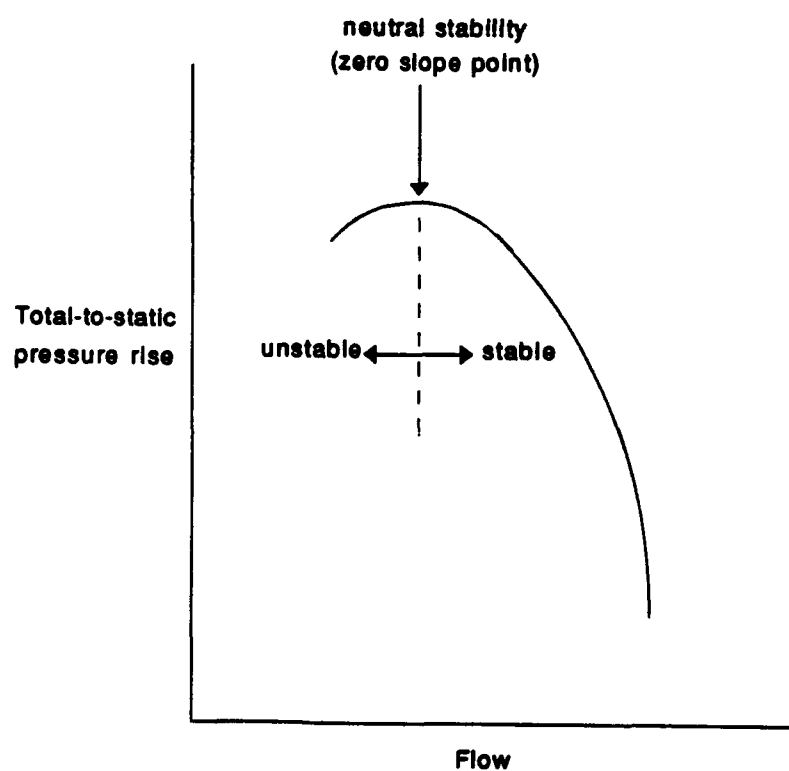


Figure 2.2 Typical compressor stability criterion

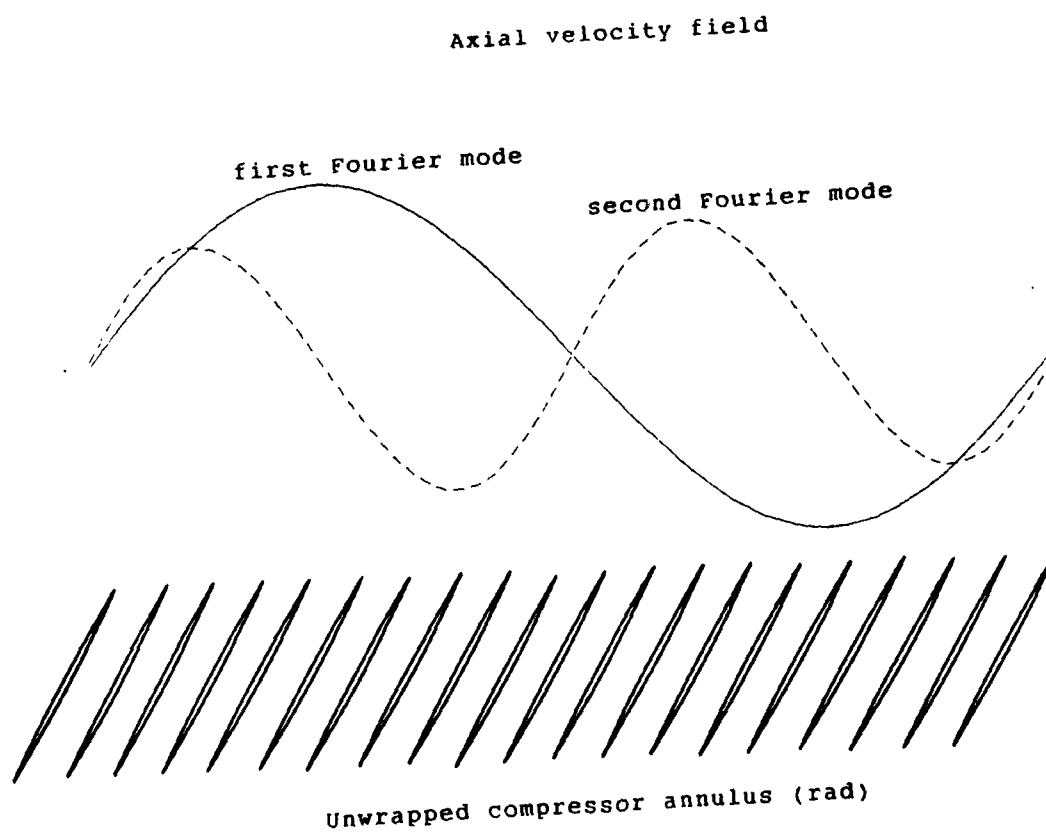
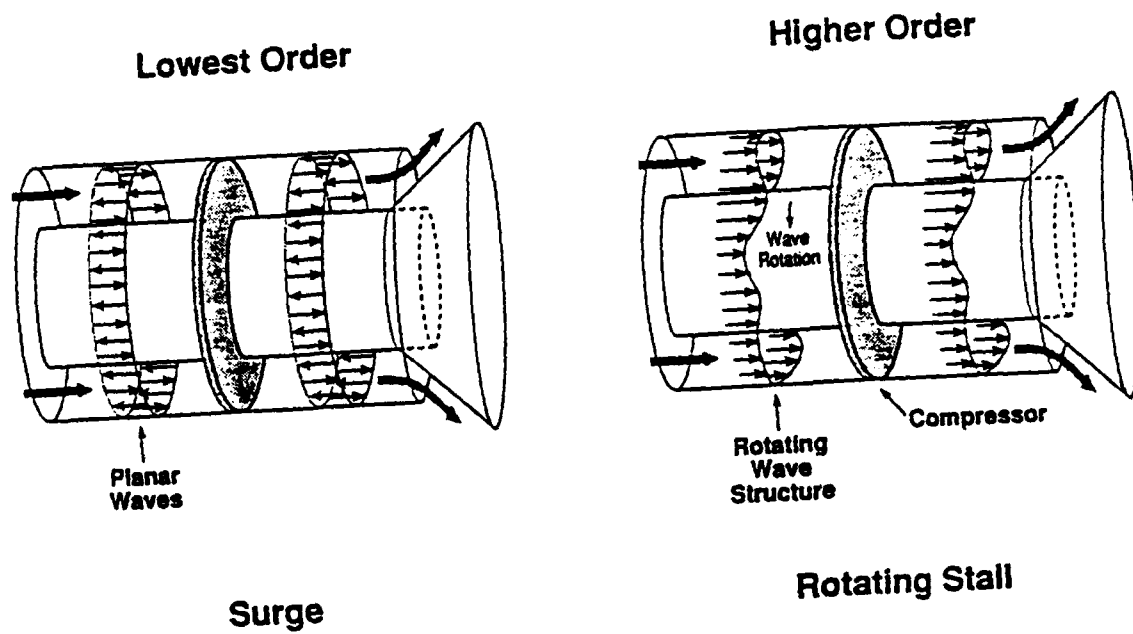
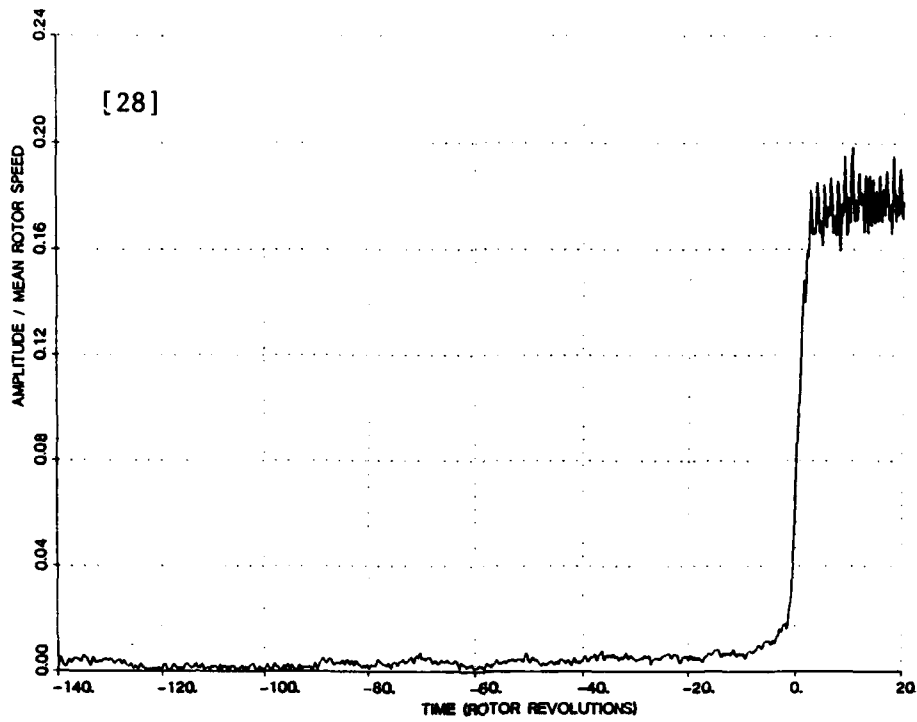
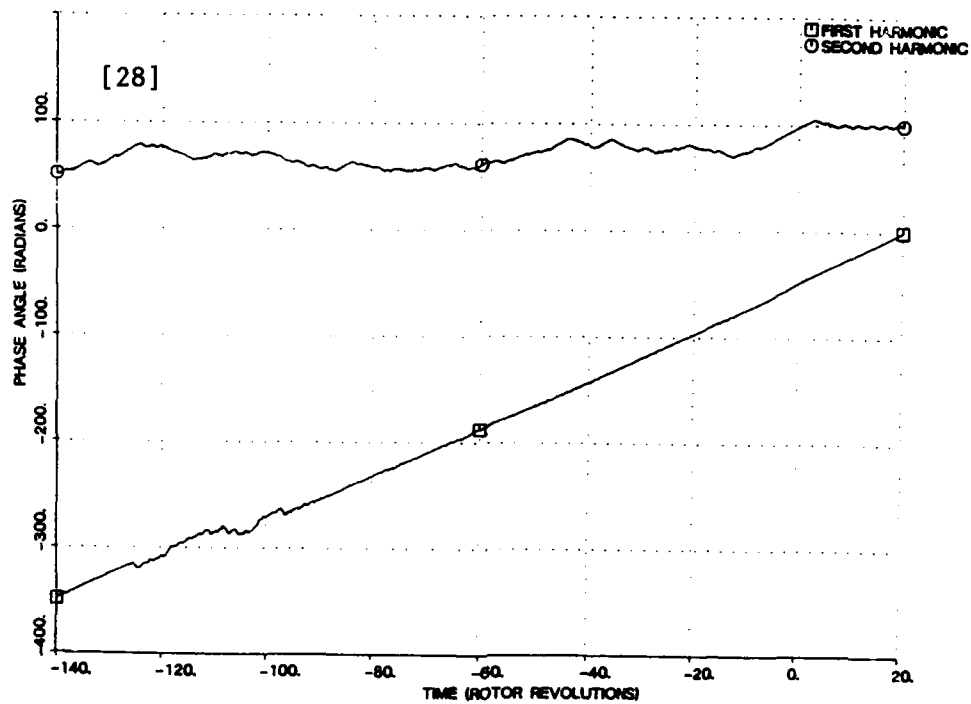


Figure 2.3 Modal wave view of compressor instabilities



a. amplitude



b. phase

Figure 2.4 Spatial Fourier coefficient analysis of modal waves [28]

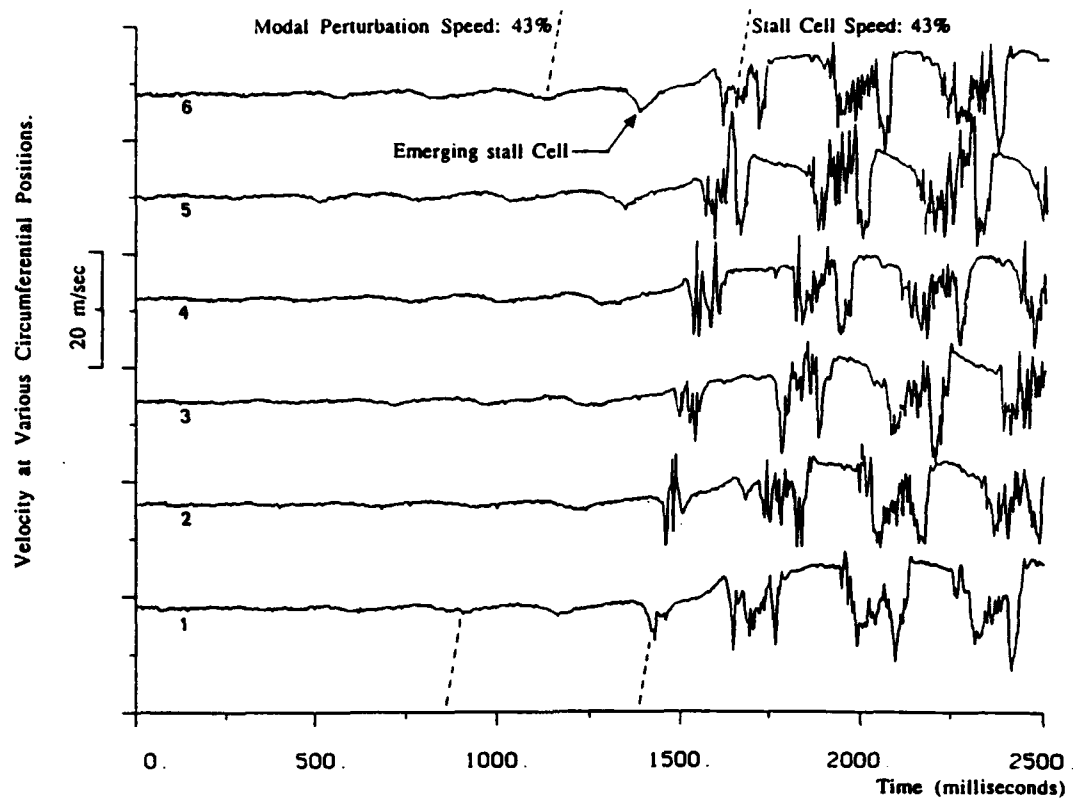


Figure 2.5 Coupling between modal waves and finite cells [7]

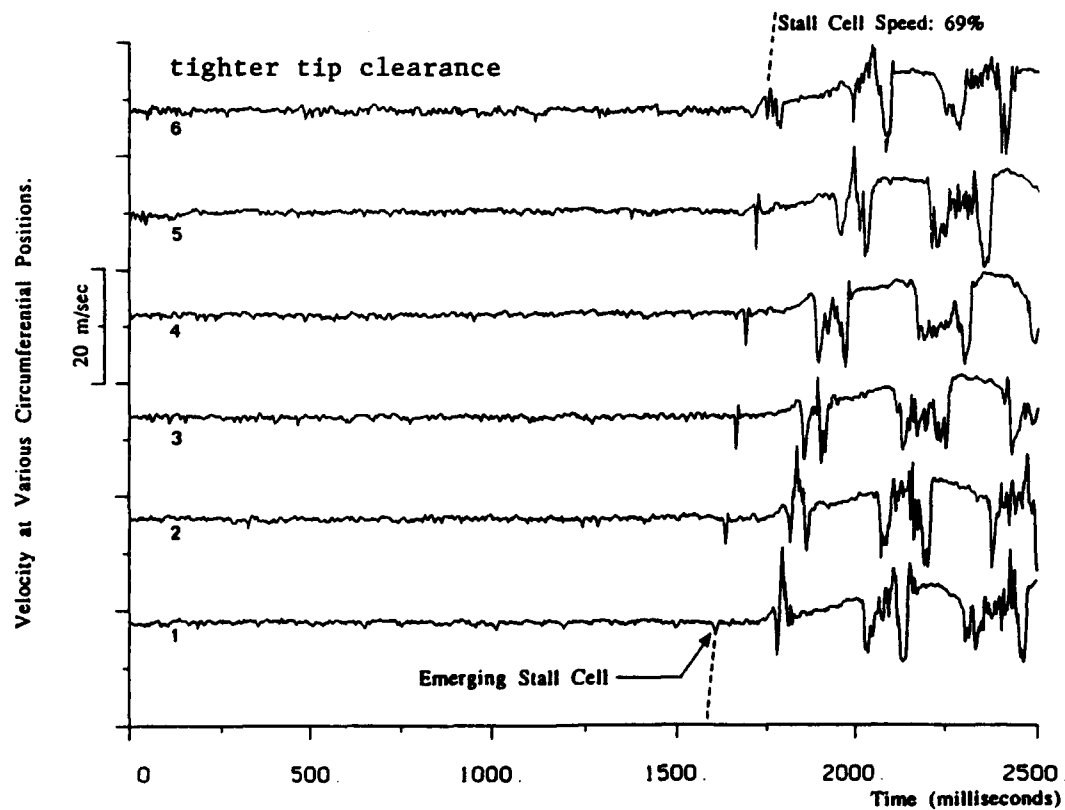


Figure 2.6 Stall inception via finite cells [7]

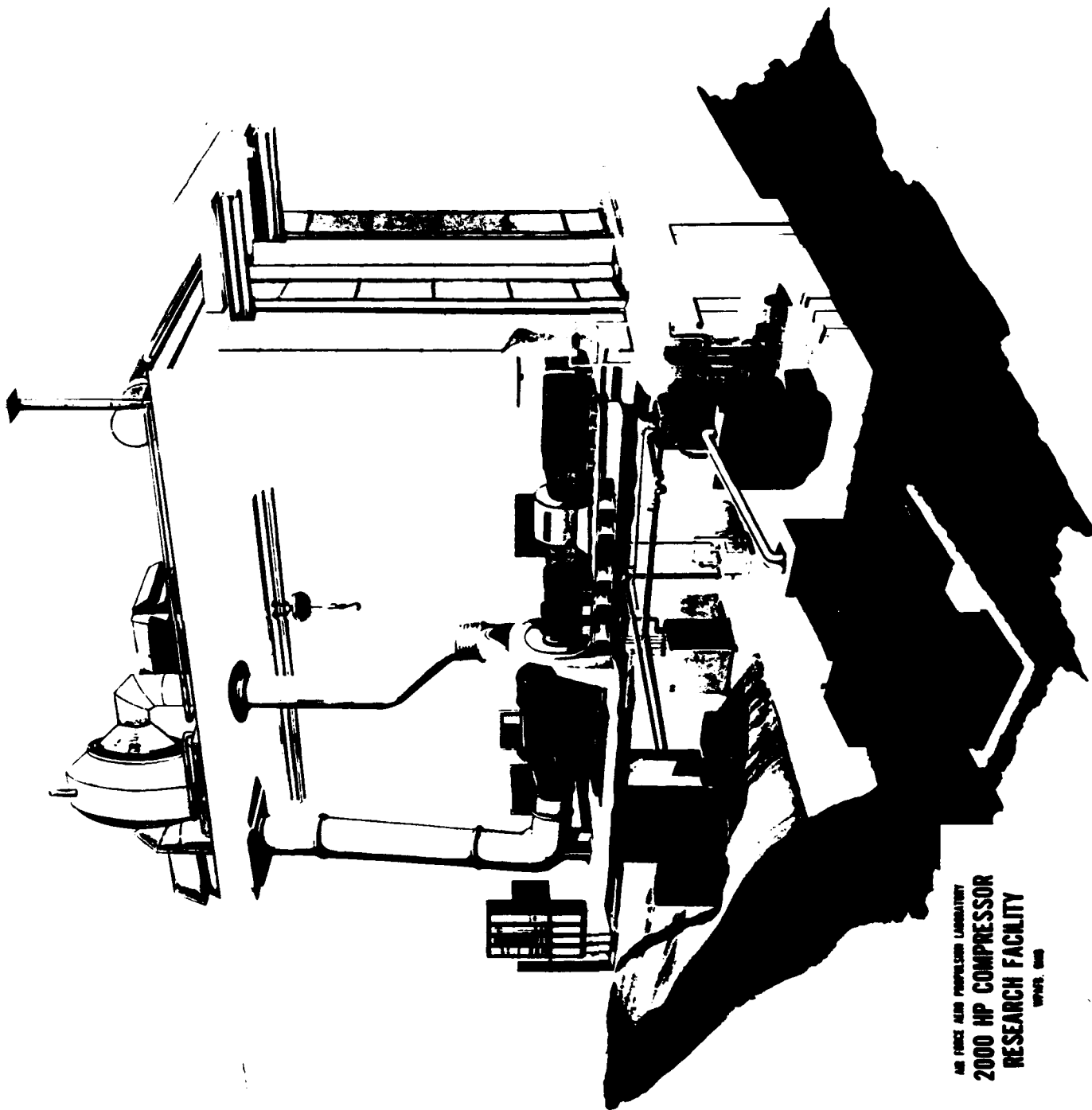


Figure 3.1 Compressor Aerodynamic Research Laboratory (CARL)

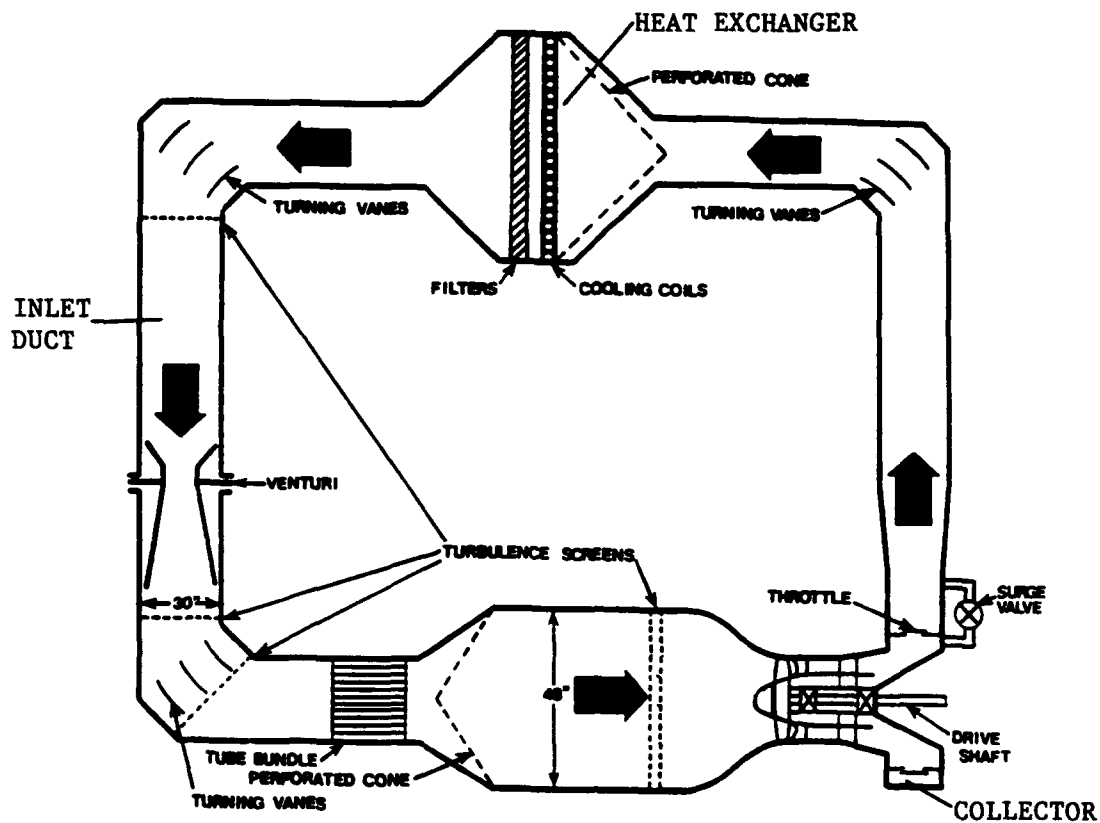


Figure 3.2 Schematic of 2000-hp test facility

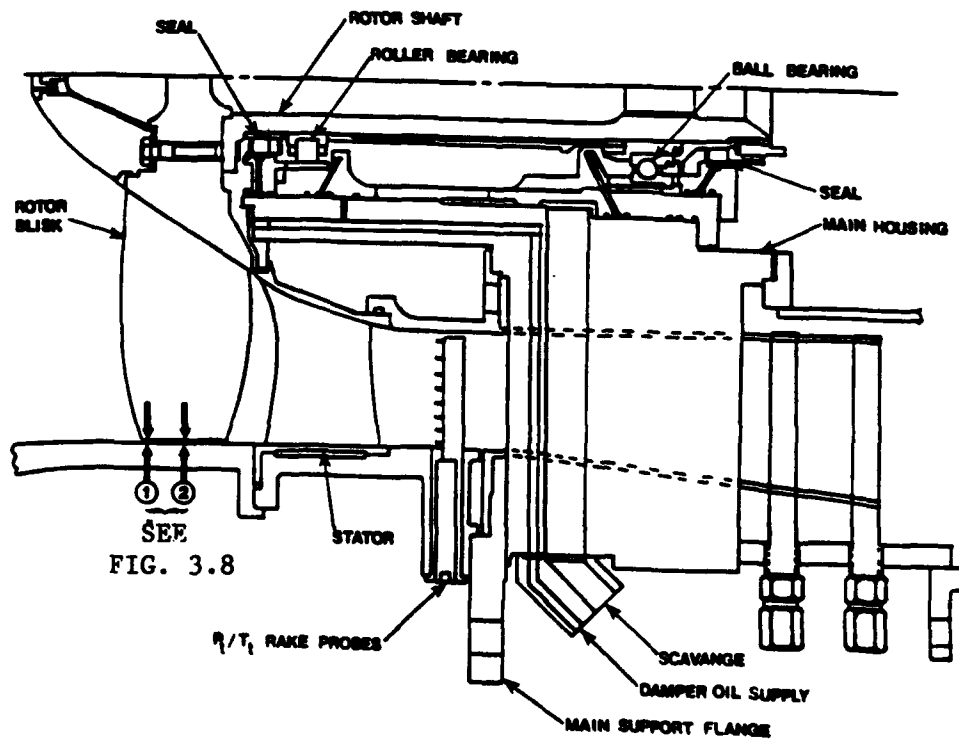


Figure 3.3 Cross-section of compressor rig [29]



Figure 3.4 Rotor 4 installed



Figure 3.5 Rotor 6 installed

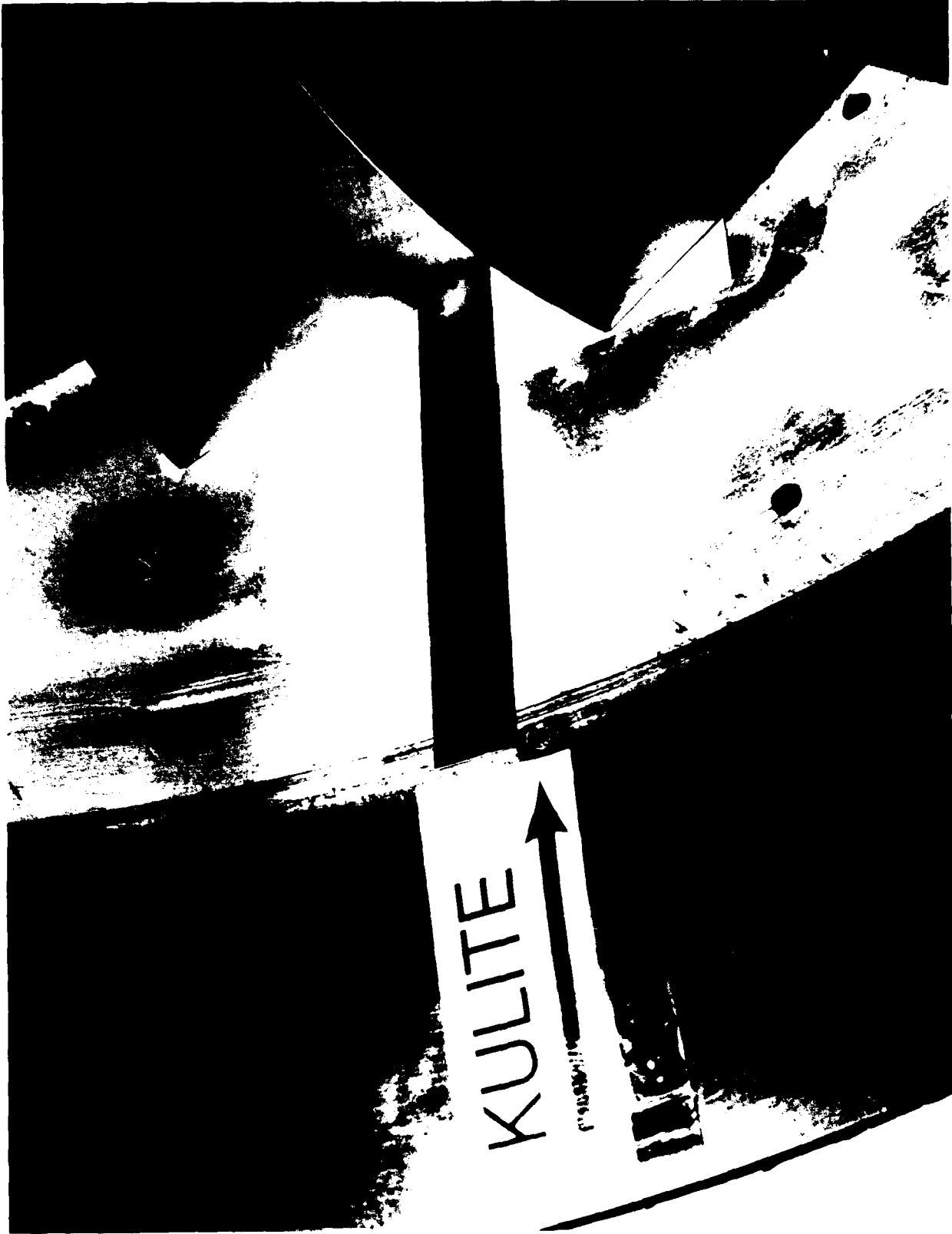


Figure 3.6 Close-up of Rotor 4 showing Kulite location



Figure 3.7 Close-up of Rotor 6 showing Kulite location

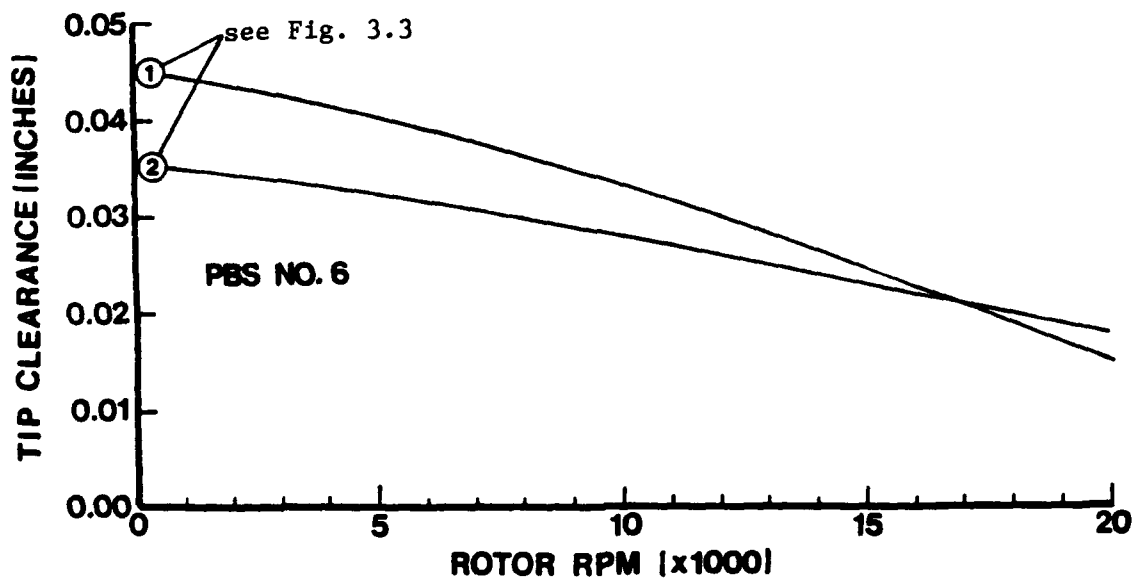
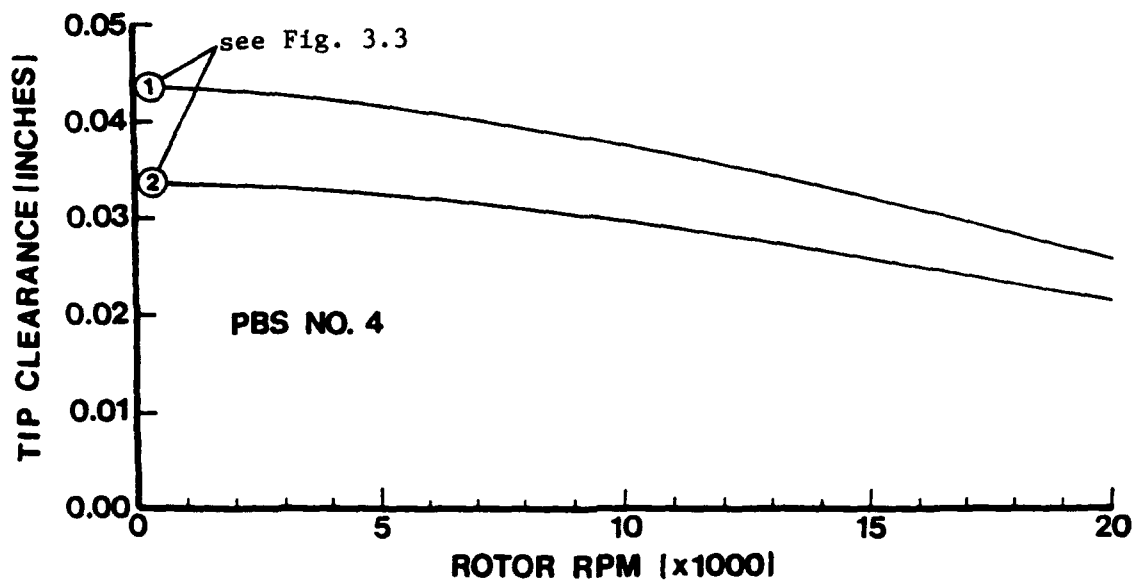


Figure 3.8 Rotor tip clearances

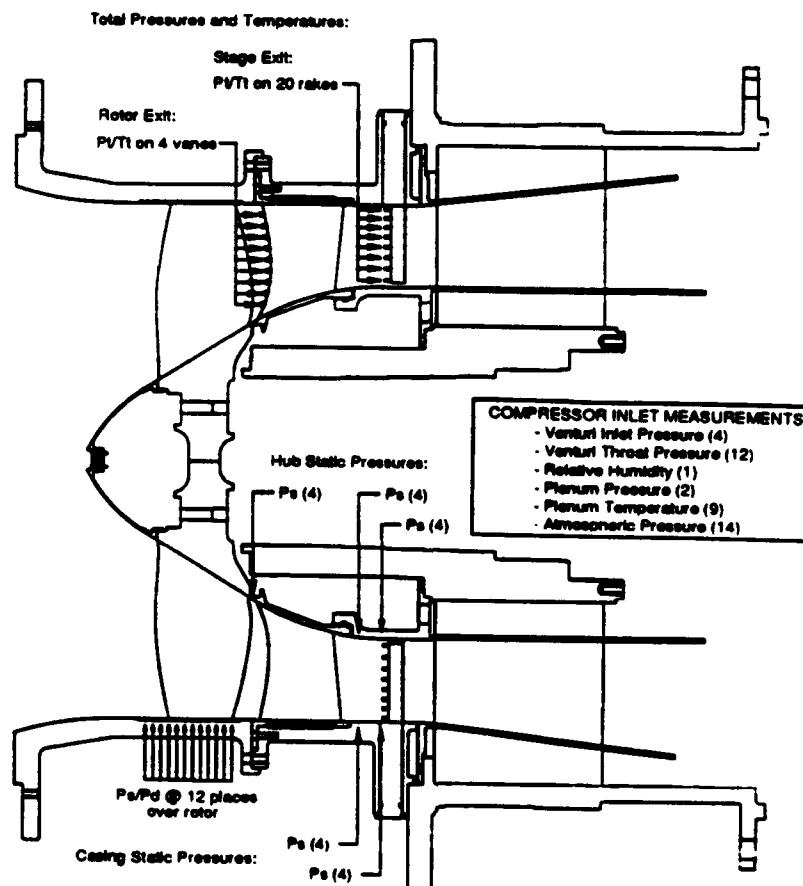


Figure 3.9 Compressor instrumentation

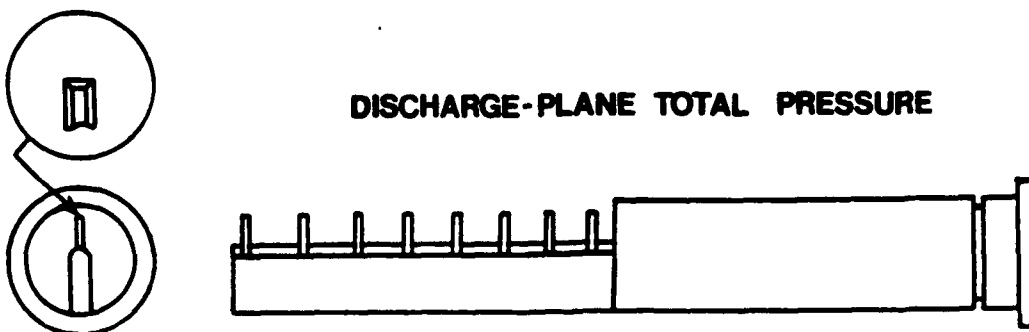
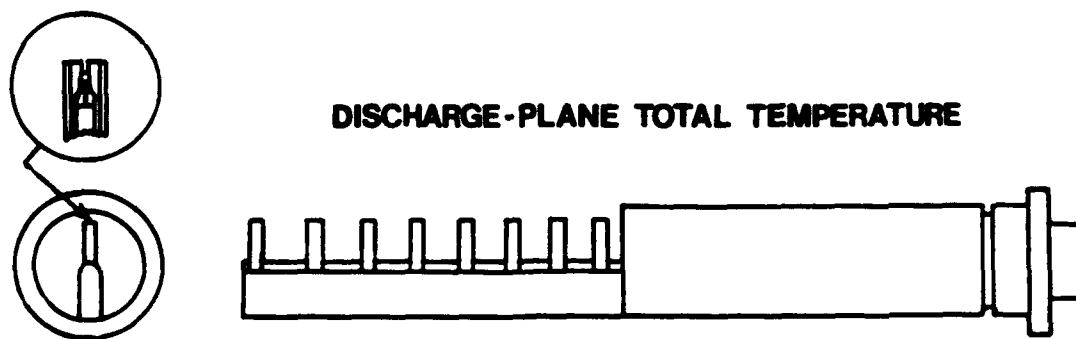
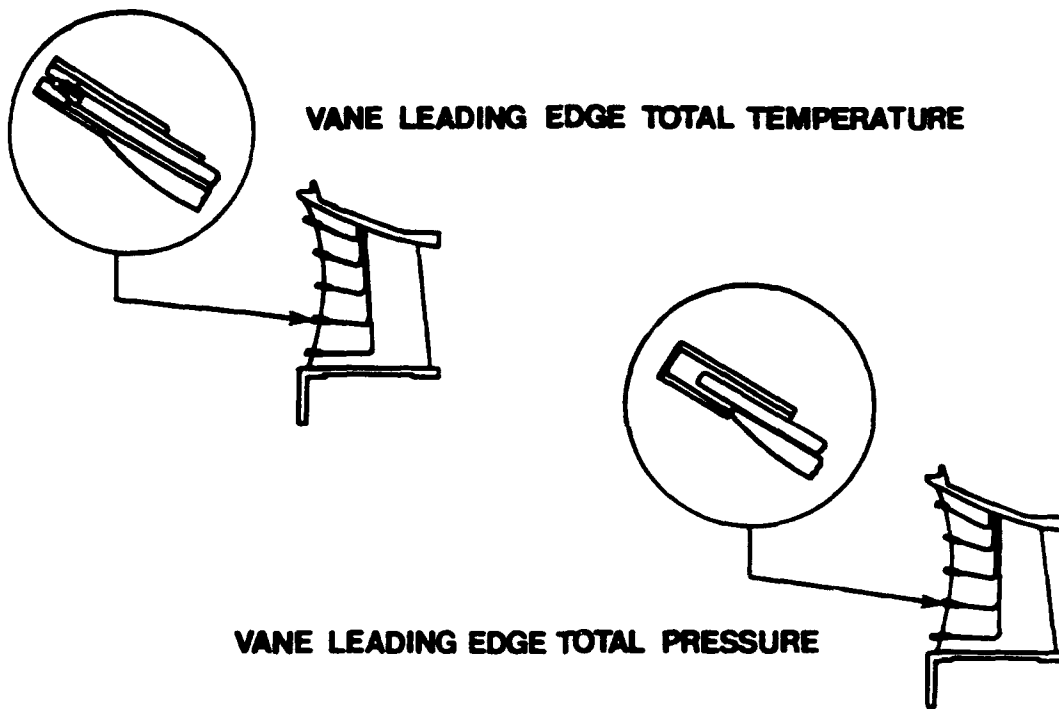


Figure 3.10 Vane leading edge and discharge plane rake instrumentation [29]

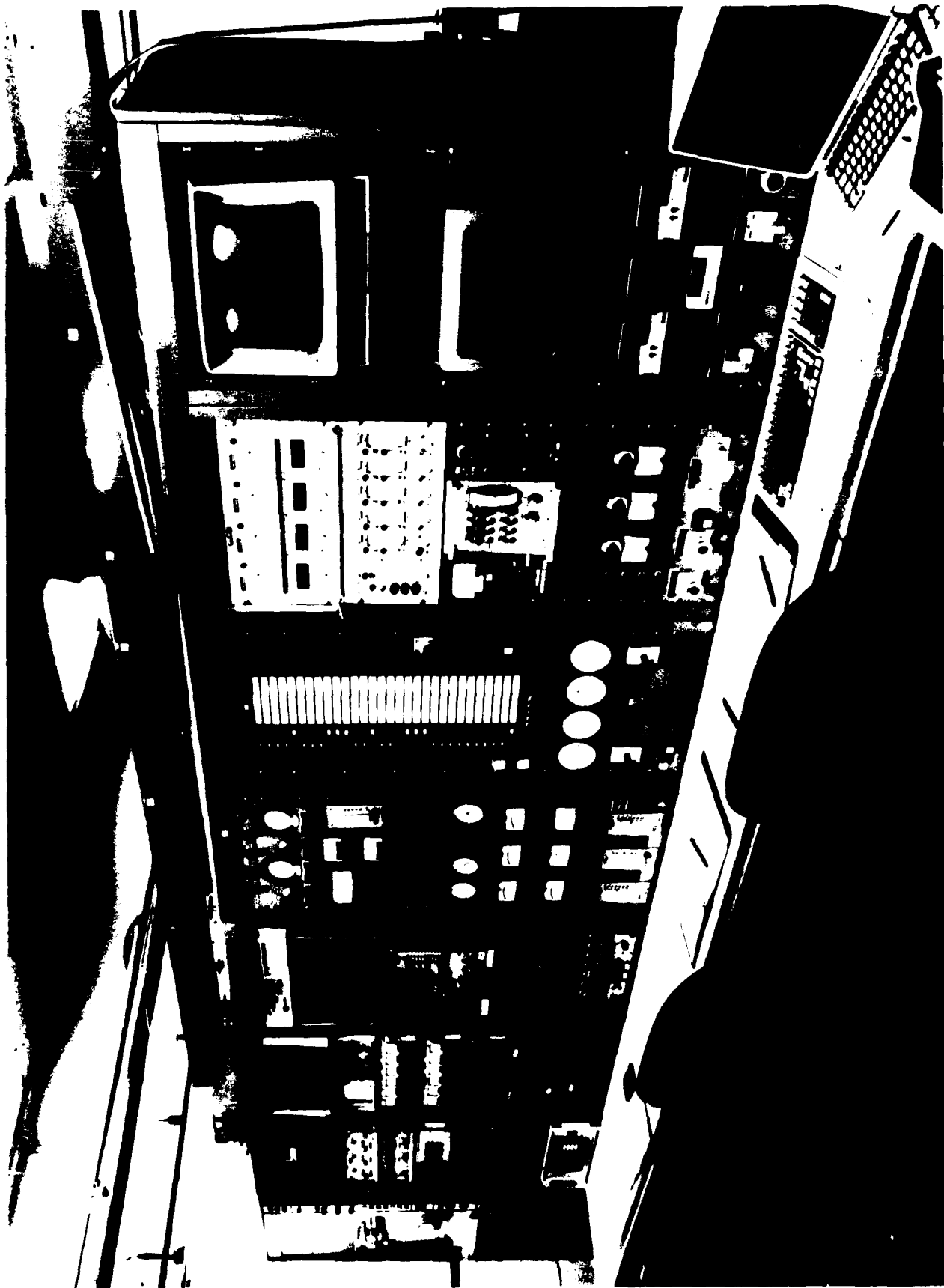


Figure 3.11 CARL control room

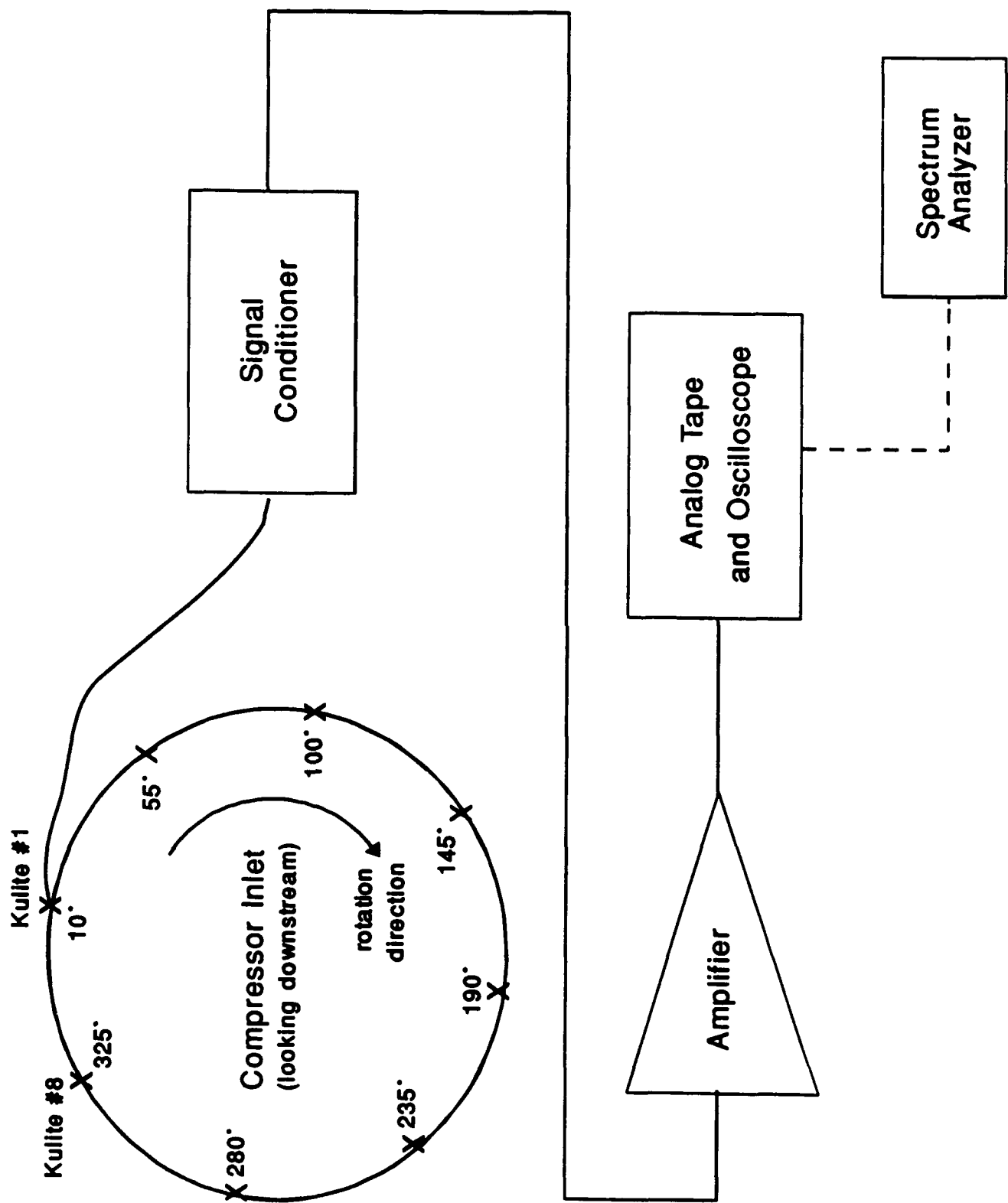


Figure 3.12 Kulite location and signal path

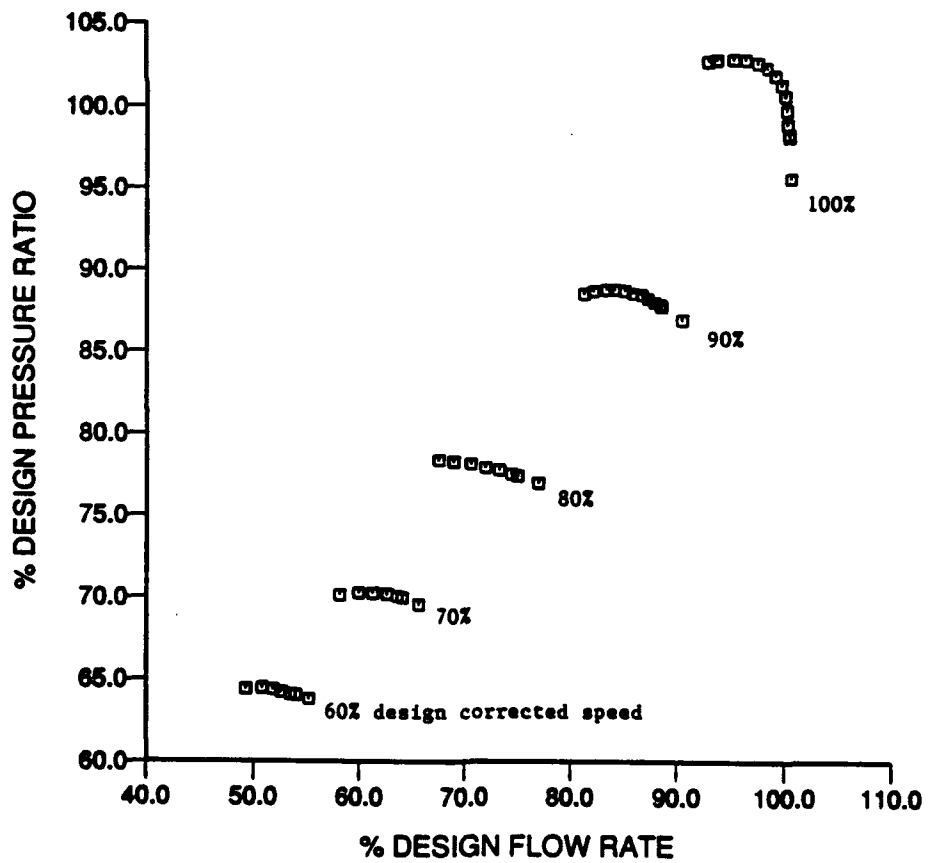
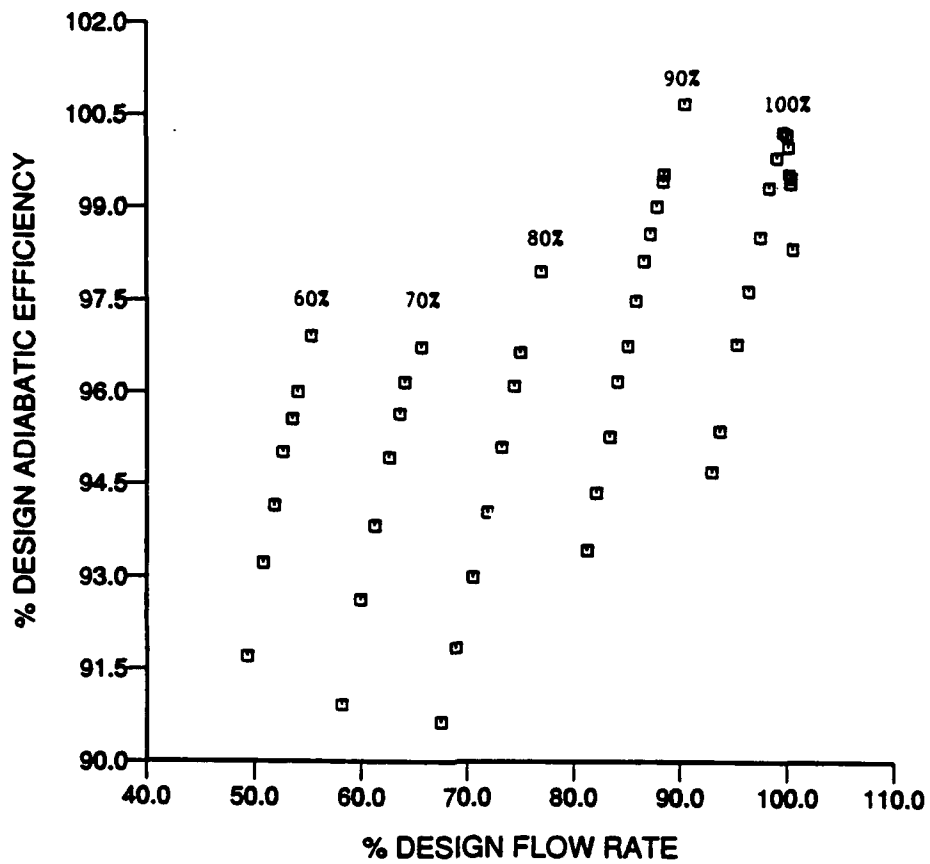


Figure 4.1 Steady-state map of Rotor 4

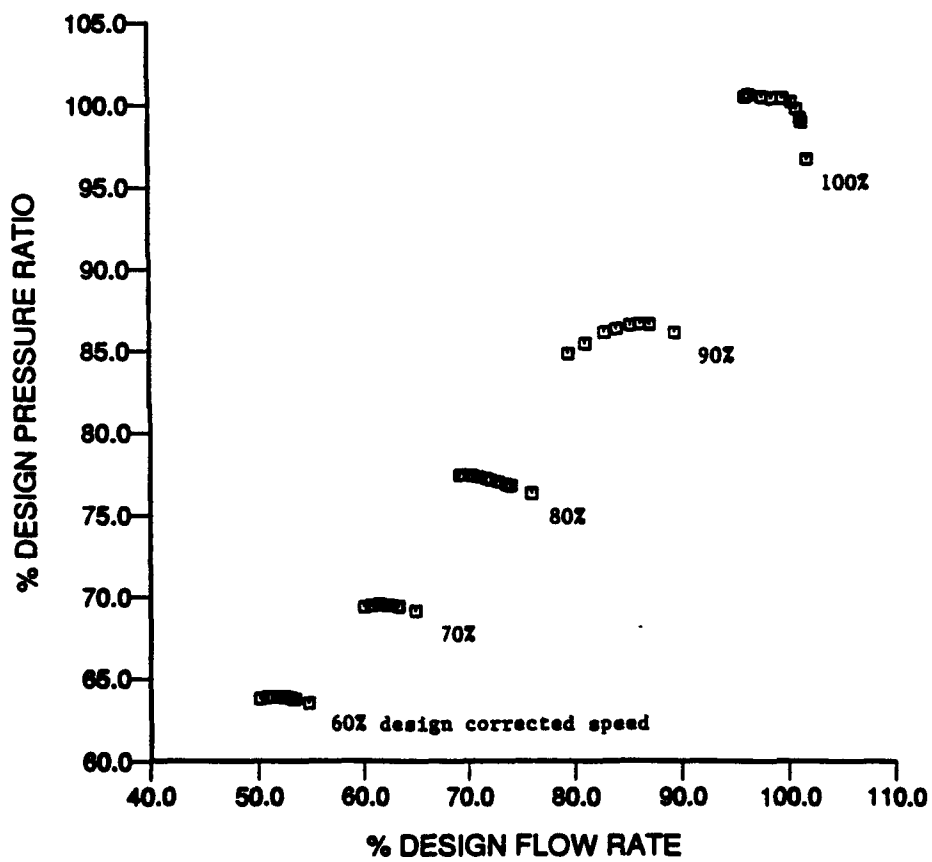
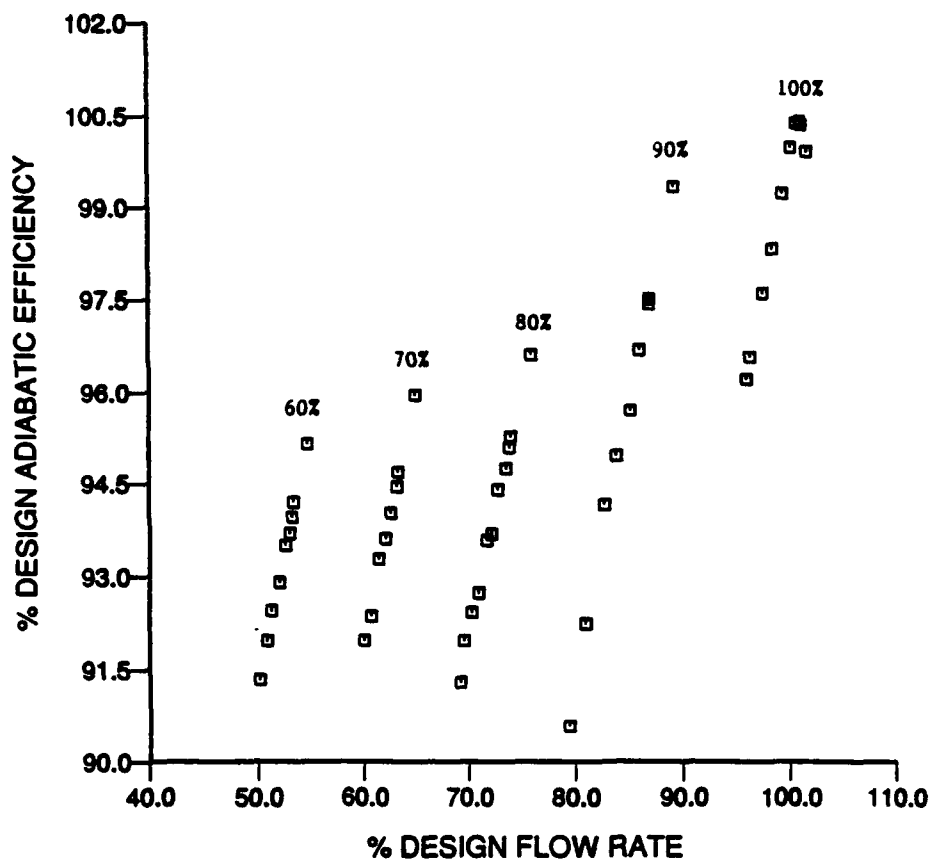


Figure 4.2 Steady-state map of Rotor 6

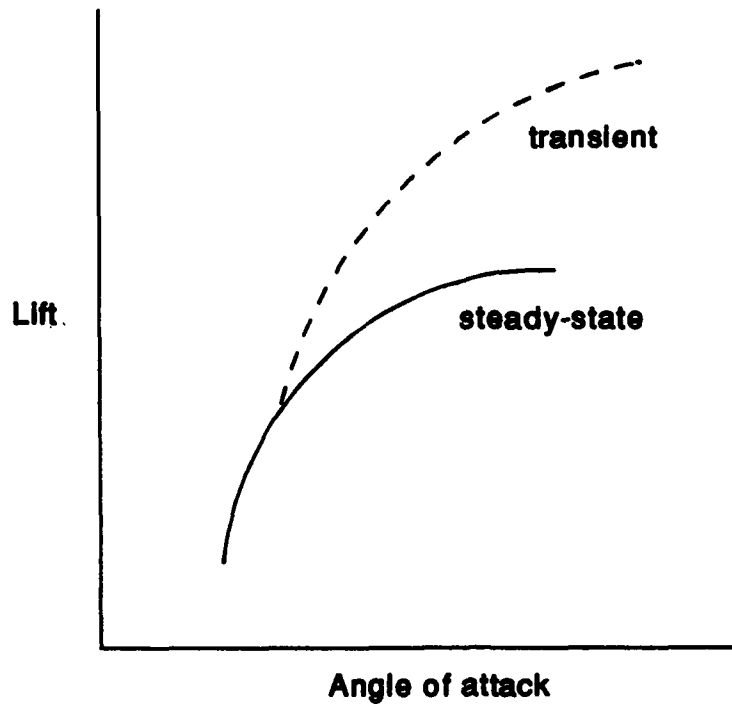


Figure 4.3a Transient behavior of an isolated airfoil

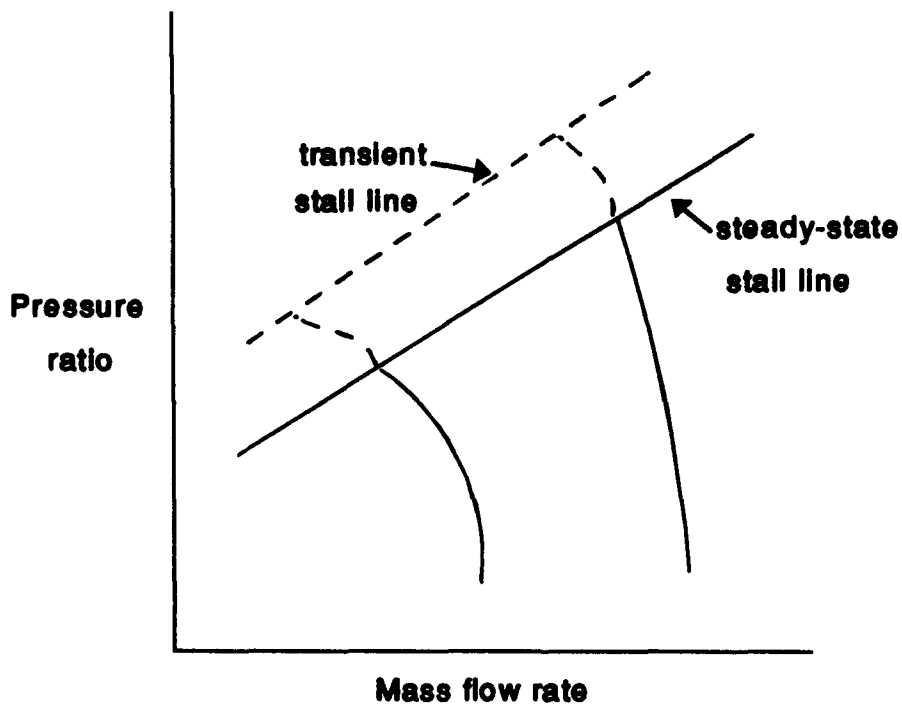


Figure 4.3b Transient behavior of a compressor stage

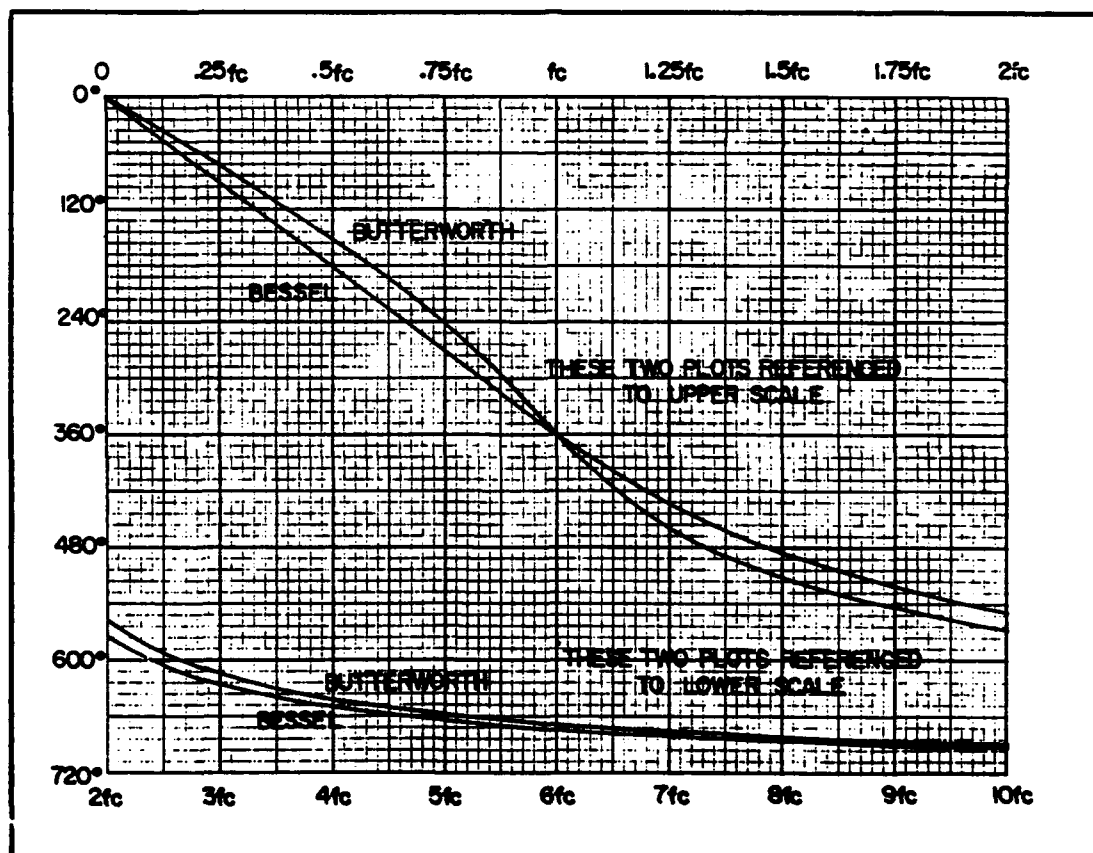
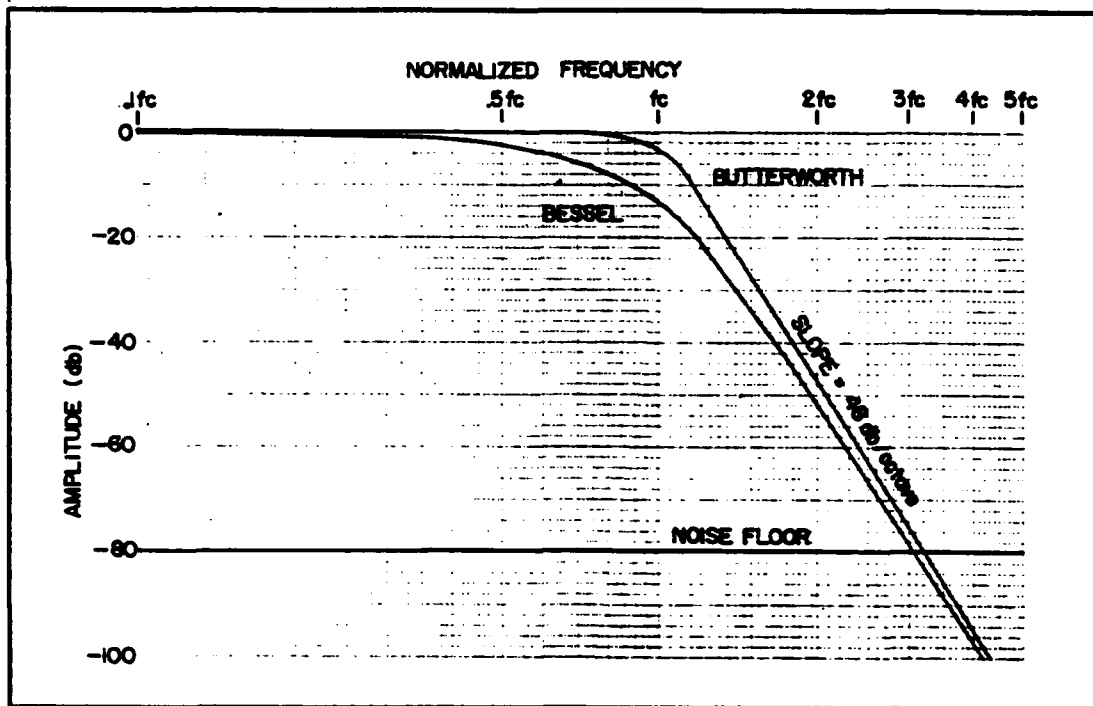


Figure 4.4 Characteristics of Butterworth analog filter

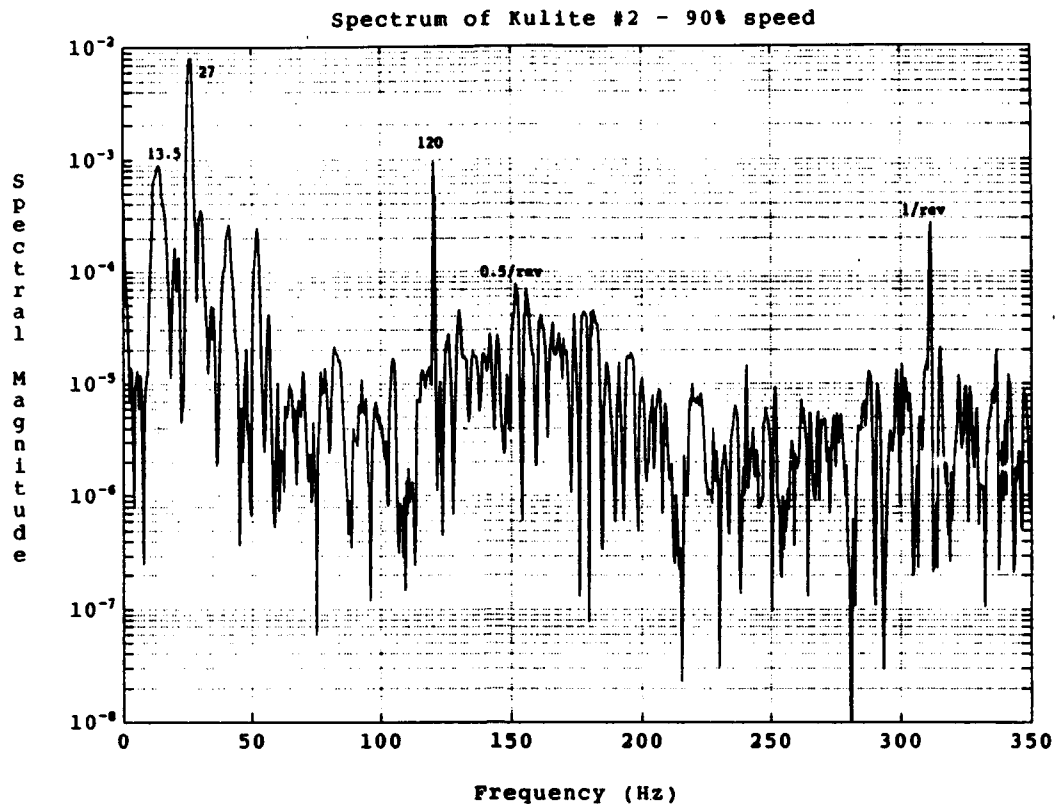


Figure 4.5 Spectrum from Kulite #2 - no additional filtering

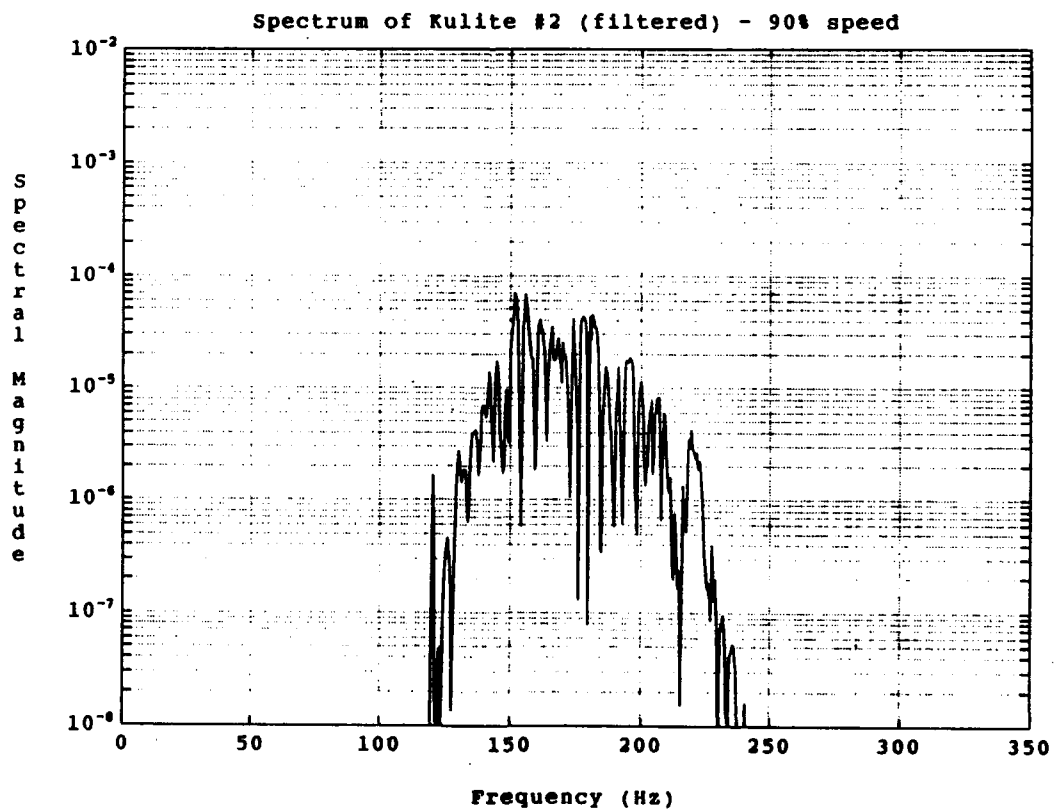
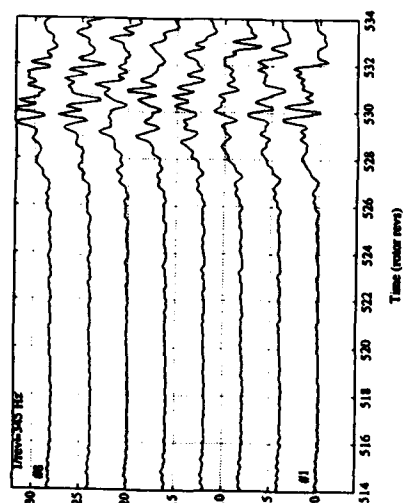


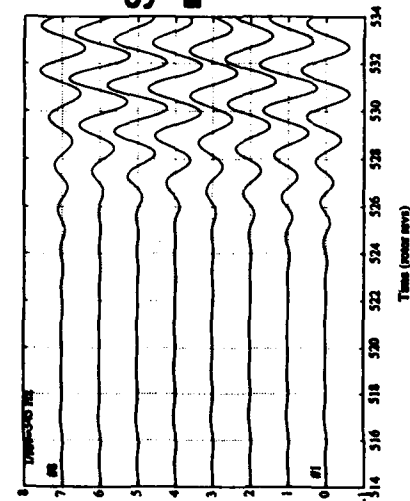
Figure 4.6 Spectrum from Kulite #2 - band-pass filtered



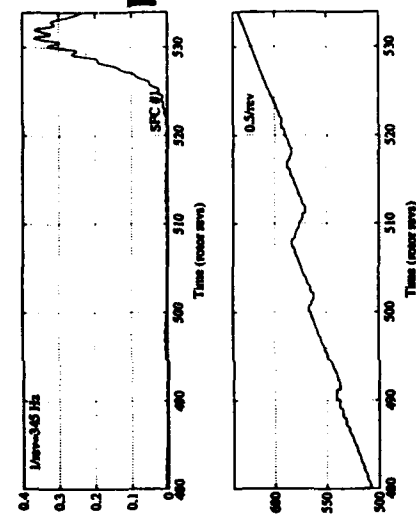
Measured
Kulite
signals (8)
(strong blade passing frequency)

Analog-filtered
pressure traces

Digitally-filtered
pressure traces



Spatial
DFT



Temporal
FFT

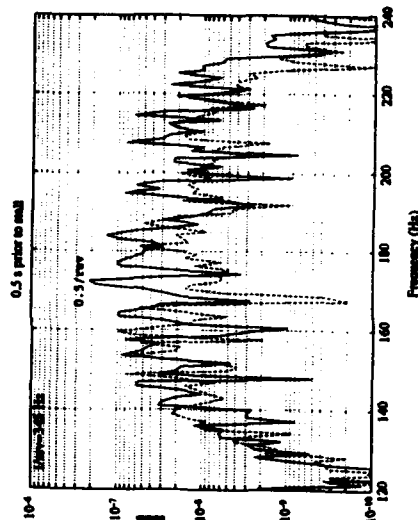


Figure 4.7 Analyses used for stall inception characterization

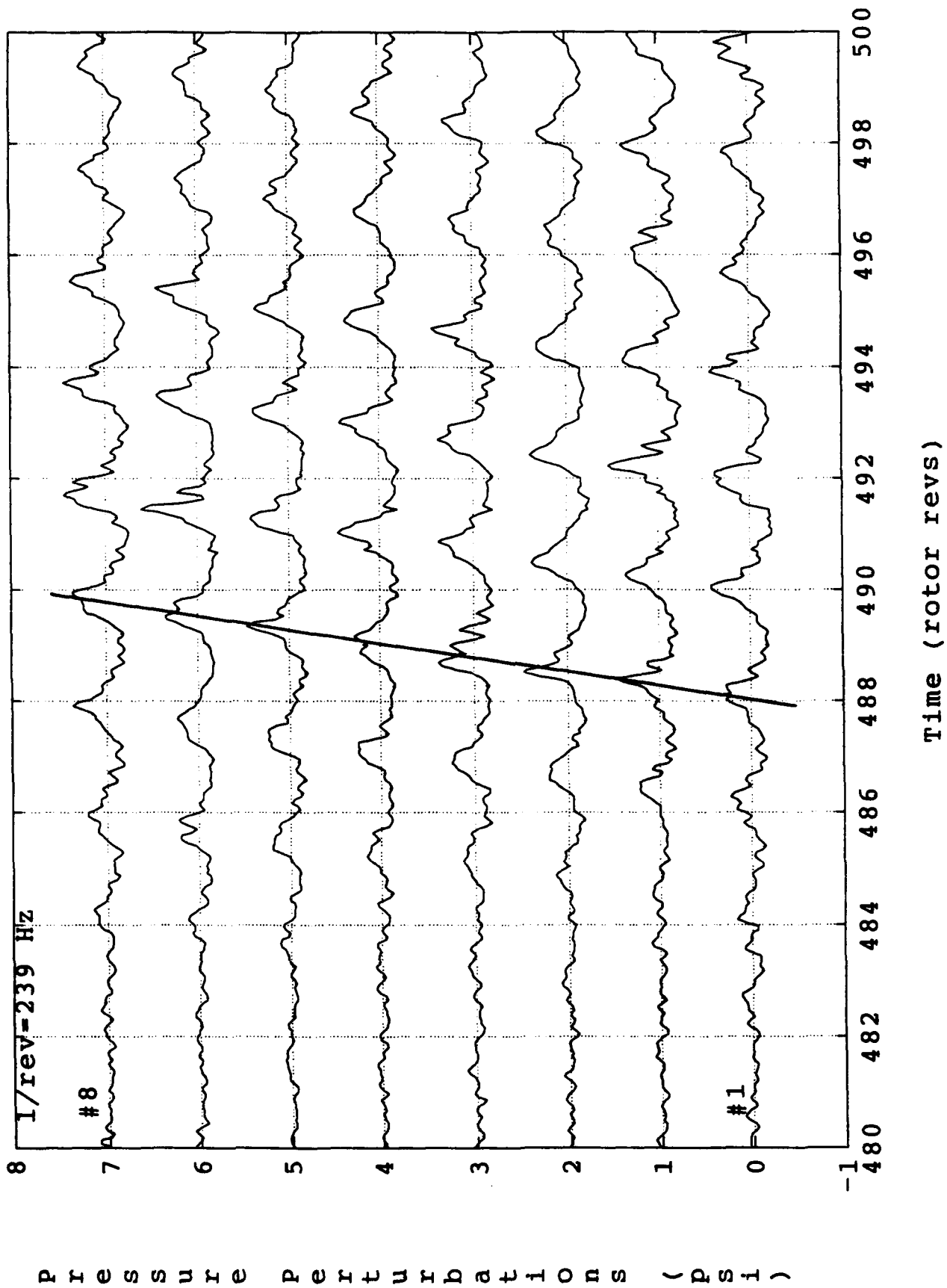
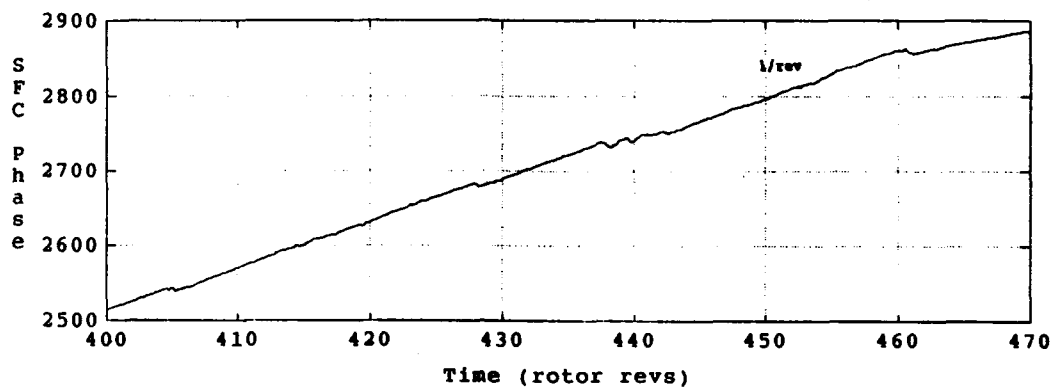
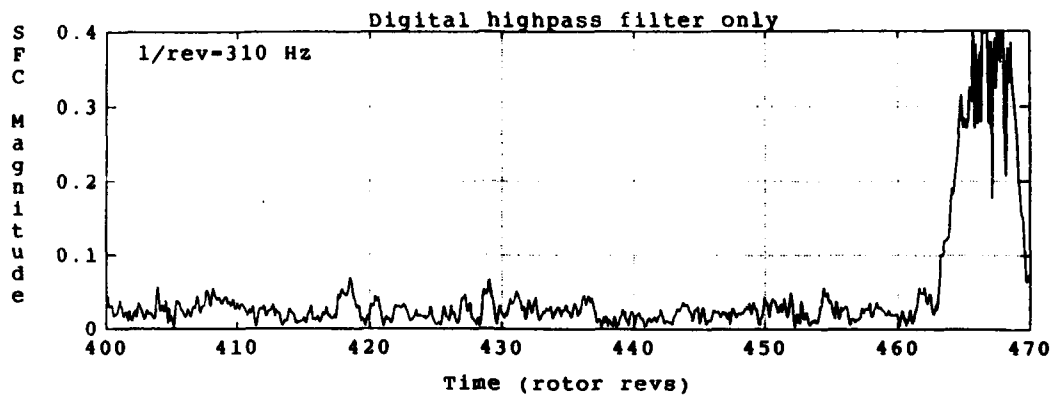
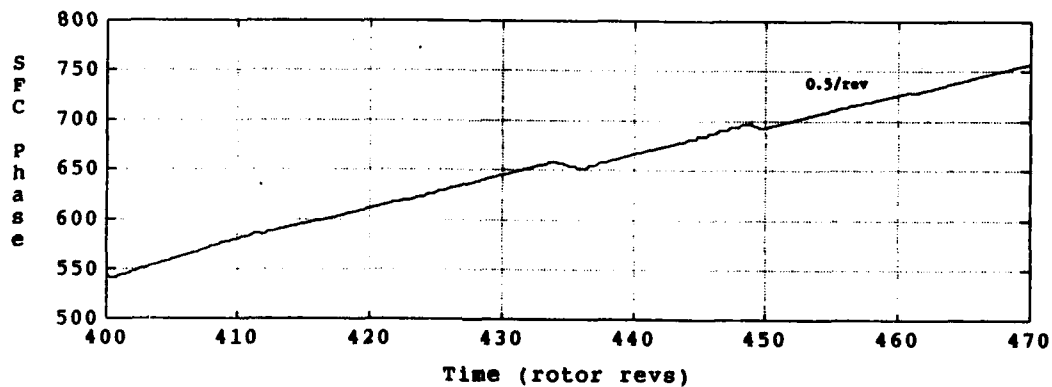
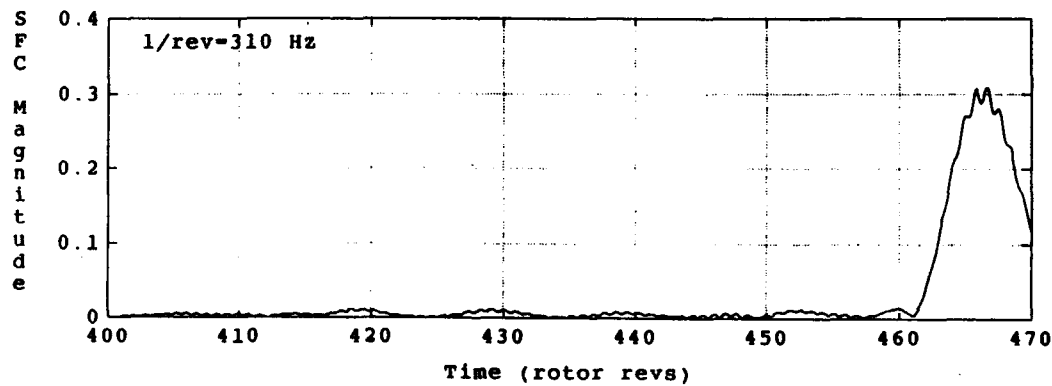


Figure 4.8 Pressure traces showing rotating waves



a. digital highpass filter



b. digital bandpass filter

Figure 4.9 Illustration of SFC #1 analysis - 90% speed transient

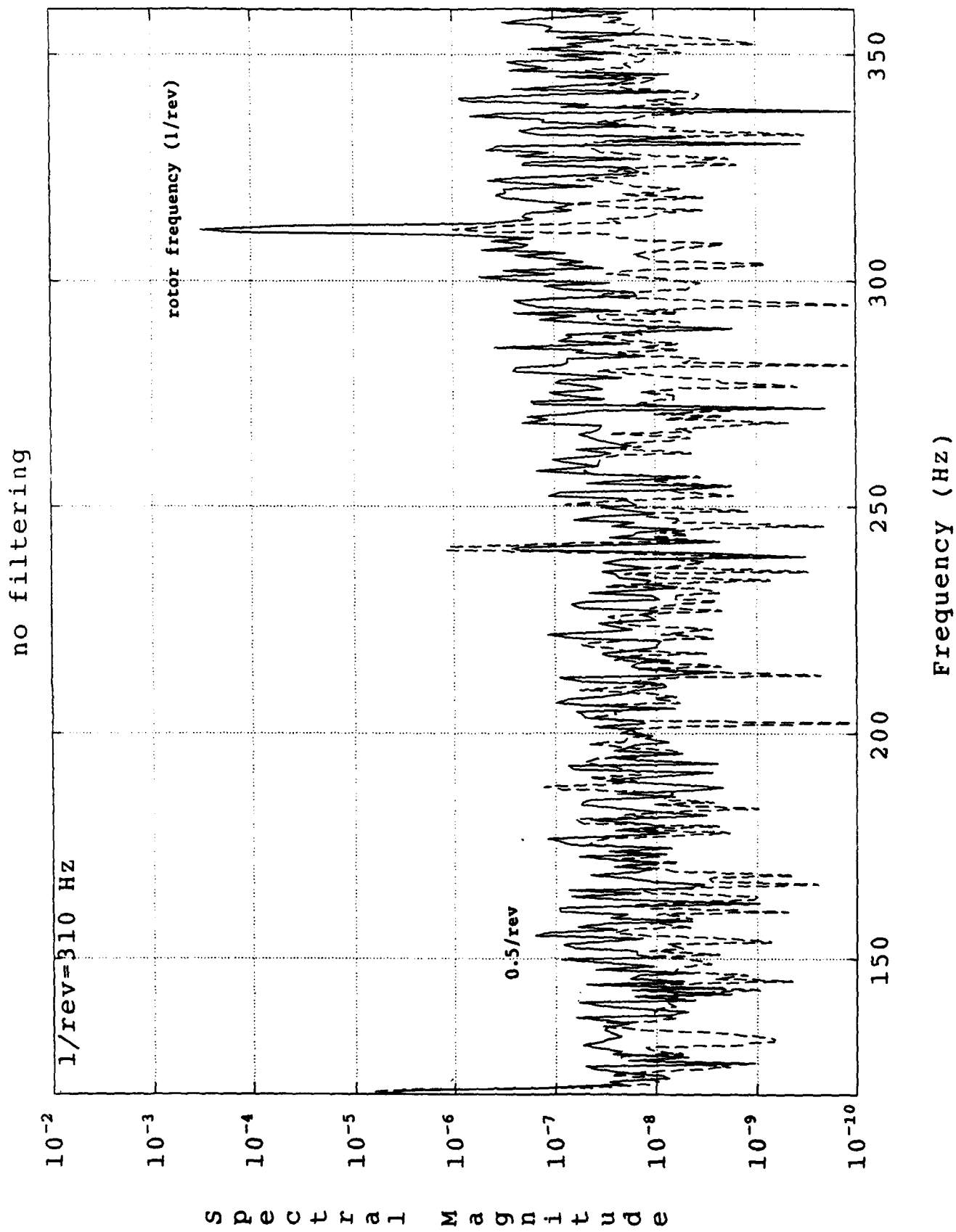


Figure 4.10 PSD of an SFC - 90% speed transient

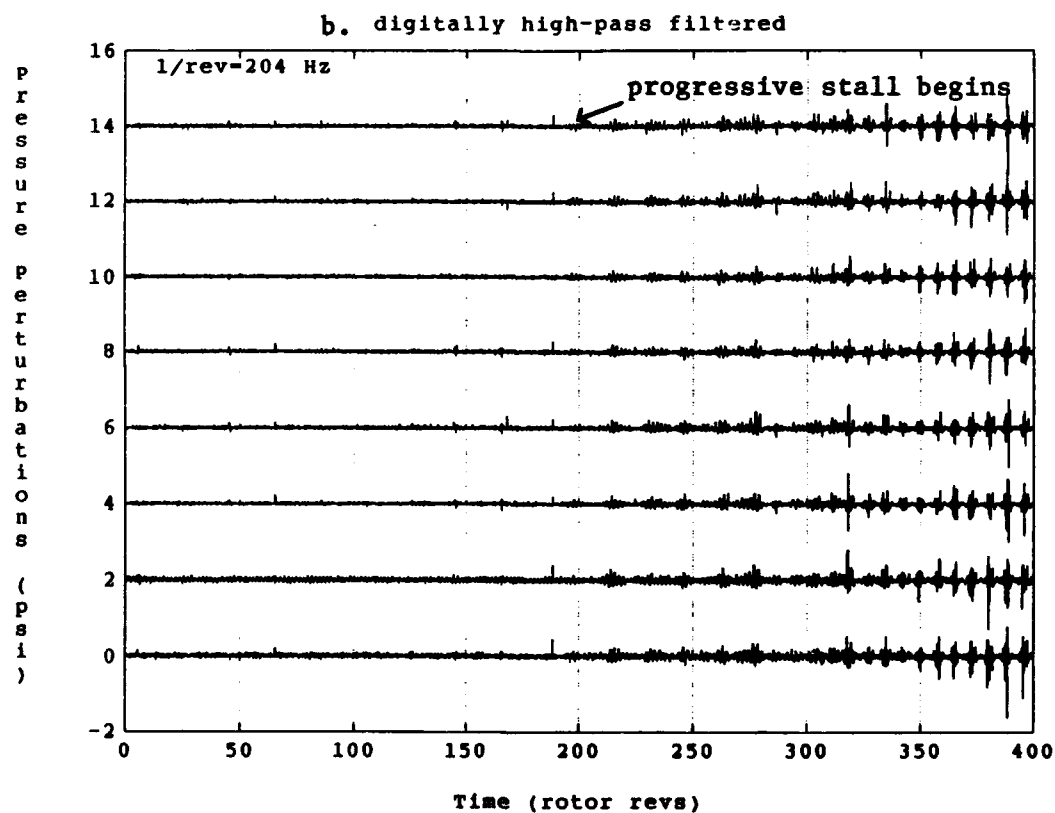
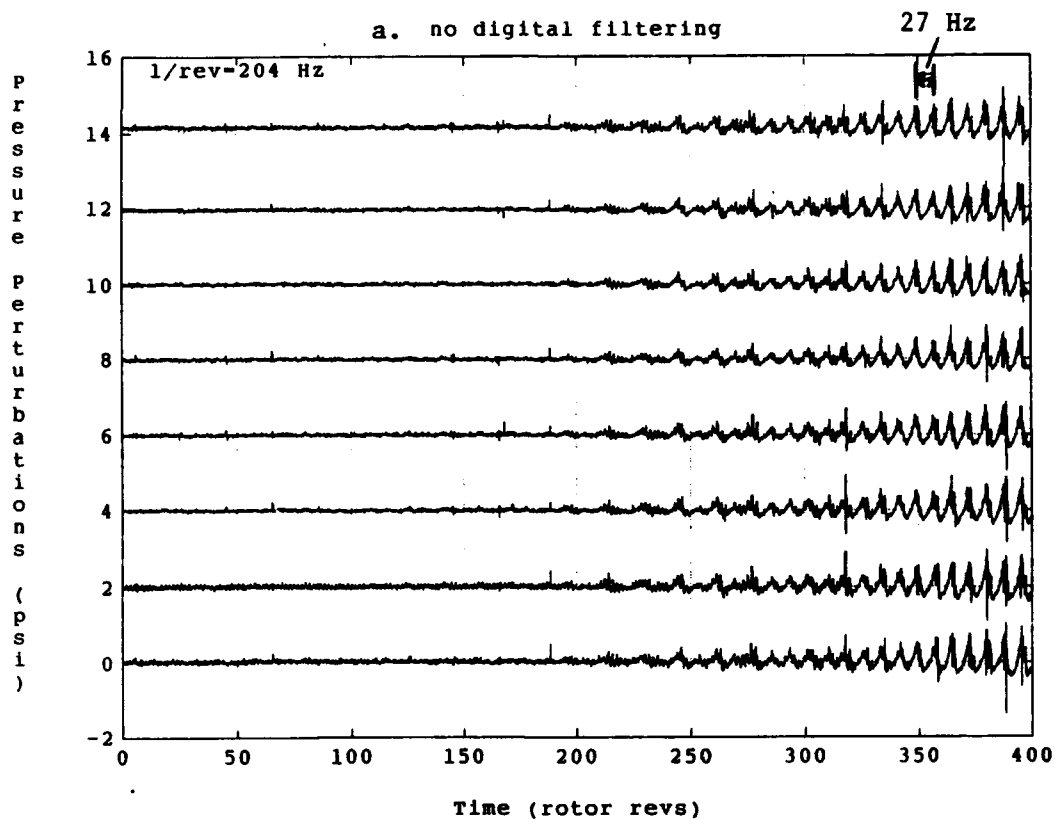
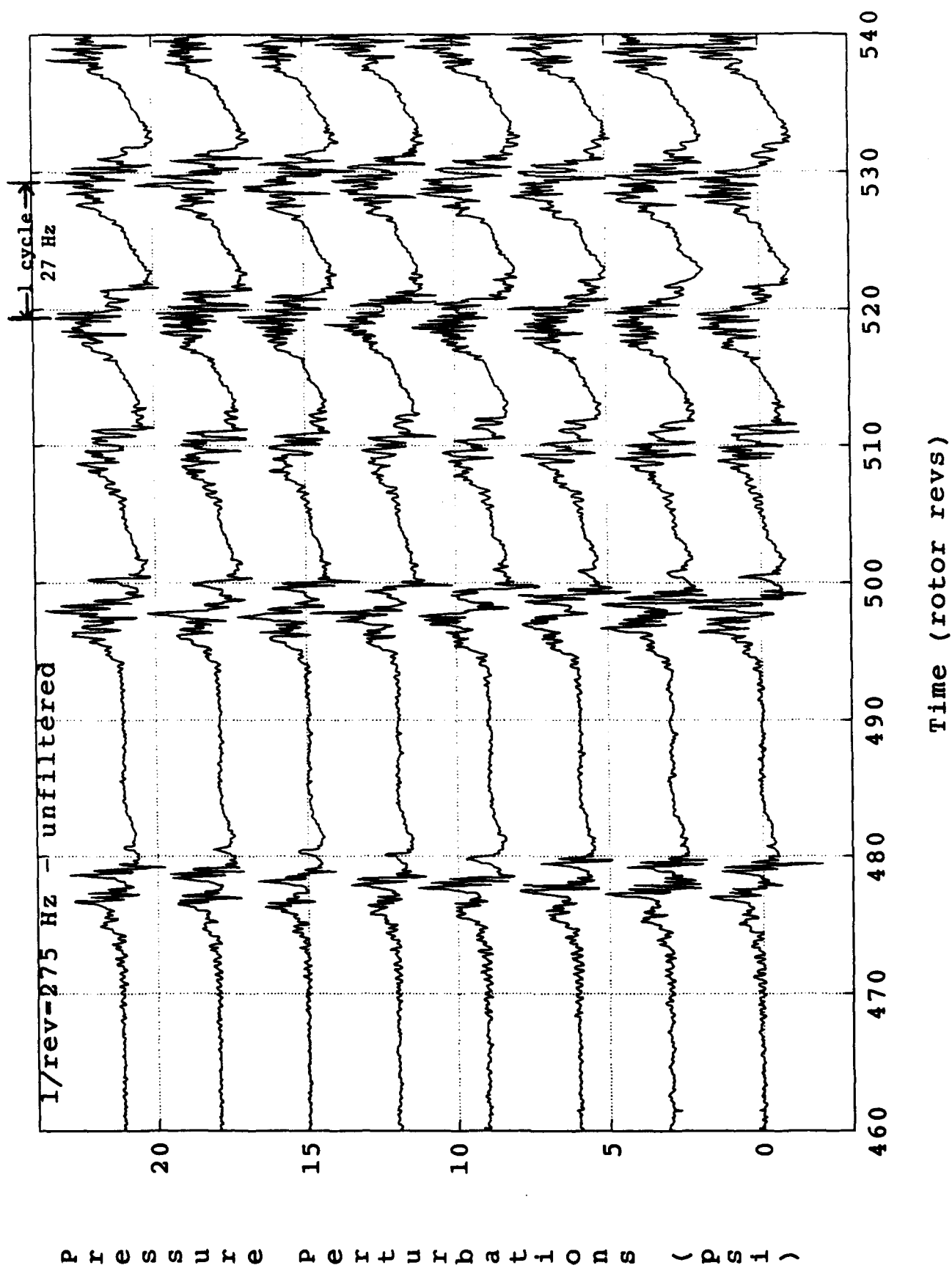


Figure 5.1 Low frequency planar oscillations - 60% speed, Rotor 4



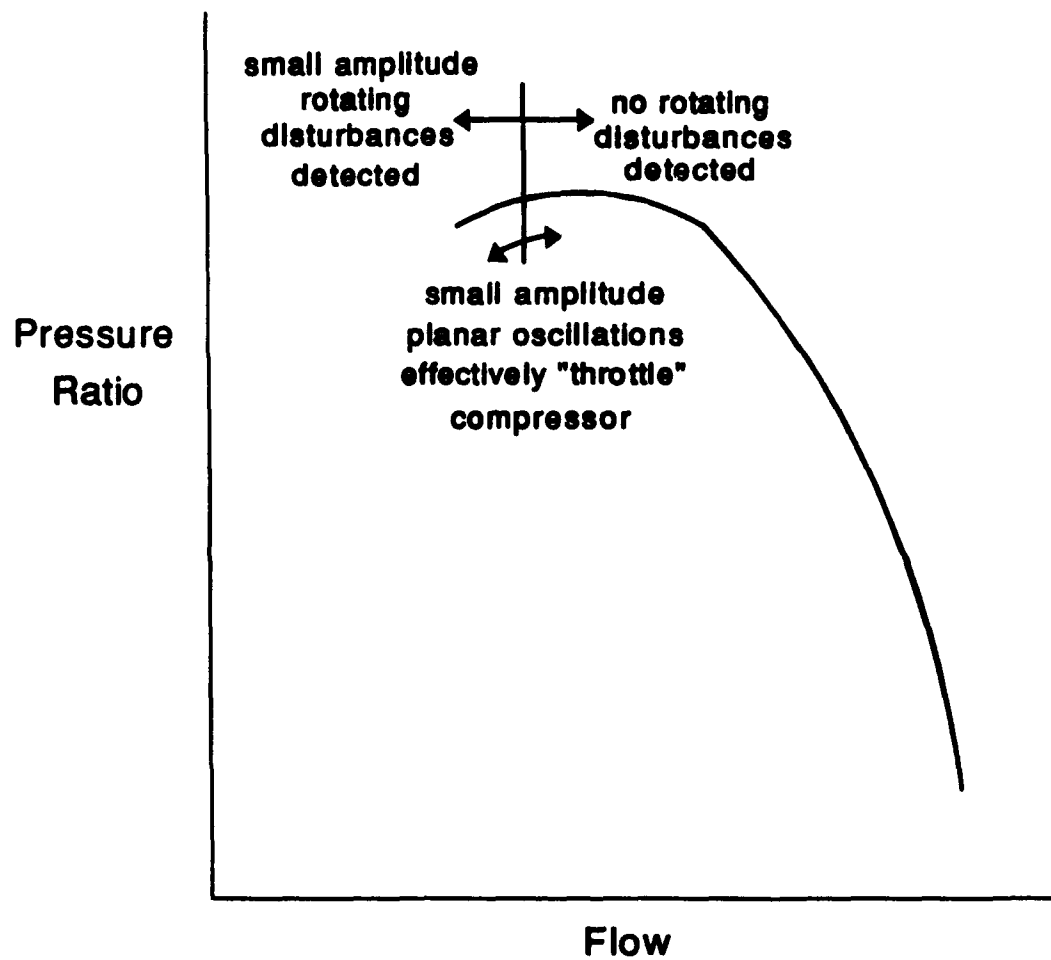


Figure 5.3 Hypothetical behavior of compressor during transient to stall with planar oscillations

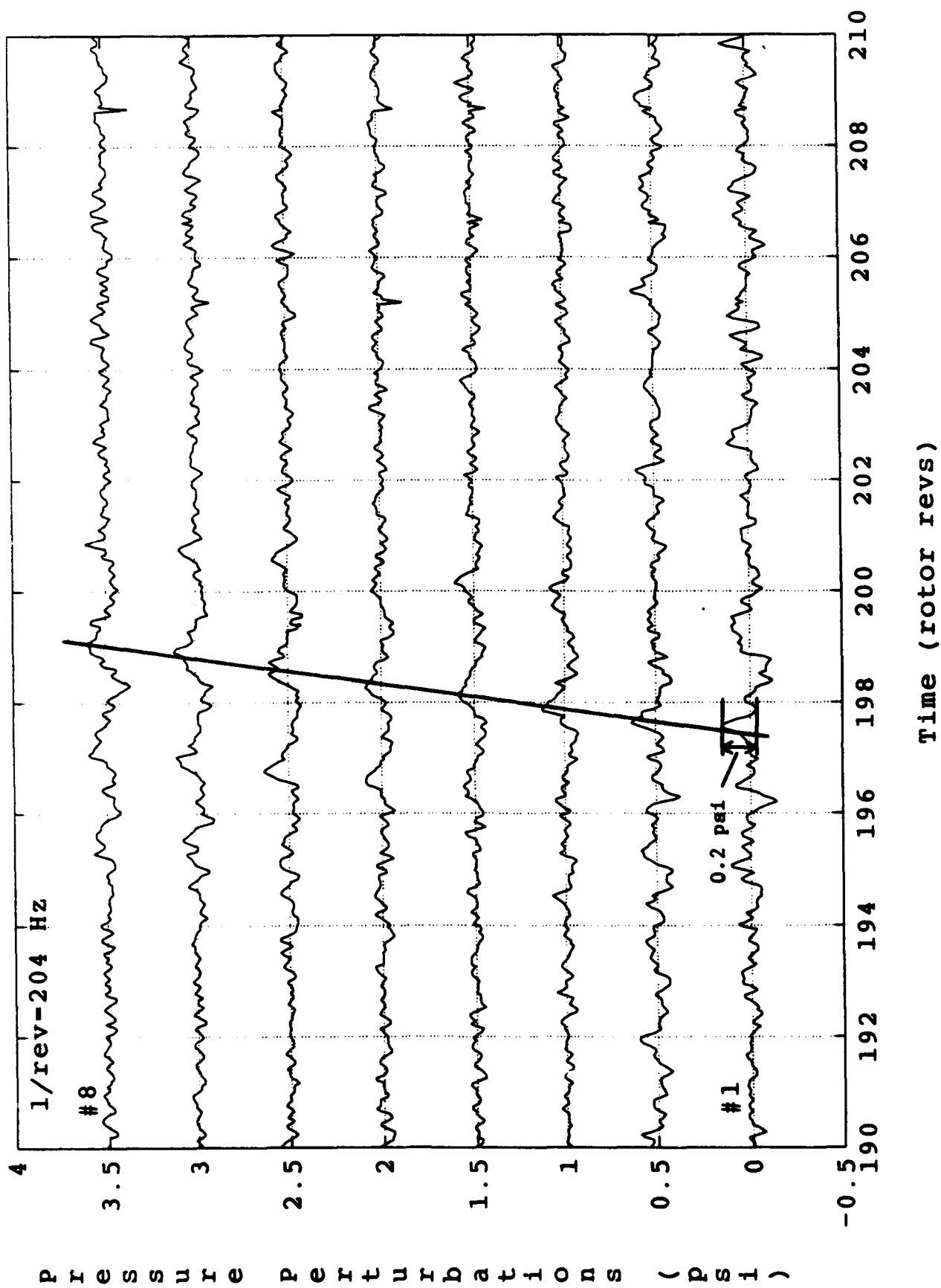


Figure 5.4 Pressure traces (no additional filtering) -
60% speed transient, Rotor 4

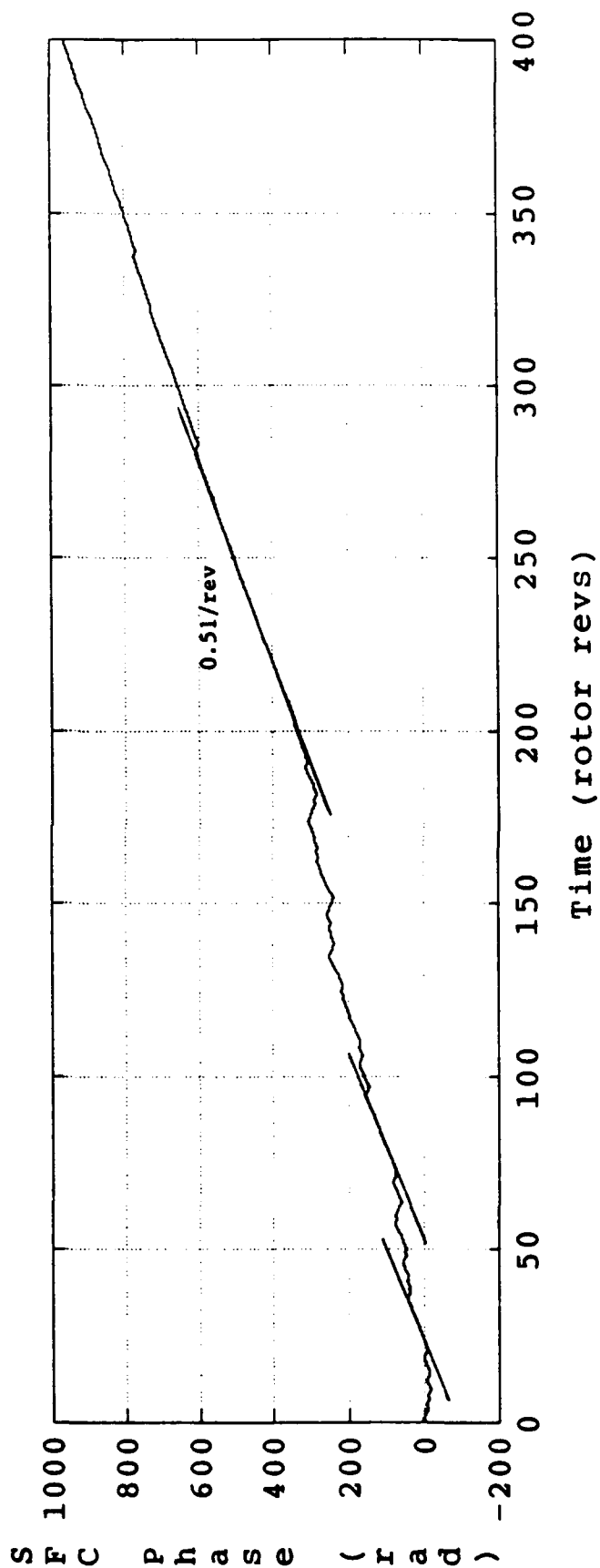
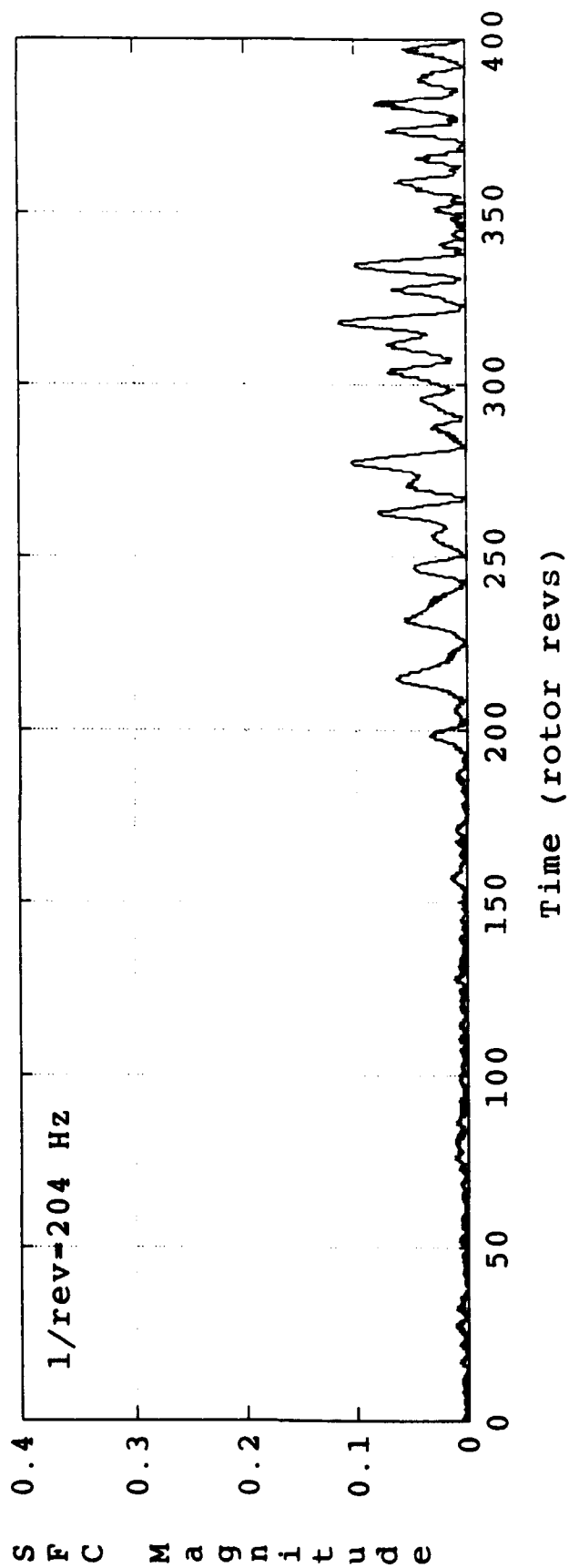


Figure 5.5 Amplitude and phase of SFC #1 - 60% speed, Rotor 4

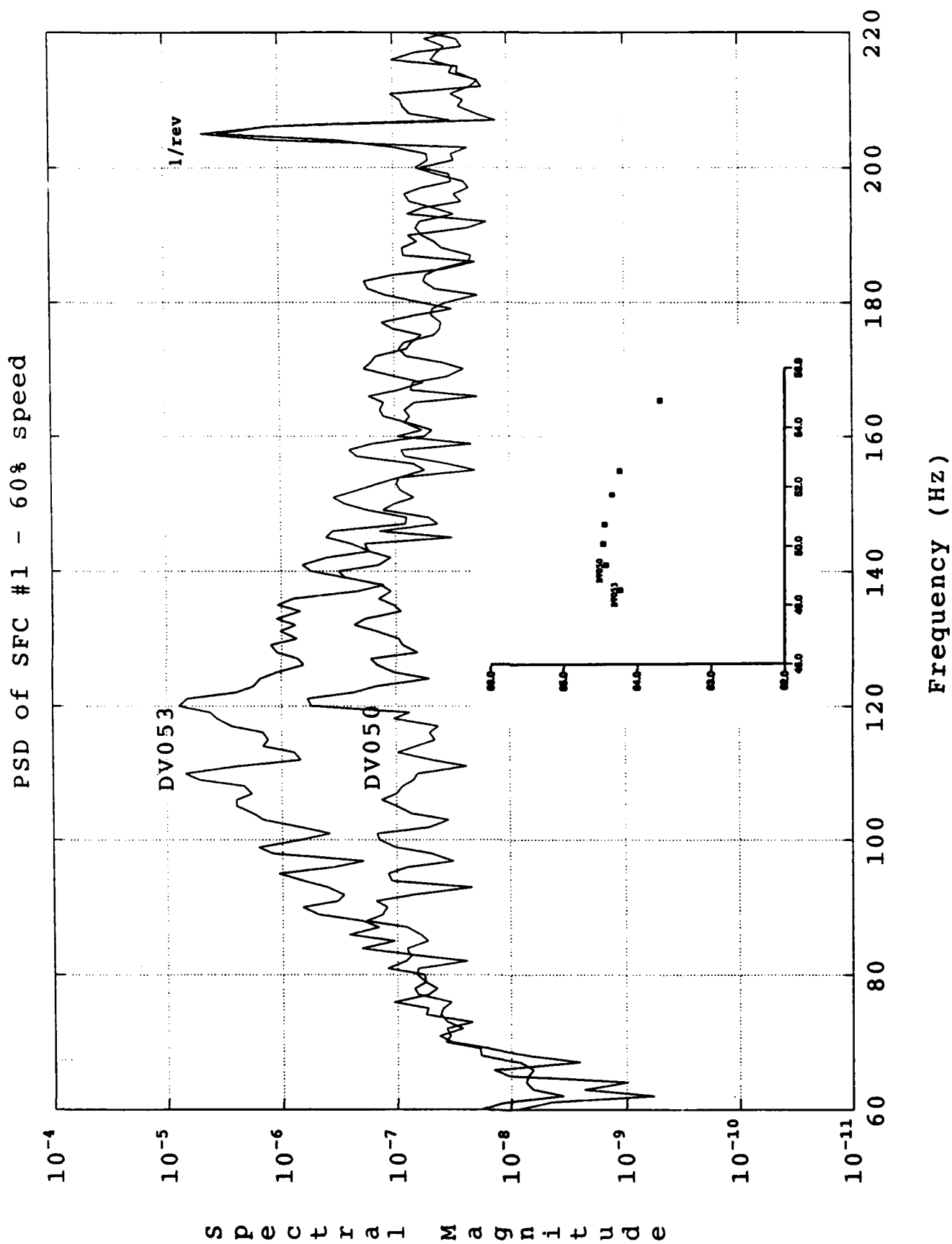
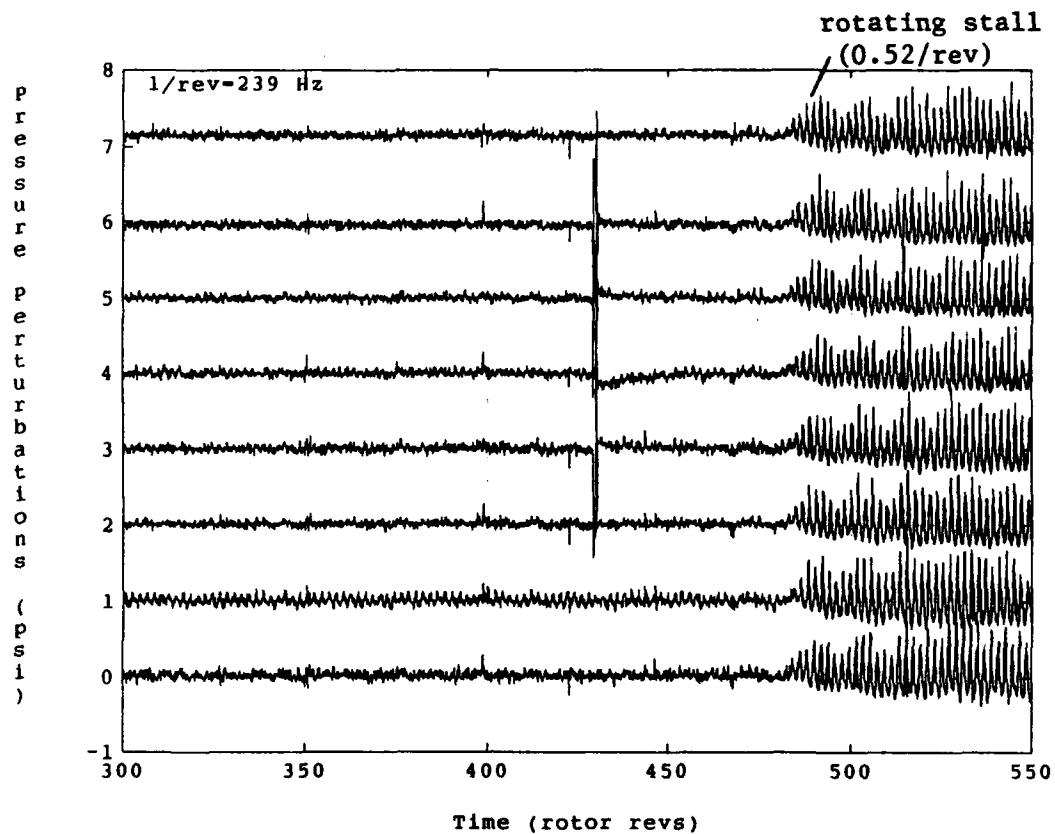
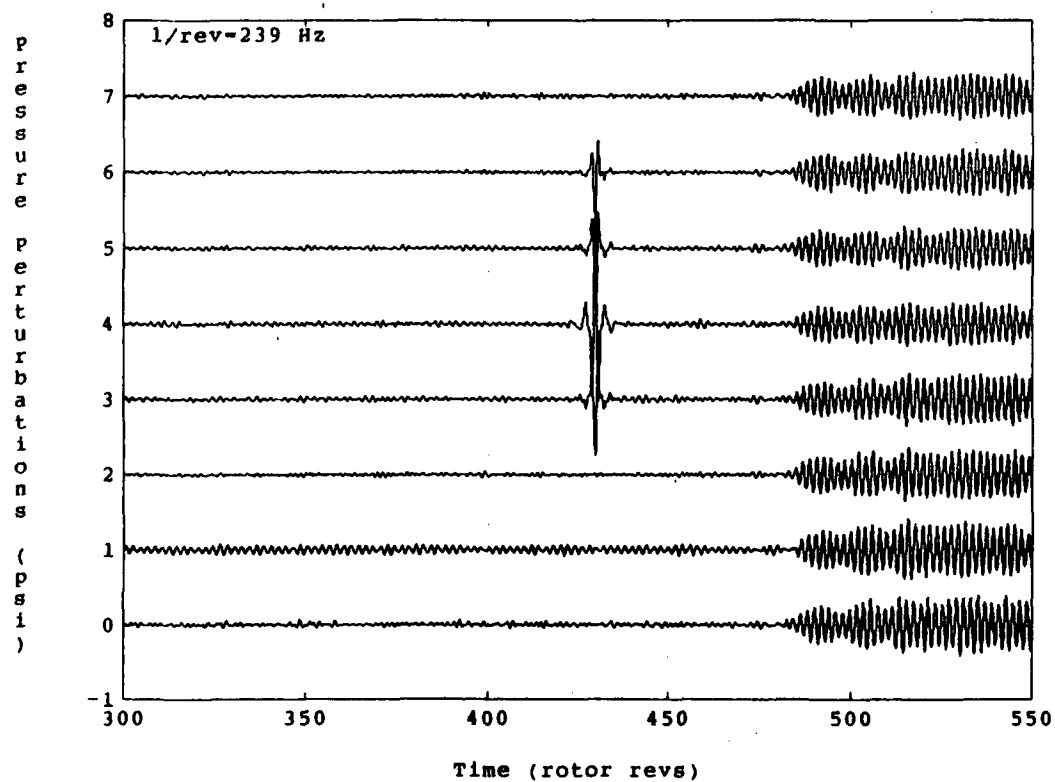


Figure 5.6 Comparison of PSD of SFC #1 at two steady throttle positions - 60% speed, Rotor 4



a. no additional filtering



b. bandpass filtered

Figure 5.7 Pressure traces during 70% speed transient, Rotor 4

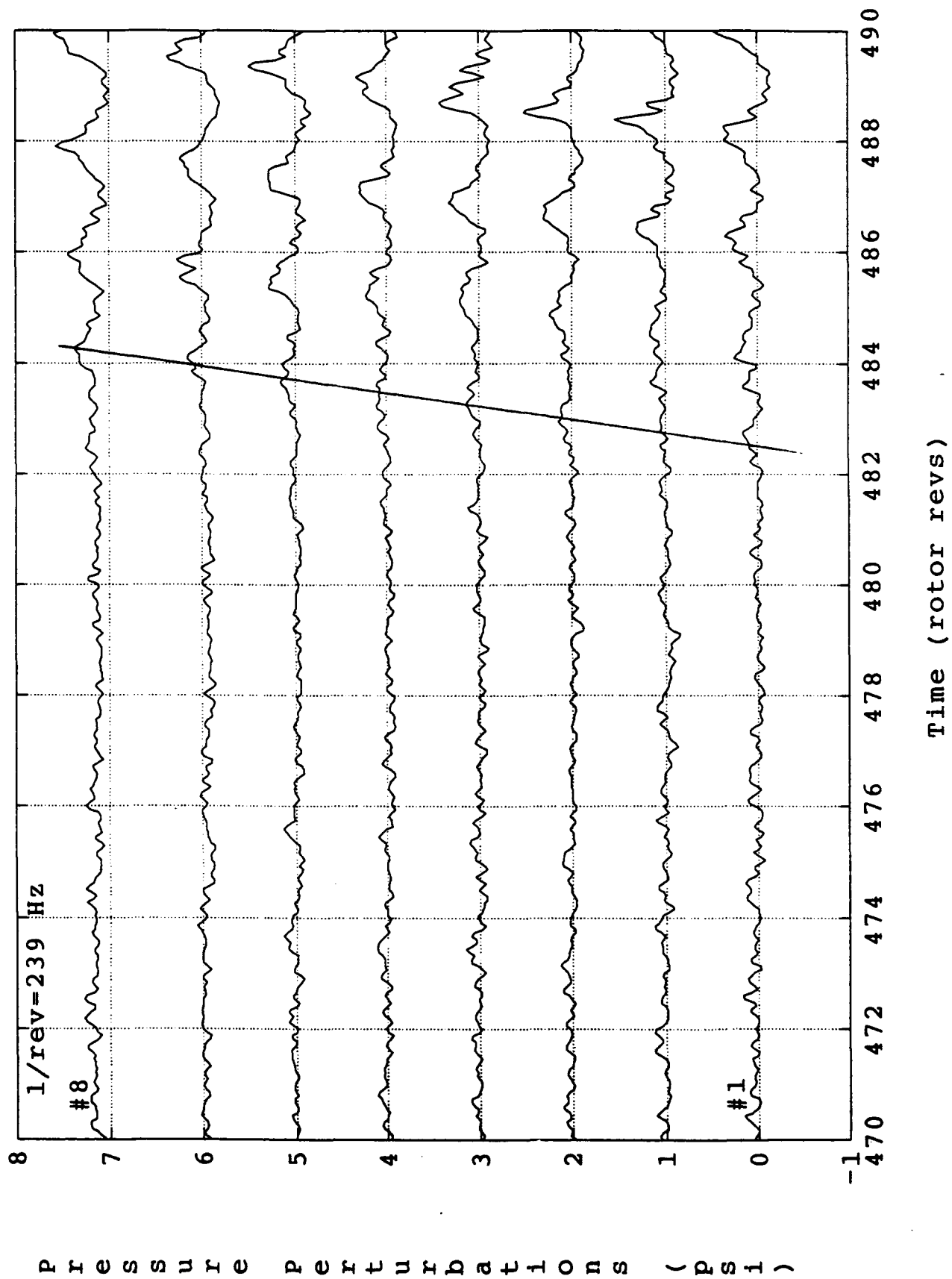


Figure 5.8 Stall inception at 70% speed, Rotor 4

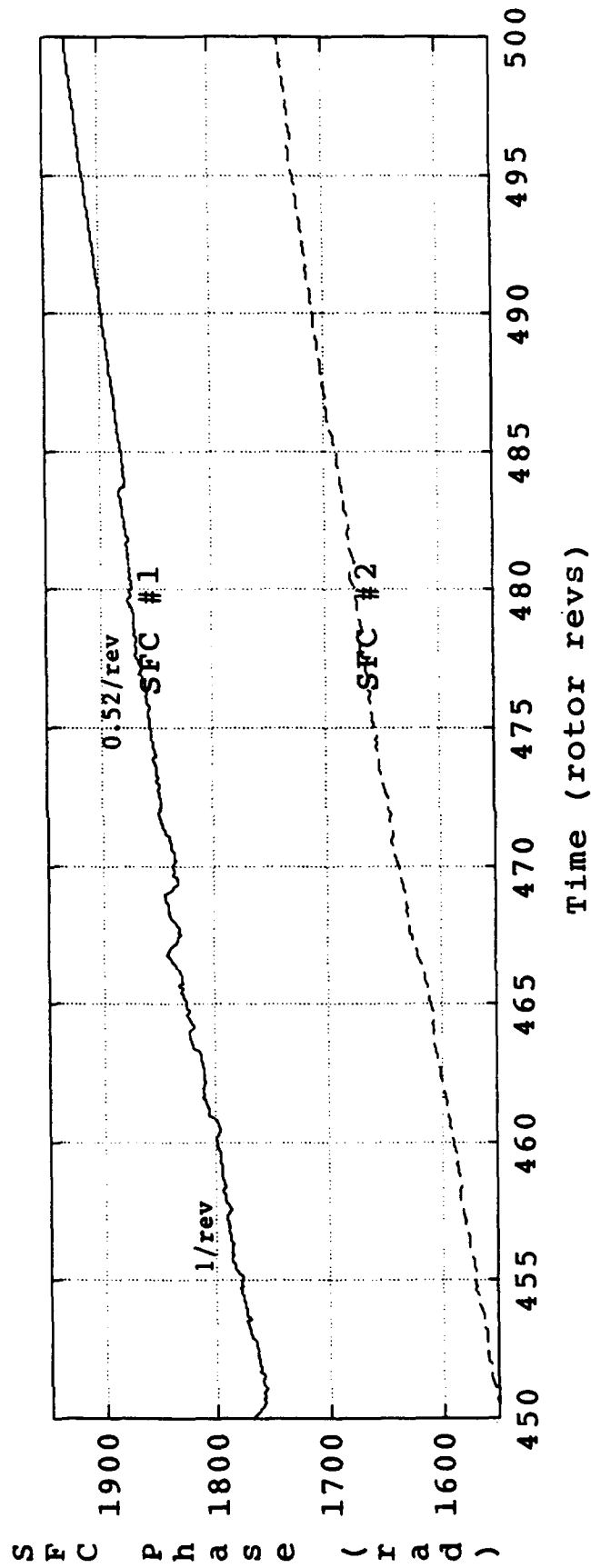
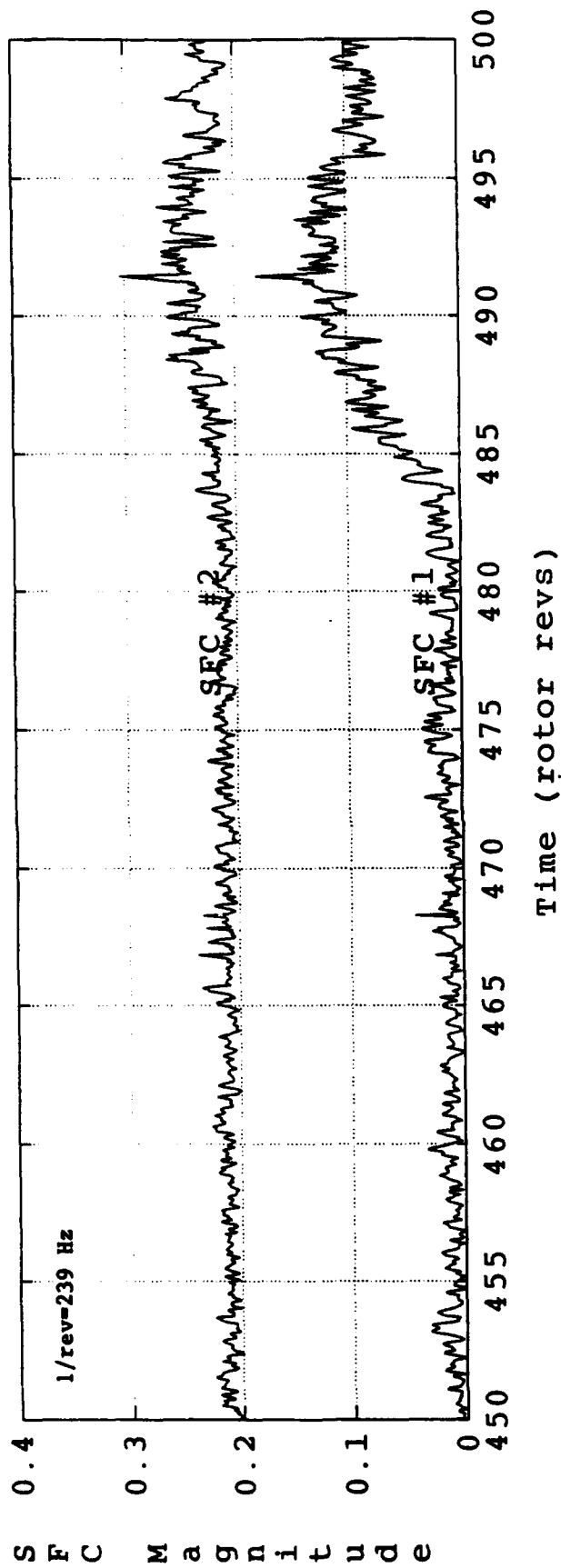
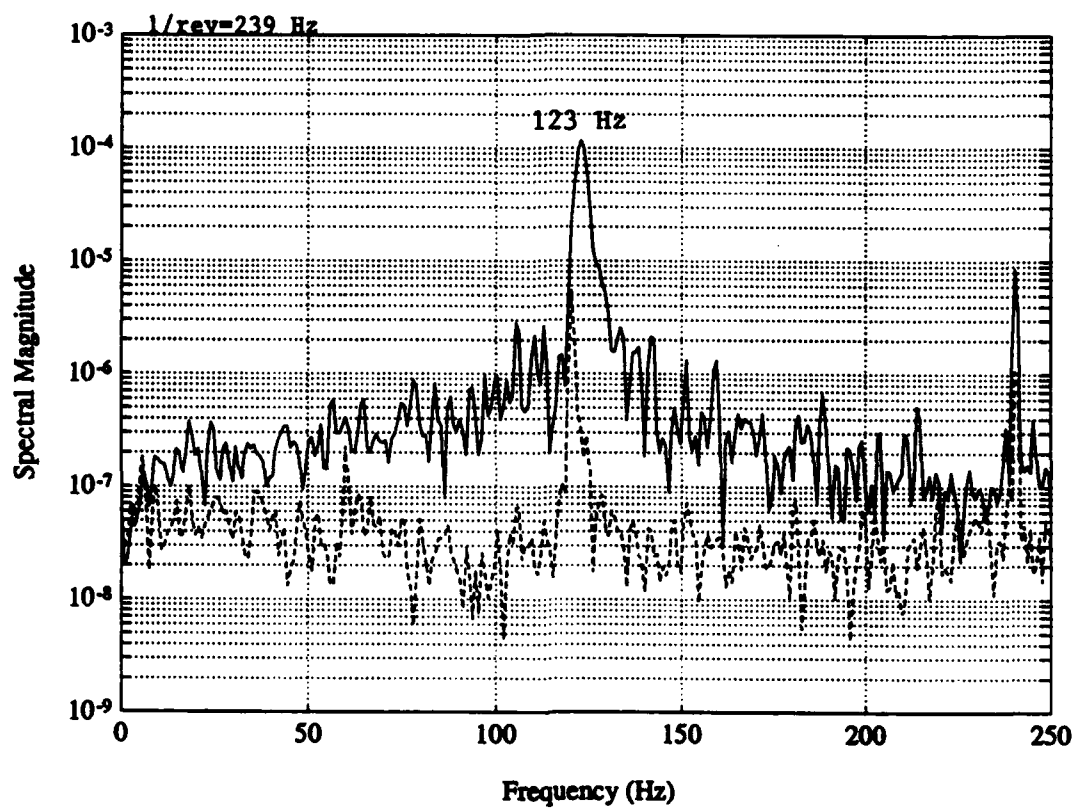
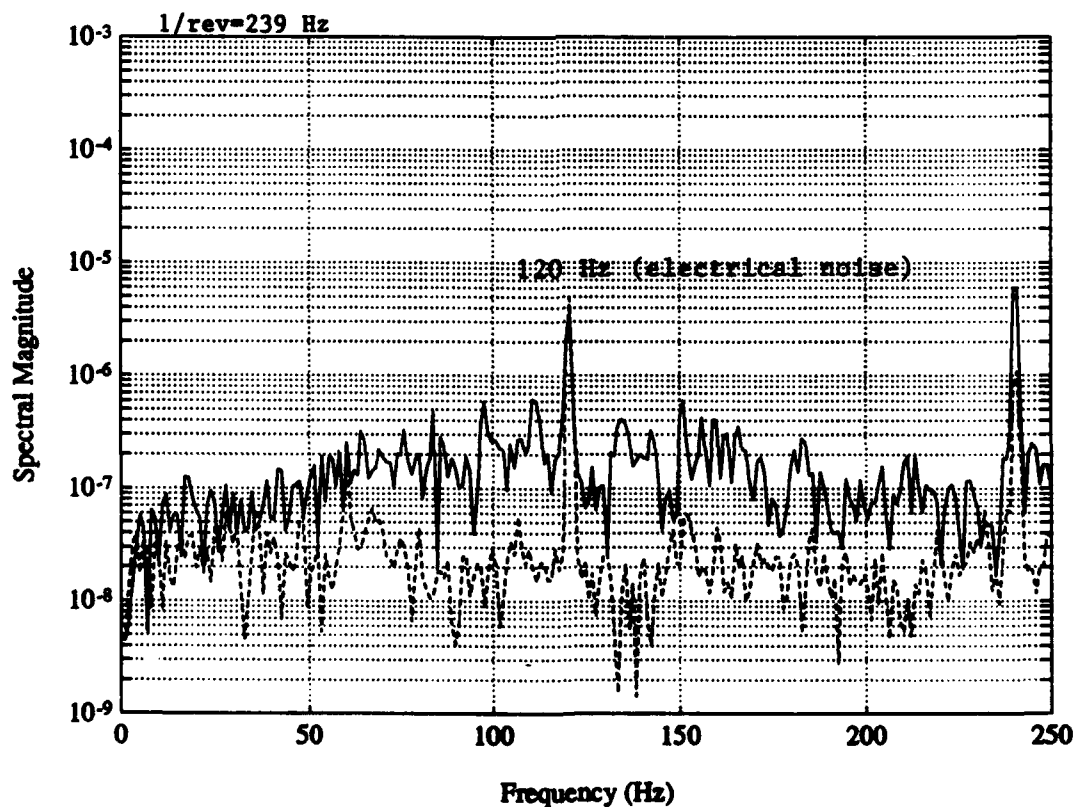


Figure 5.9 First and second spatial Fourier modes - 70% speed, Rotor 4

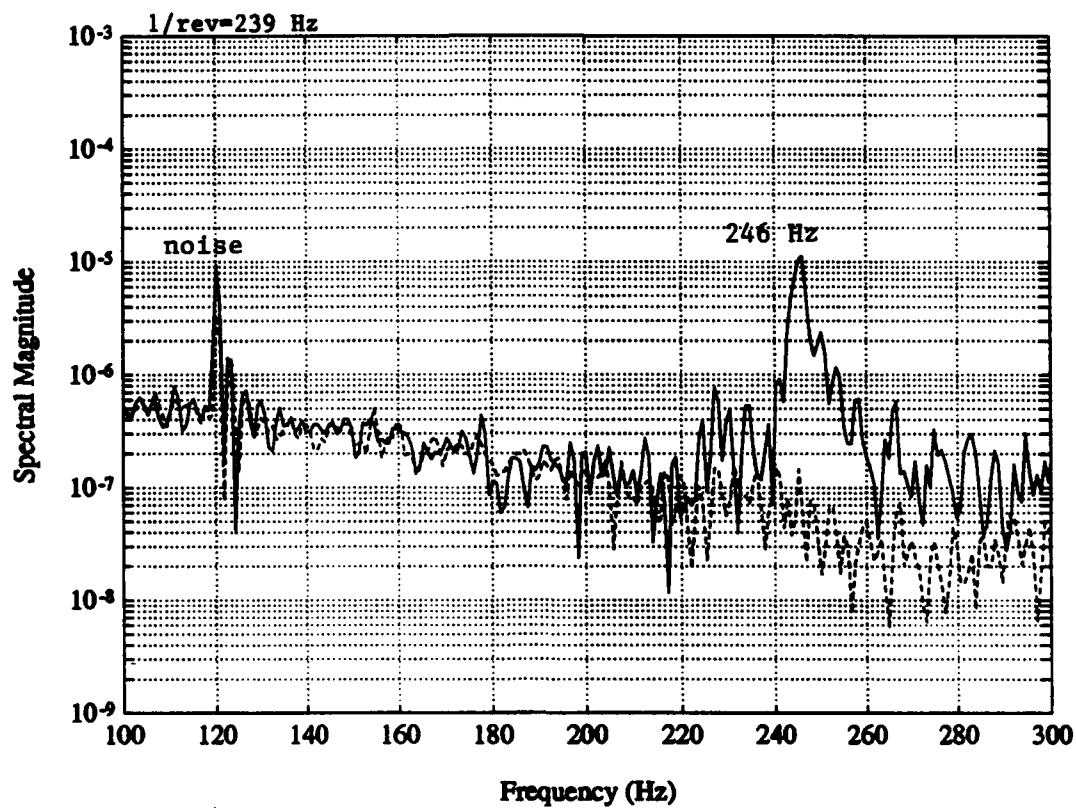


a. including stall

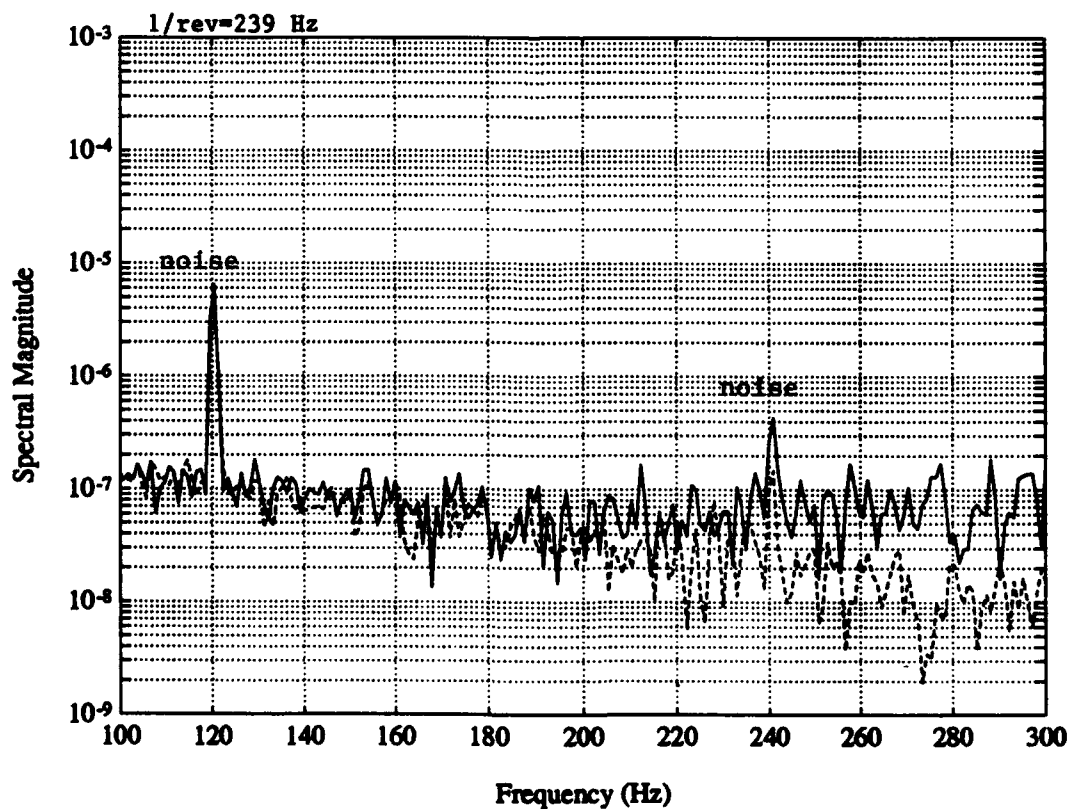


b. up to stall

Figure 5.10 Spectra of SFC #1 transient data at 70% speed, Rotor 4



a. including stall



b. up to stall

Figure 5.11 Spectra of SFC #2 transient data at 70% speed, Rotor 4

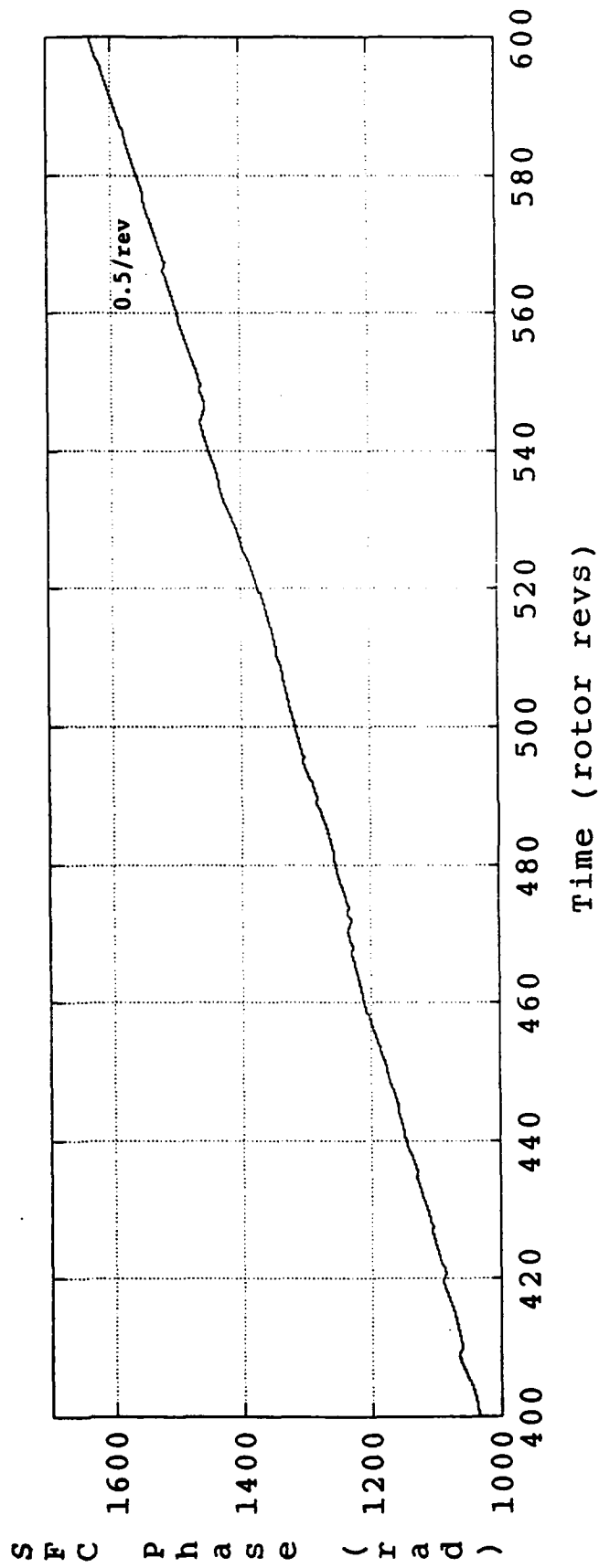
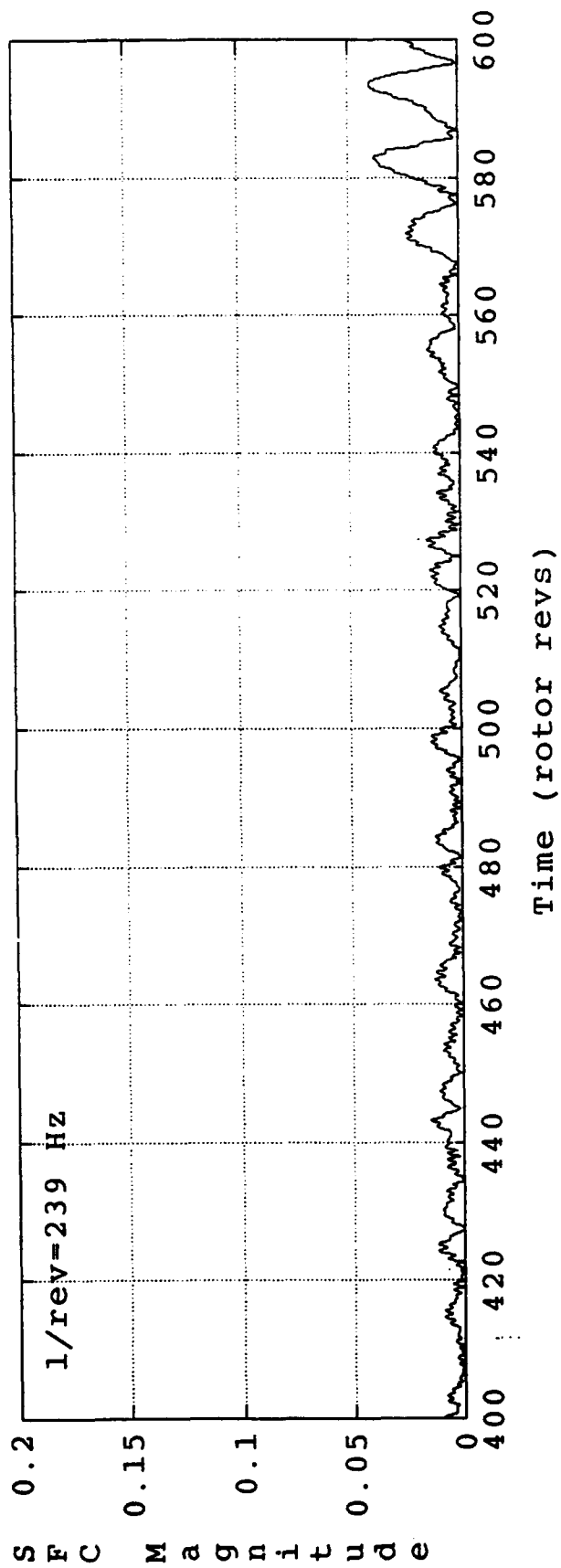


Figure 5.12 SFC #1 of 70% speed transient data, Rotor 6

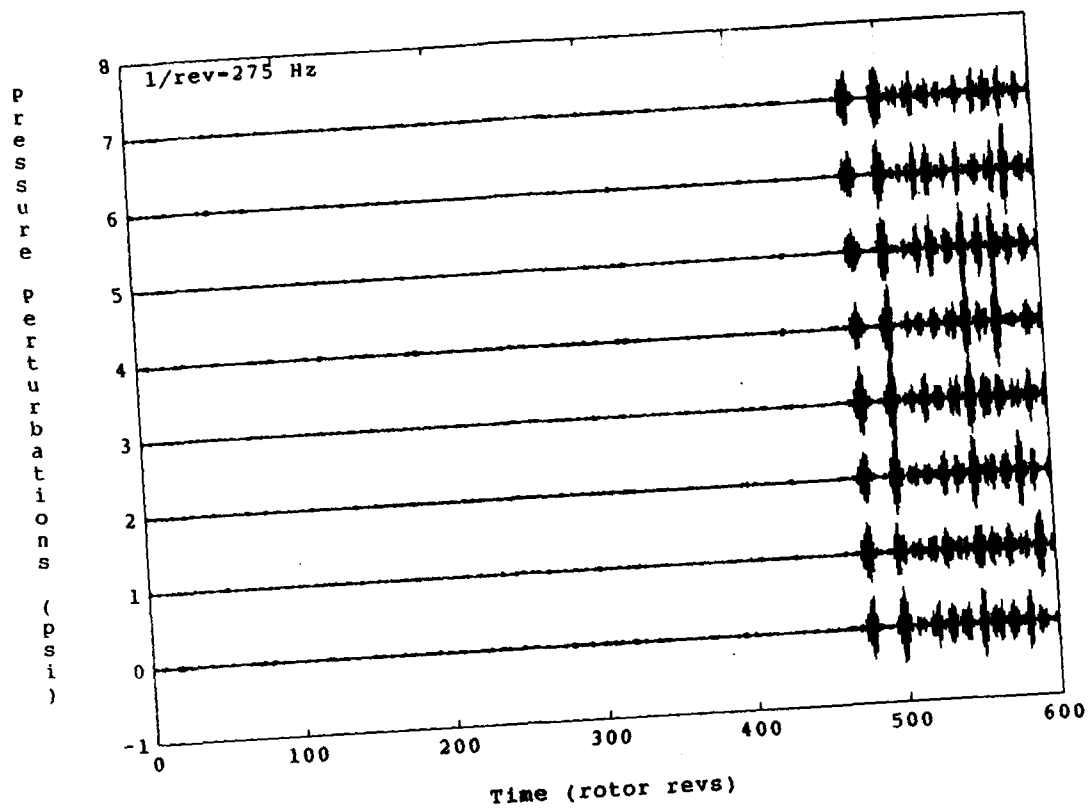


Figure 5.13 Pressure traces - 80% speed transient, Rotor 4

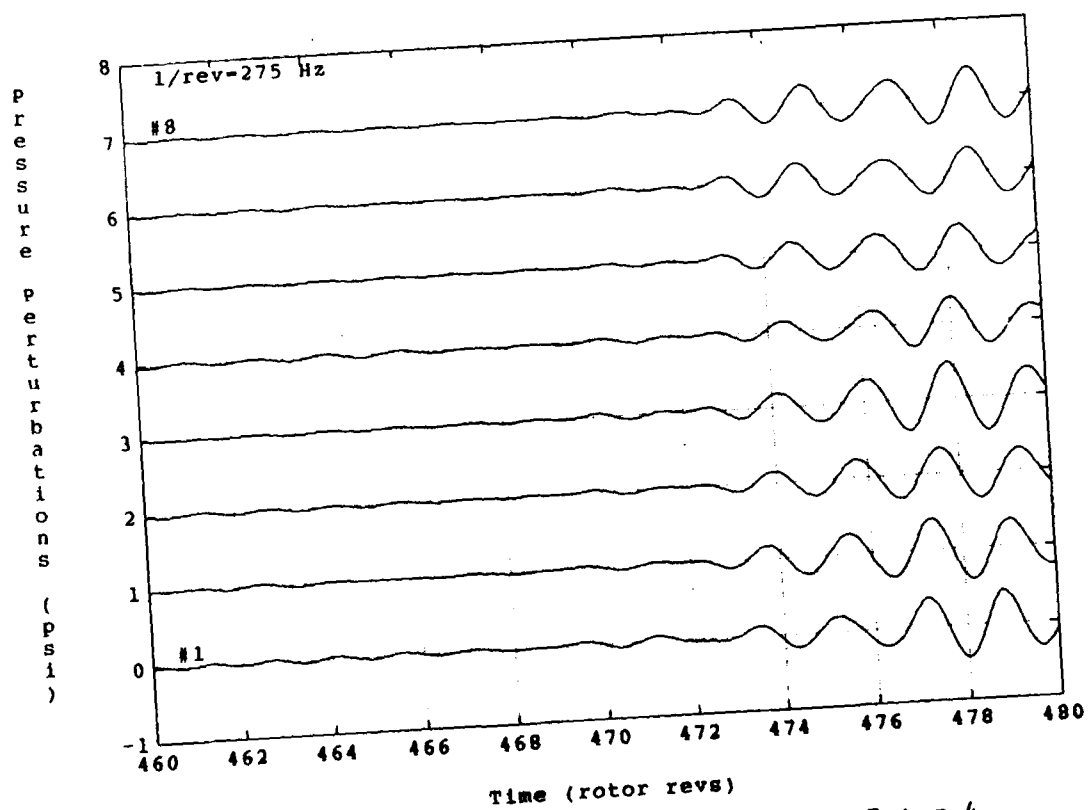


Figure 5.14 Stall inception at 80% speed, Rotor 4

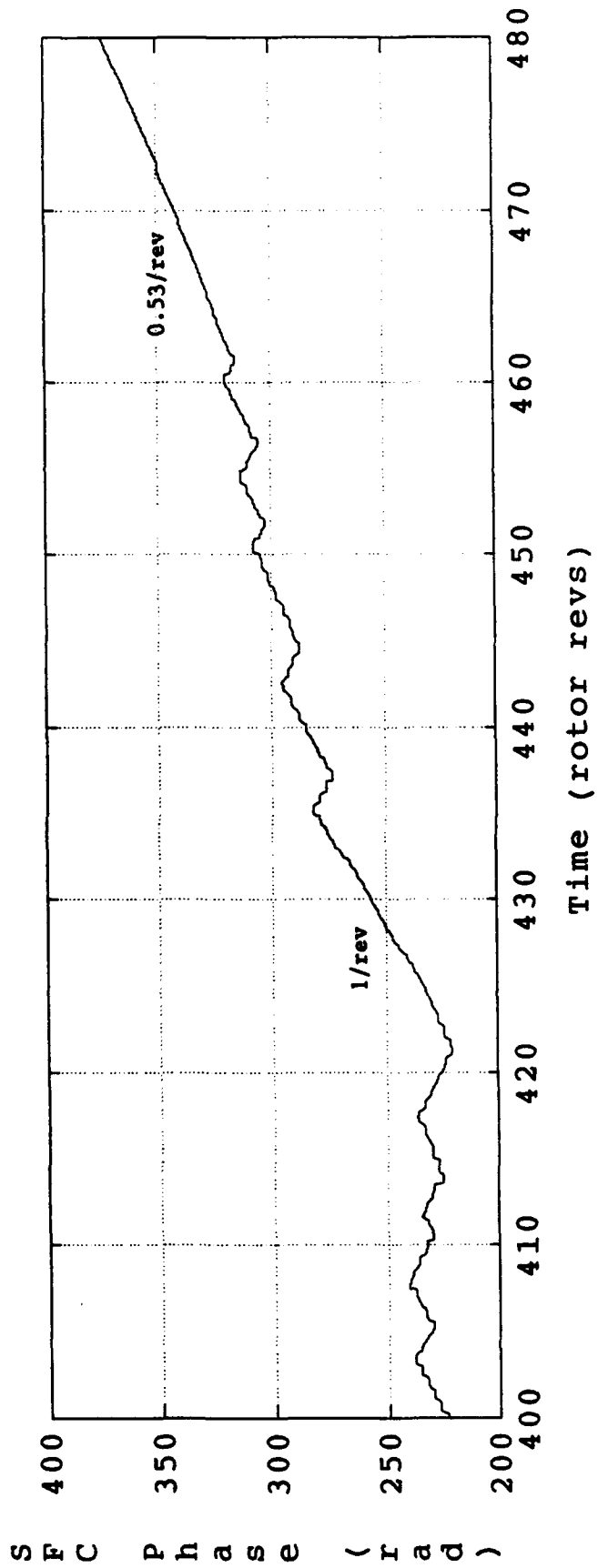
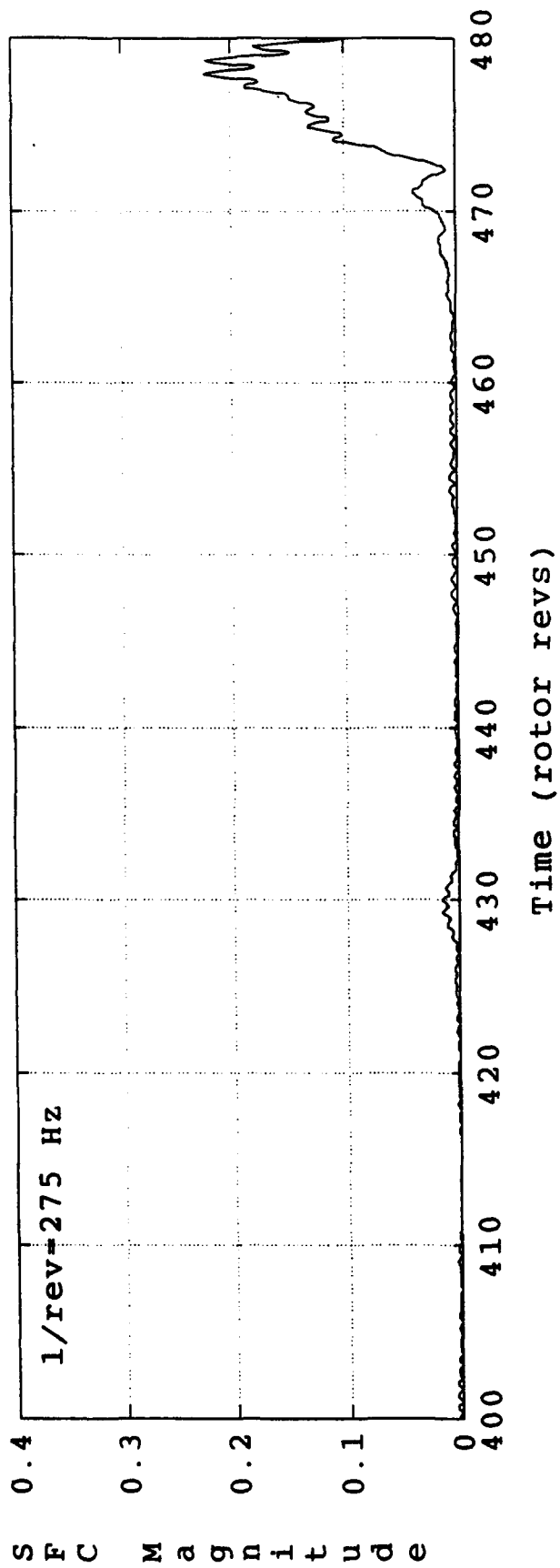


Figure 5.15 Amplitude and phase of SFC #1 - 80% speed, Rotor 4

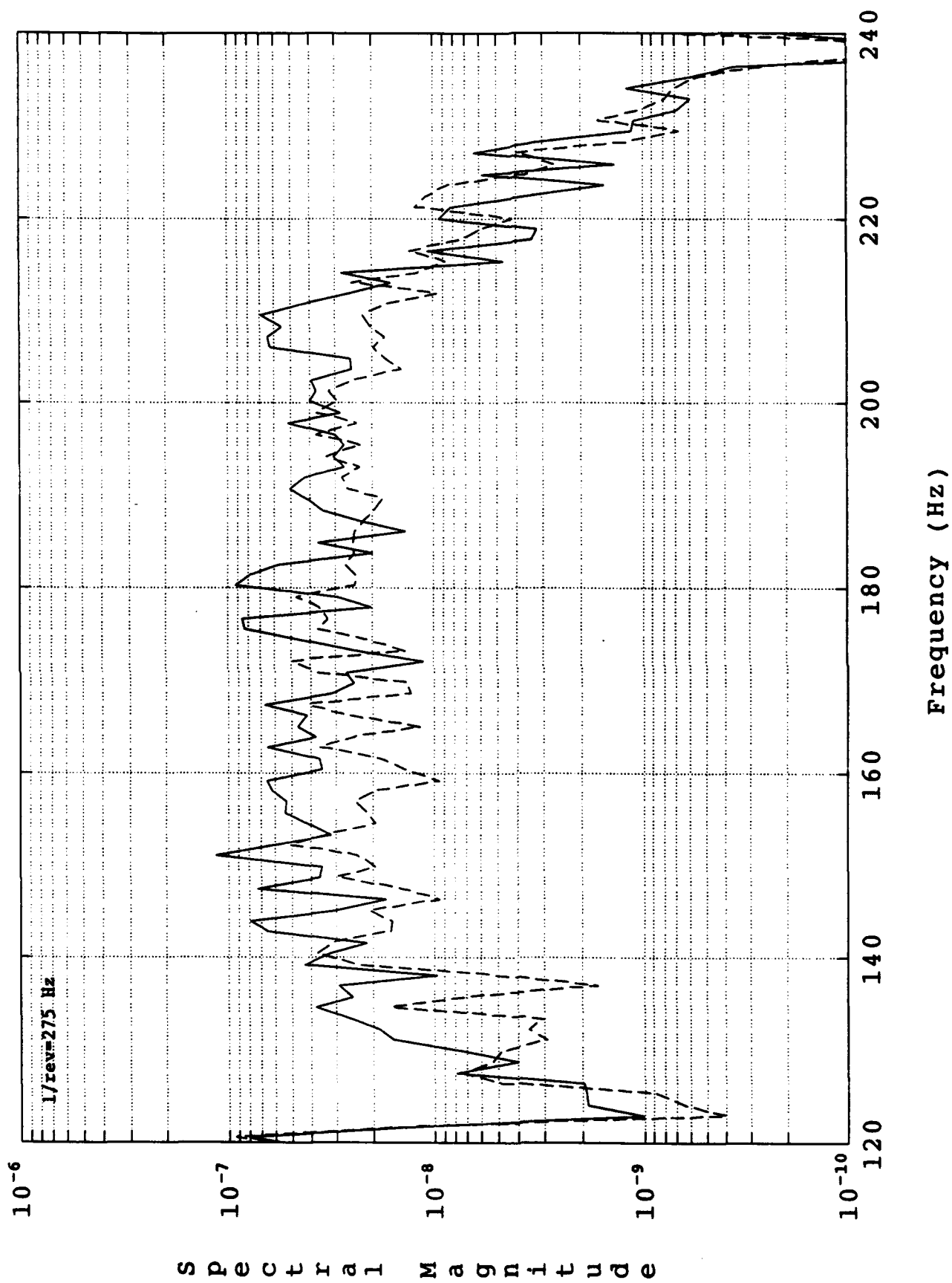


Figure 5.16 PSD of SFC #1 using transient data set up to stall - 80% speed, Rotor 4

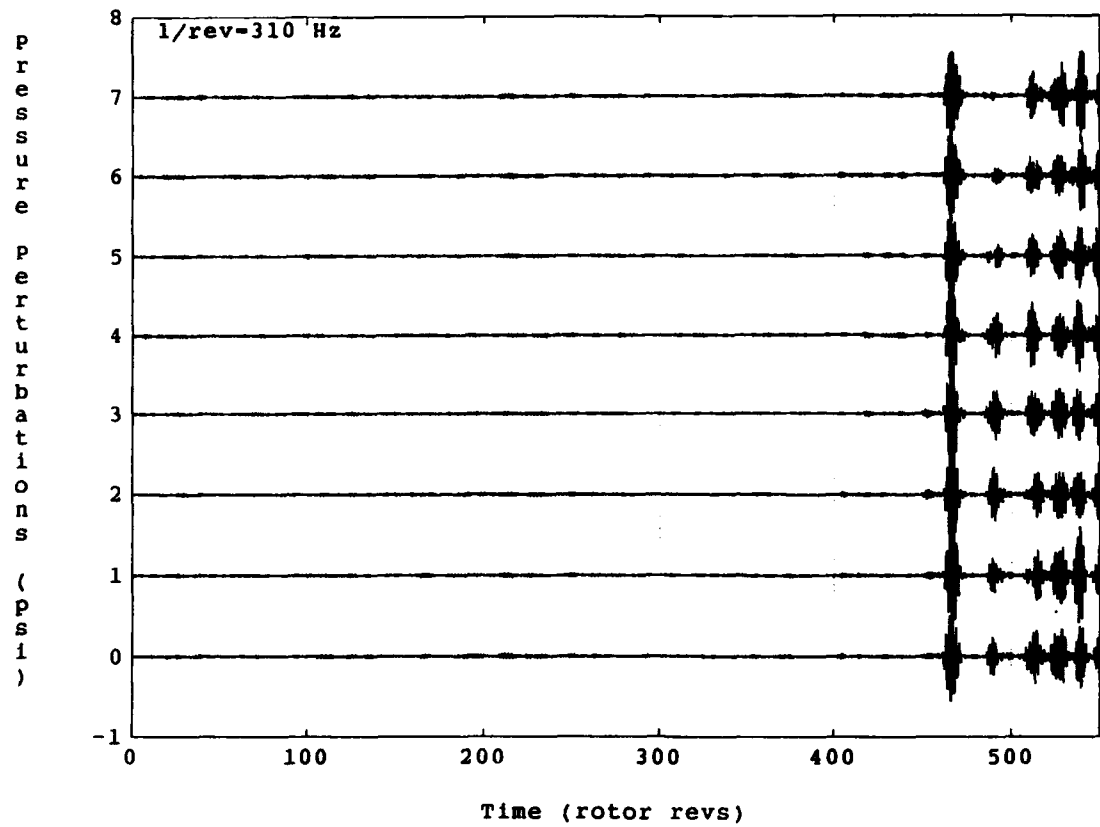


Figure 5.17 Pressure traces during 90% speed transient, Rotor 4

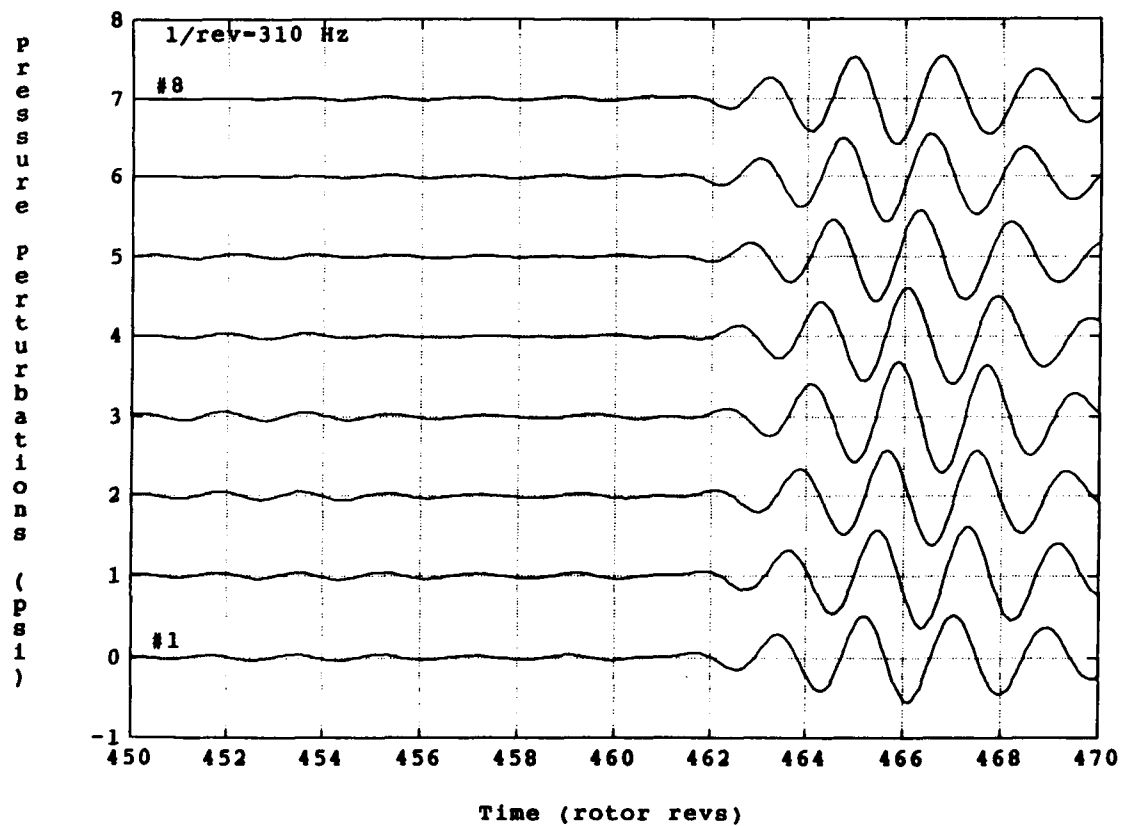


Figure 5.18 Stall inception at 90% speed, Rotor 4

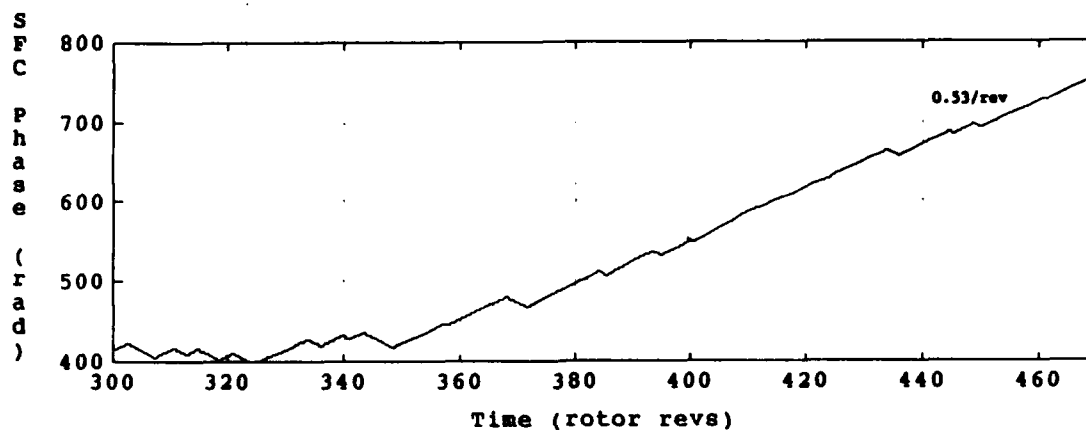
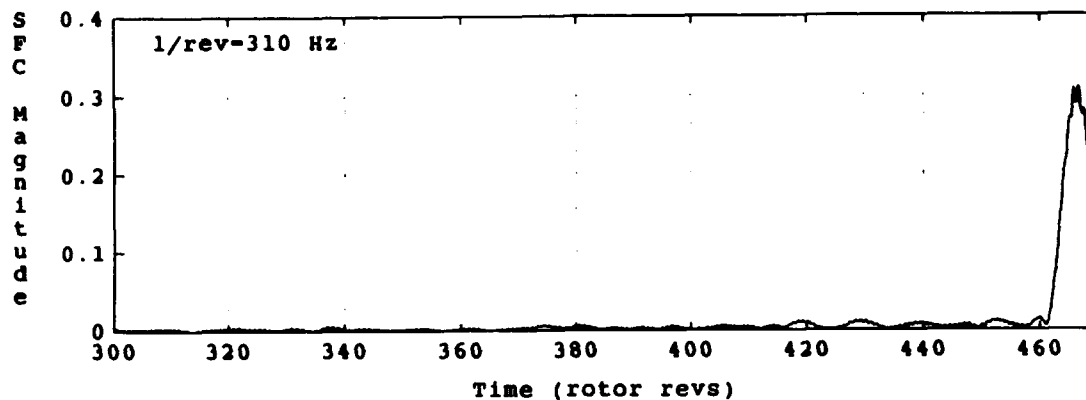


Figure 5.19 SFC #1 amplitude and phase - 90% speed, Rotor 4

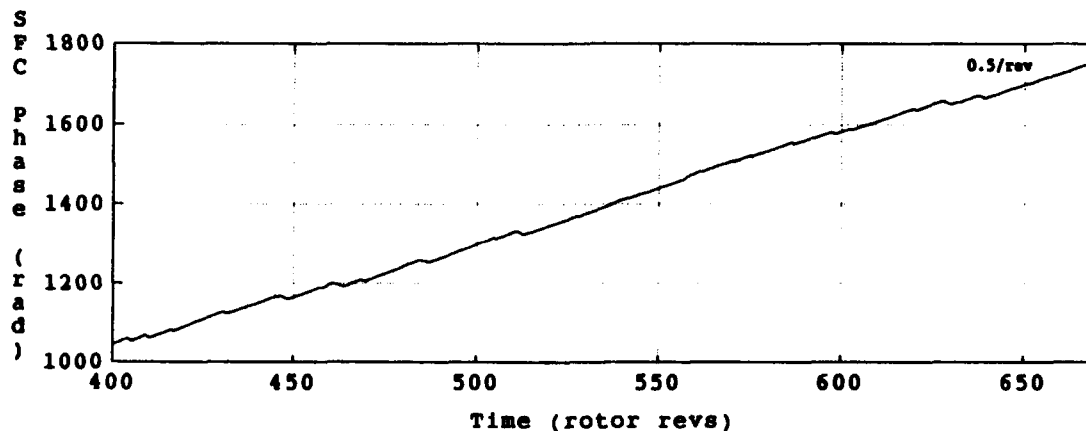
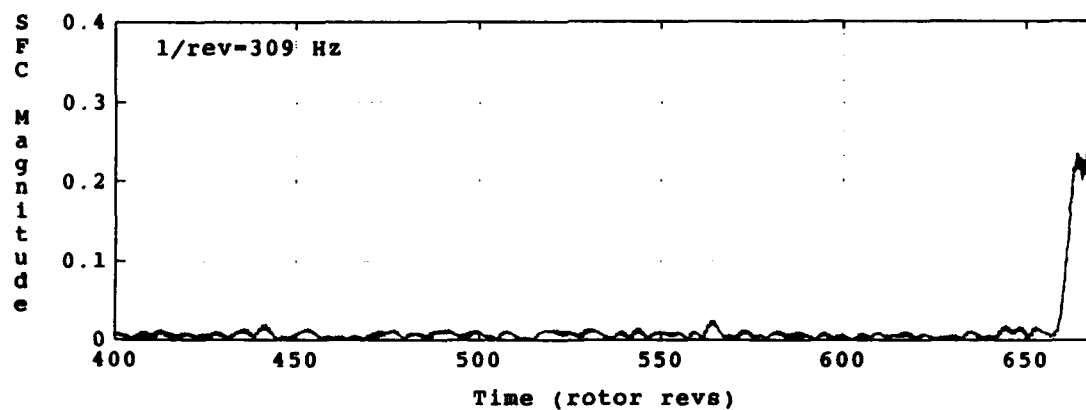


Figure 5.20 SFC #1 amplitude and phase - 90% speed, Rotor 6

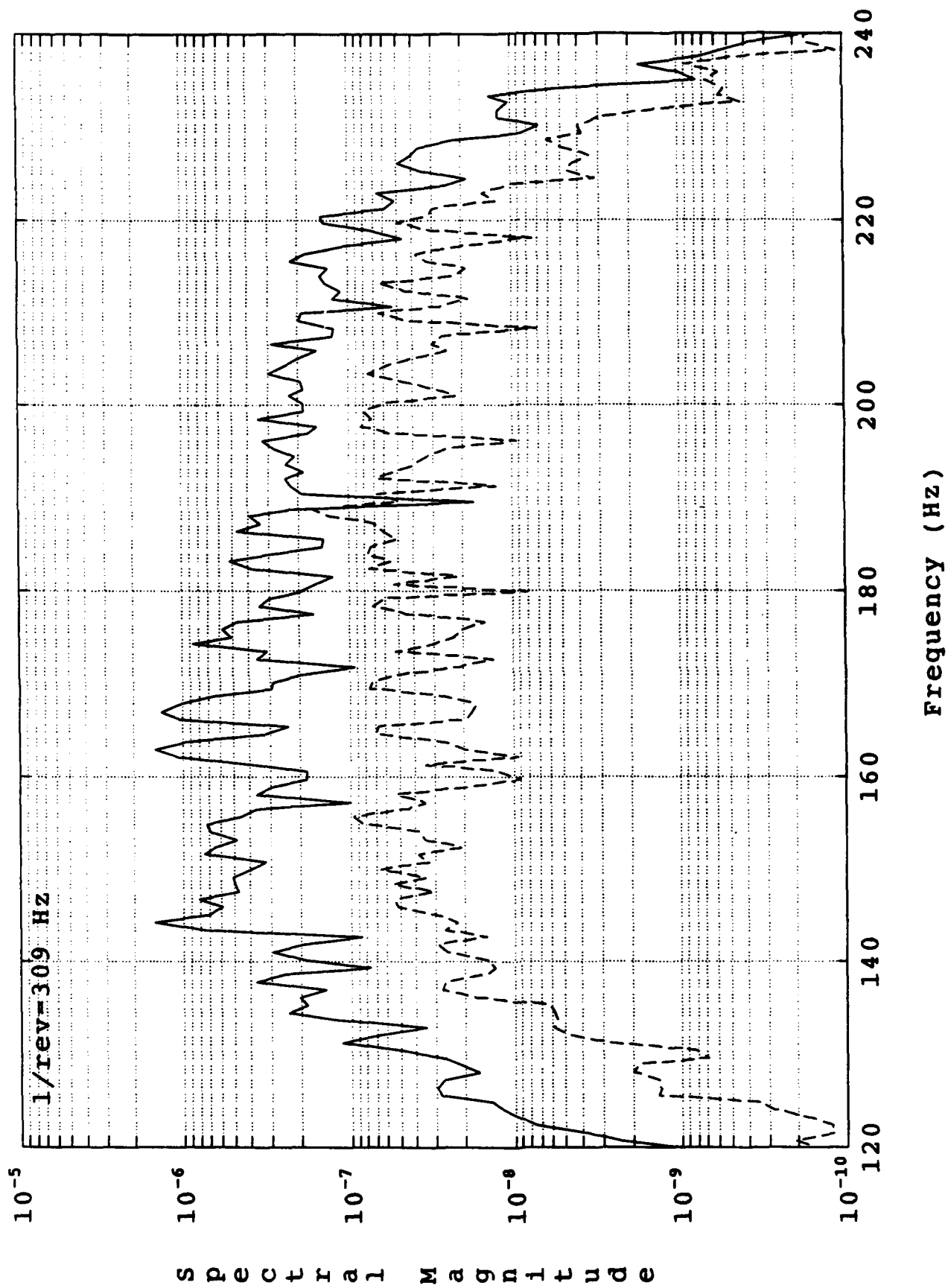


Figure 5.21 PSD of SFC #1 using transient data set up to stall - 90% speed, Rotor 6

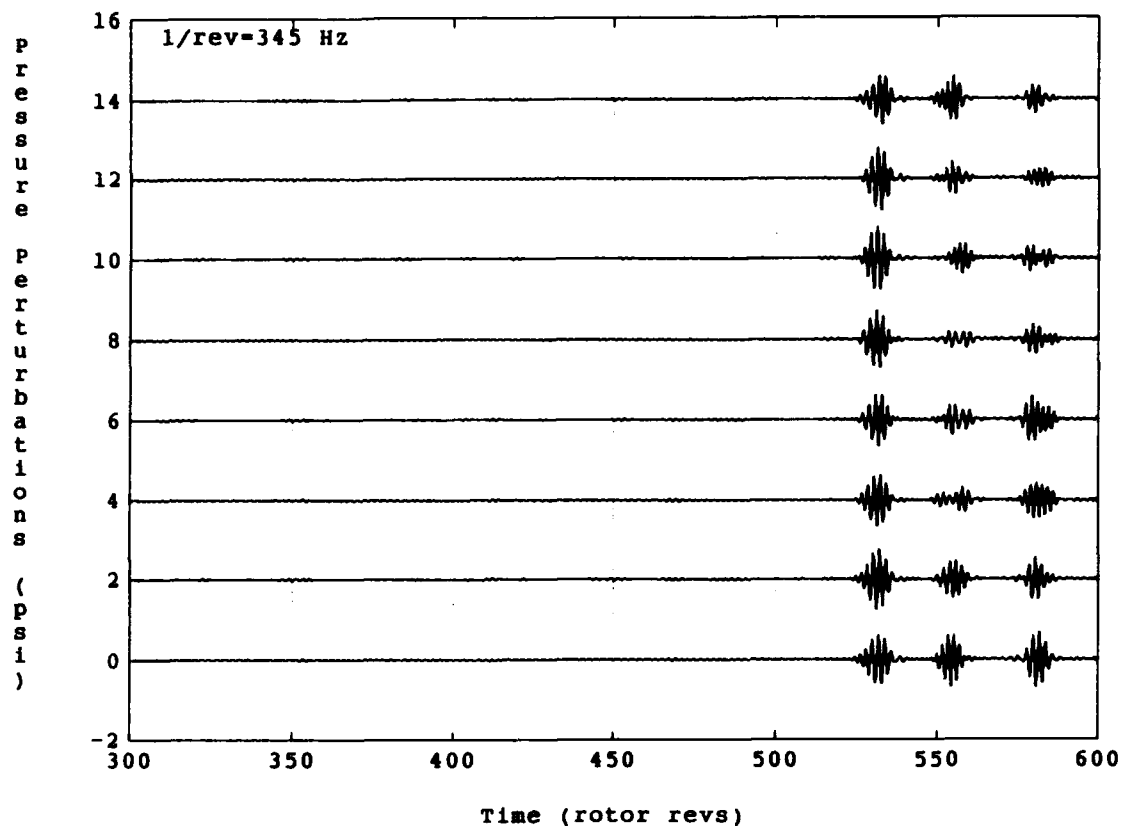


Figure 5.22 Pressure traces during 100% speed transient, Rotor 6

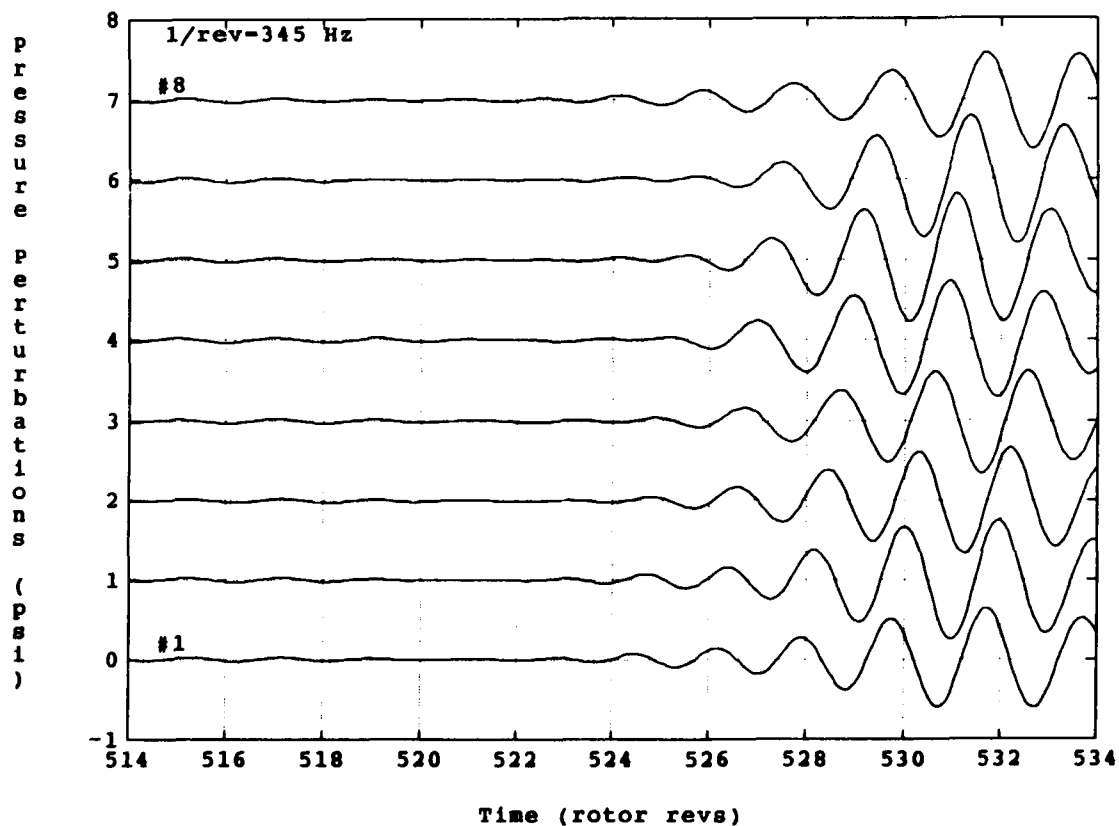


Figure 5.23 Stall inception at 100% speed, Rotor 6

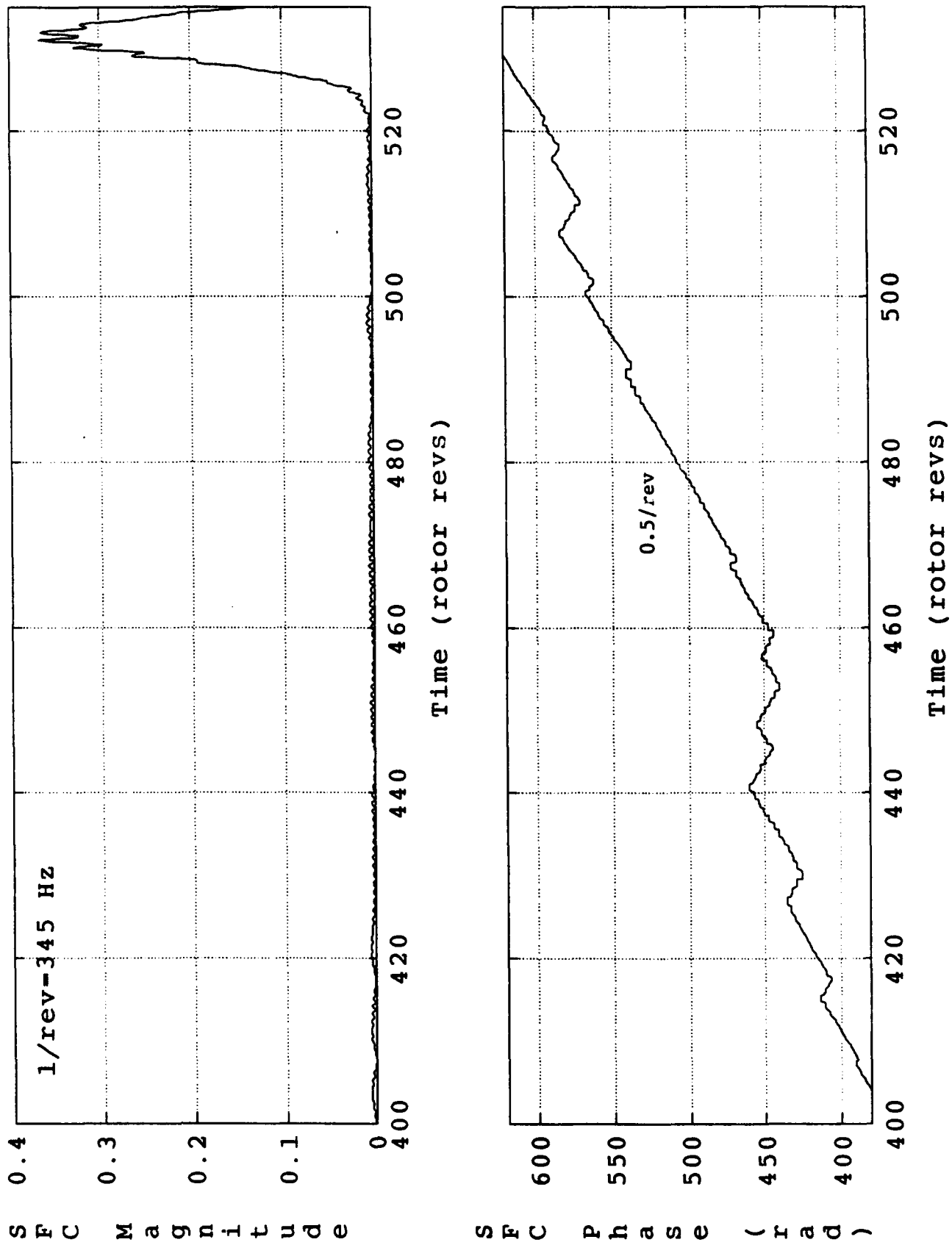
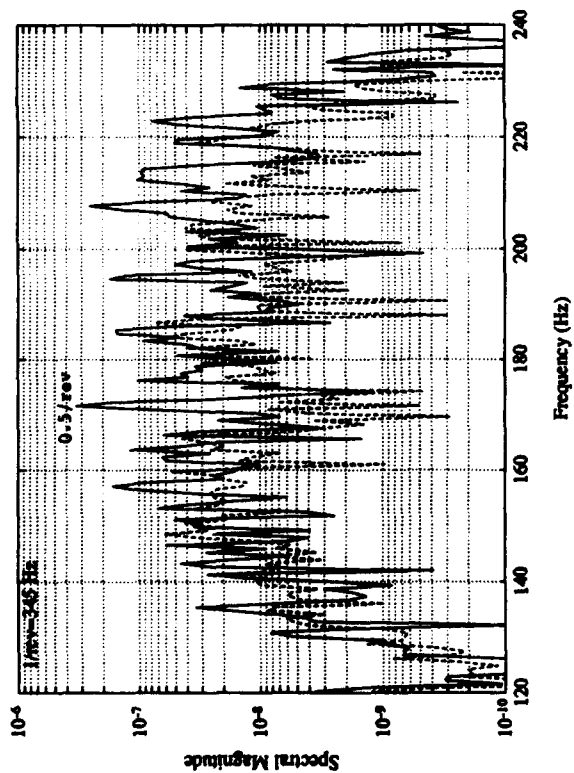
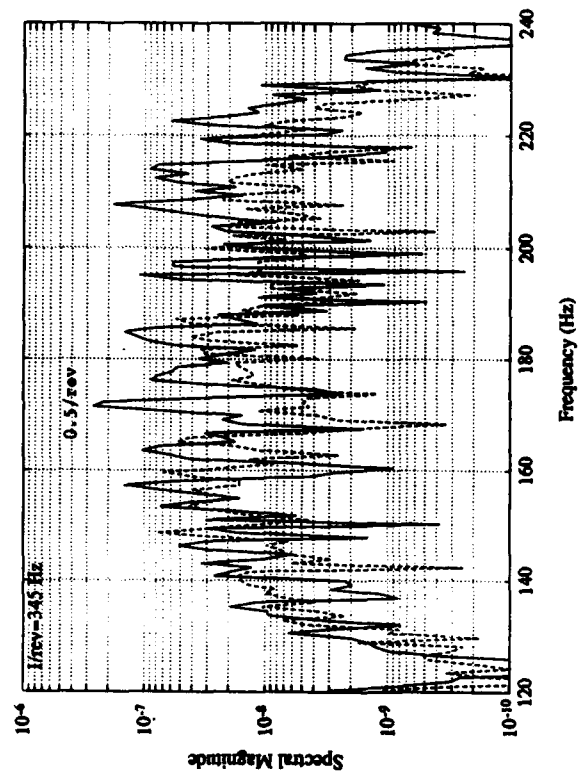


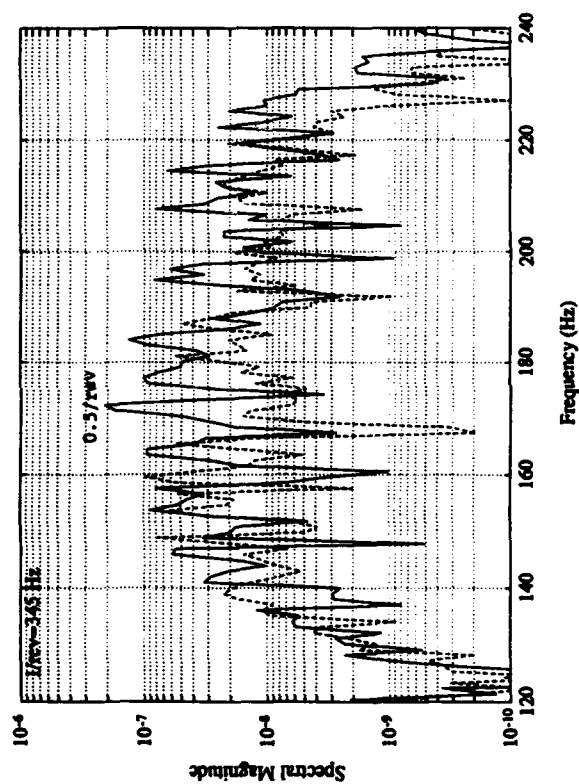
Figure 5.24 SFC #1 amplitude and phase - 100% speed, Rotor 6



a. up to stall



b. 0.25 s prior to stall



c. 0.5 s prior to stall

Figure 5.25 PSD of SFC #1 using different lengths of transient data set - 100% speed, Rotor 6

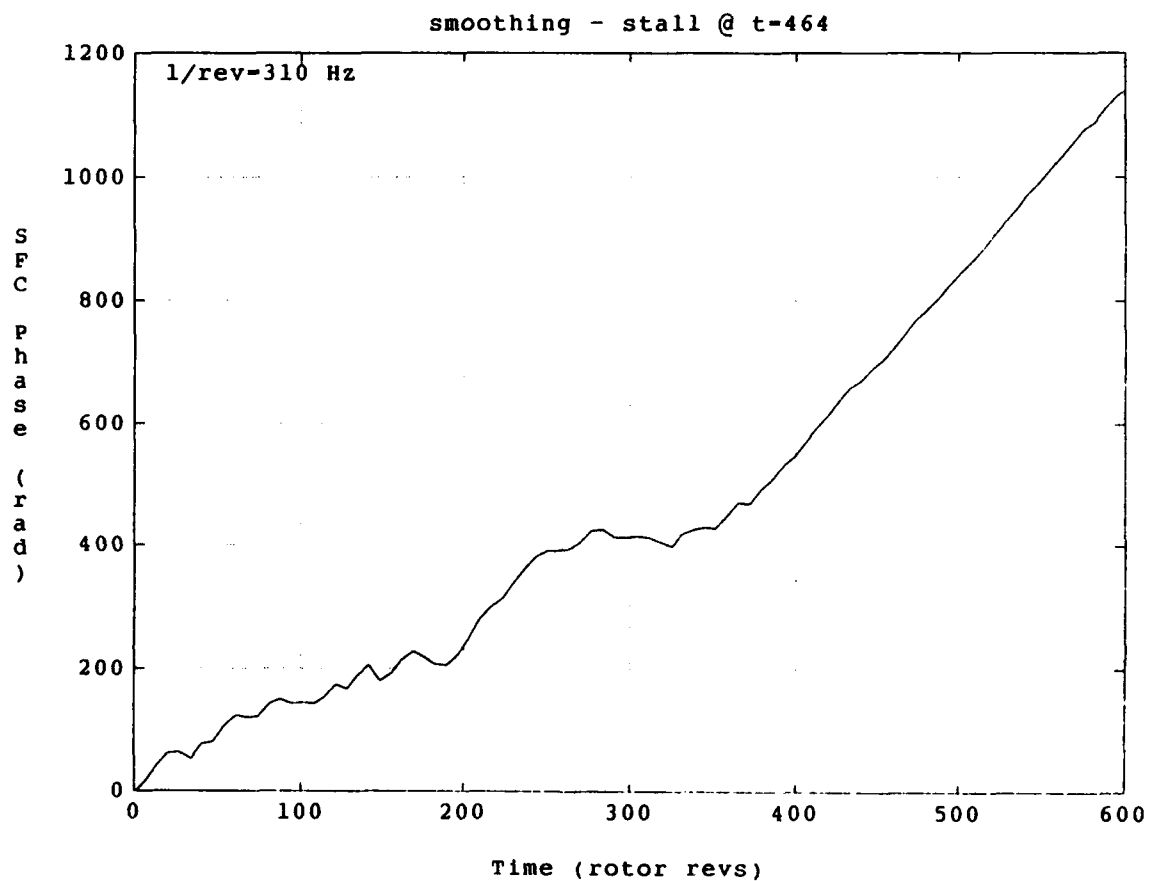
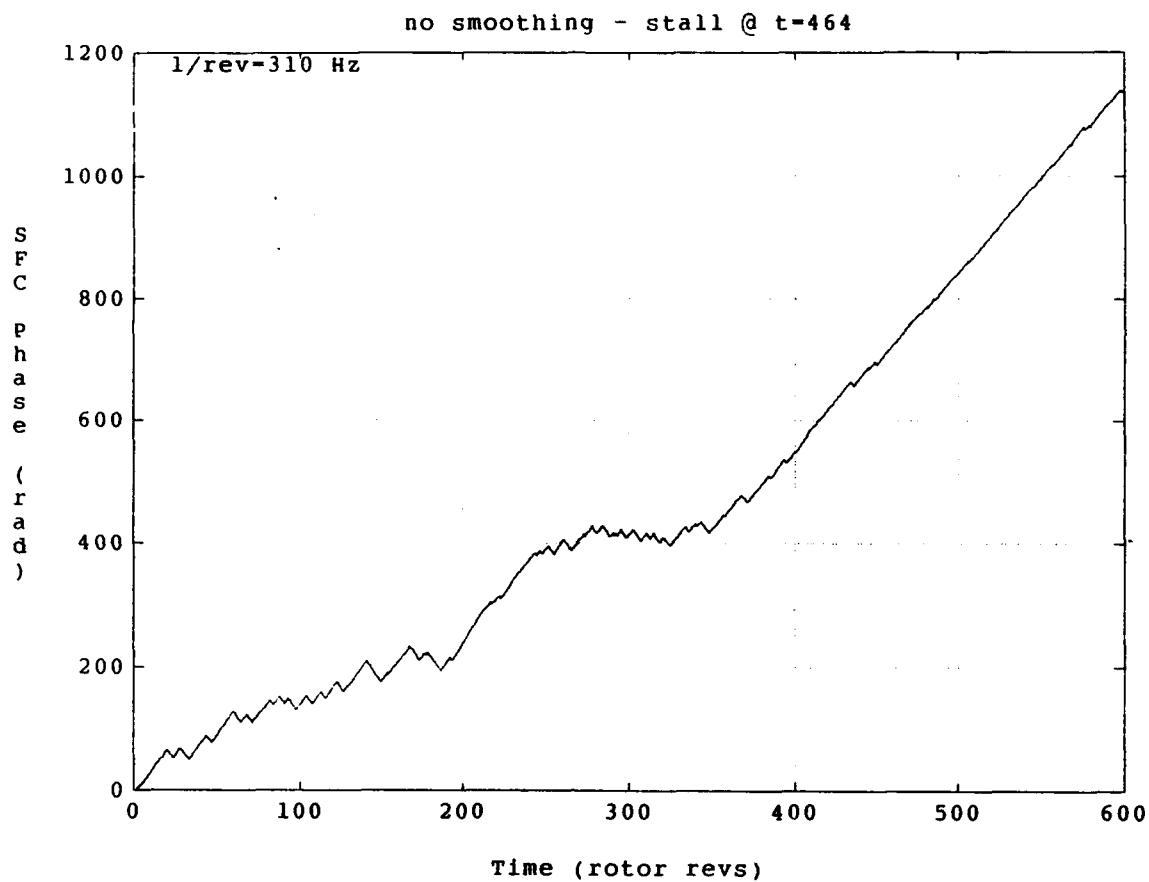


Figure 5.26 Example of smoothed SFC #1 phase data - 90% speed

stall @ t=485

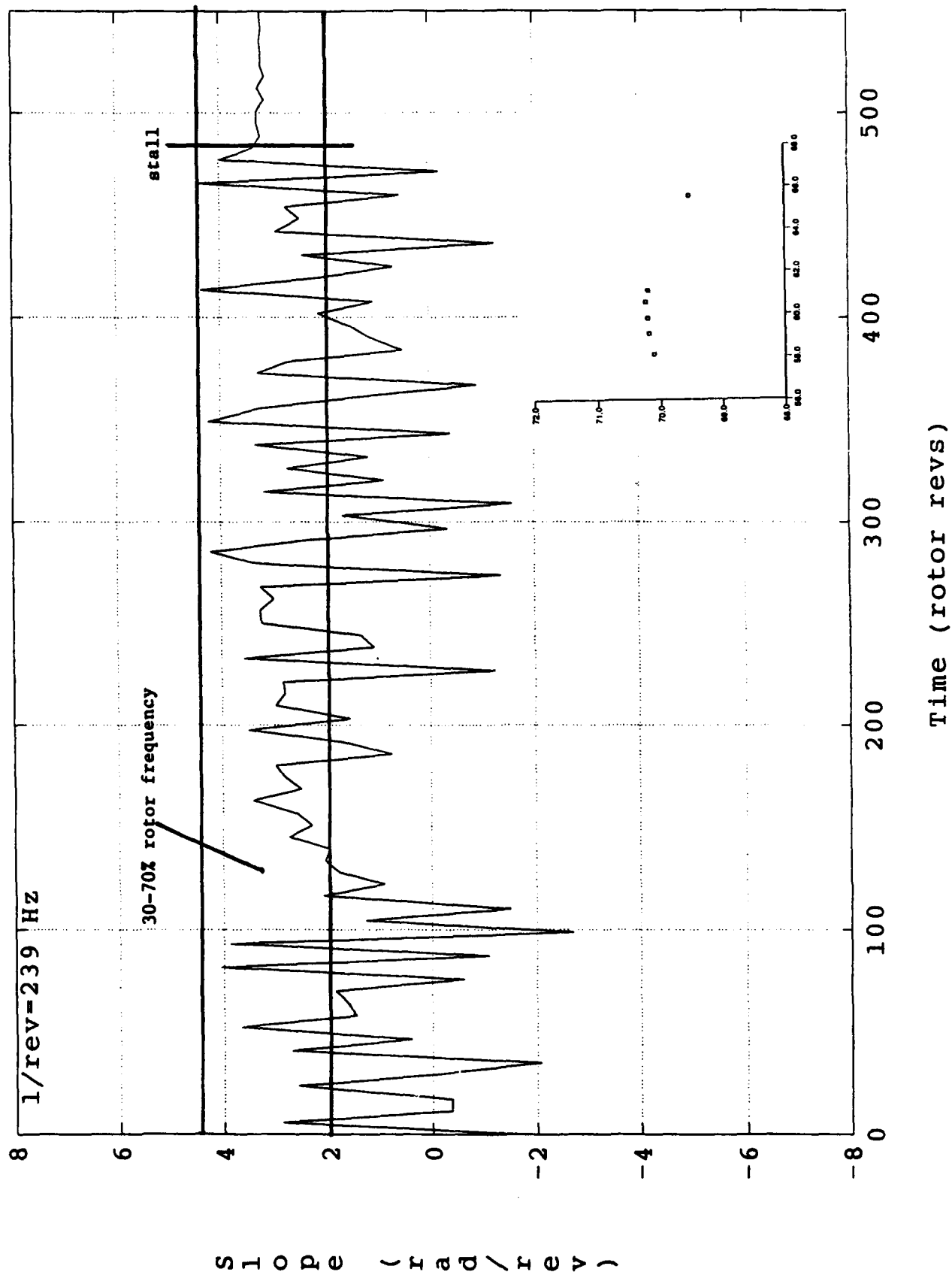


Figure 5.27 Slope of SFC #1 phase - 70% speed, Rotor 4

progressive stall starting @ t=580

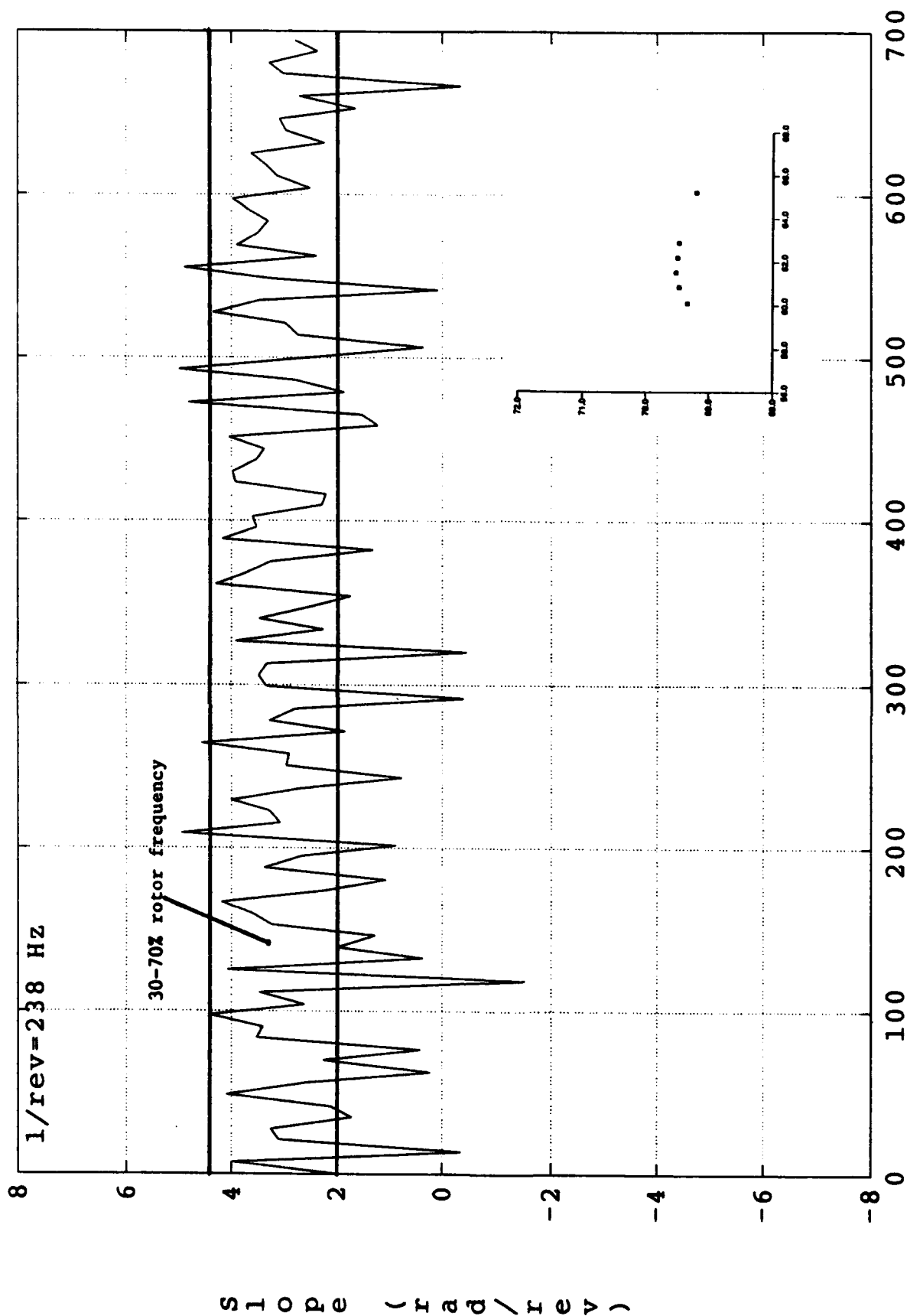
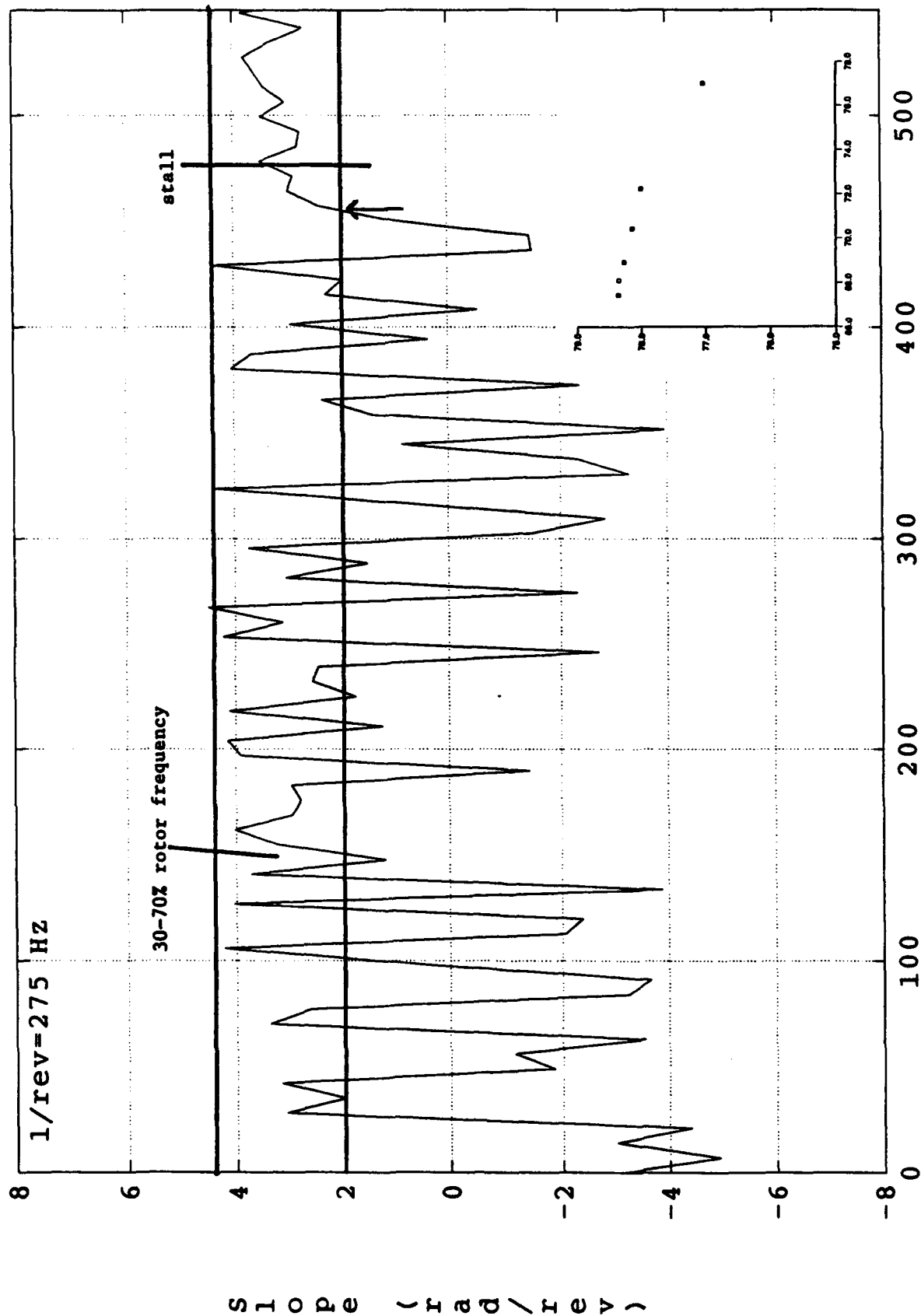


Figure 5.28 Slope of SFC #1 phase - 70% speed, Rotor 6

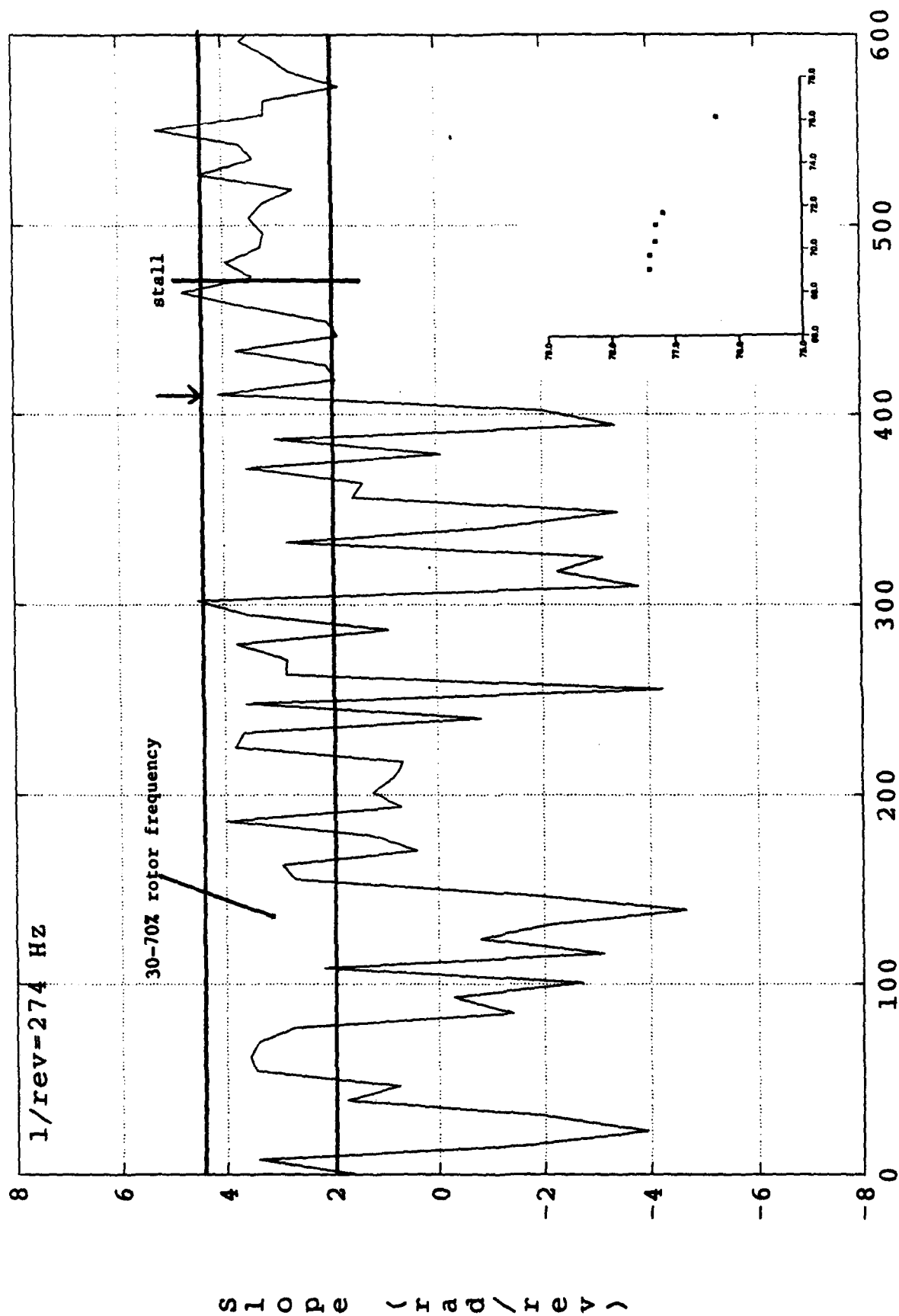
stall @ t=476



Time (rotor revs)

Figure 5.29 Slope of SFC #1 phase - 80% speed, Rotor 4

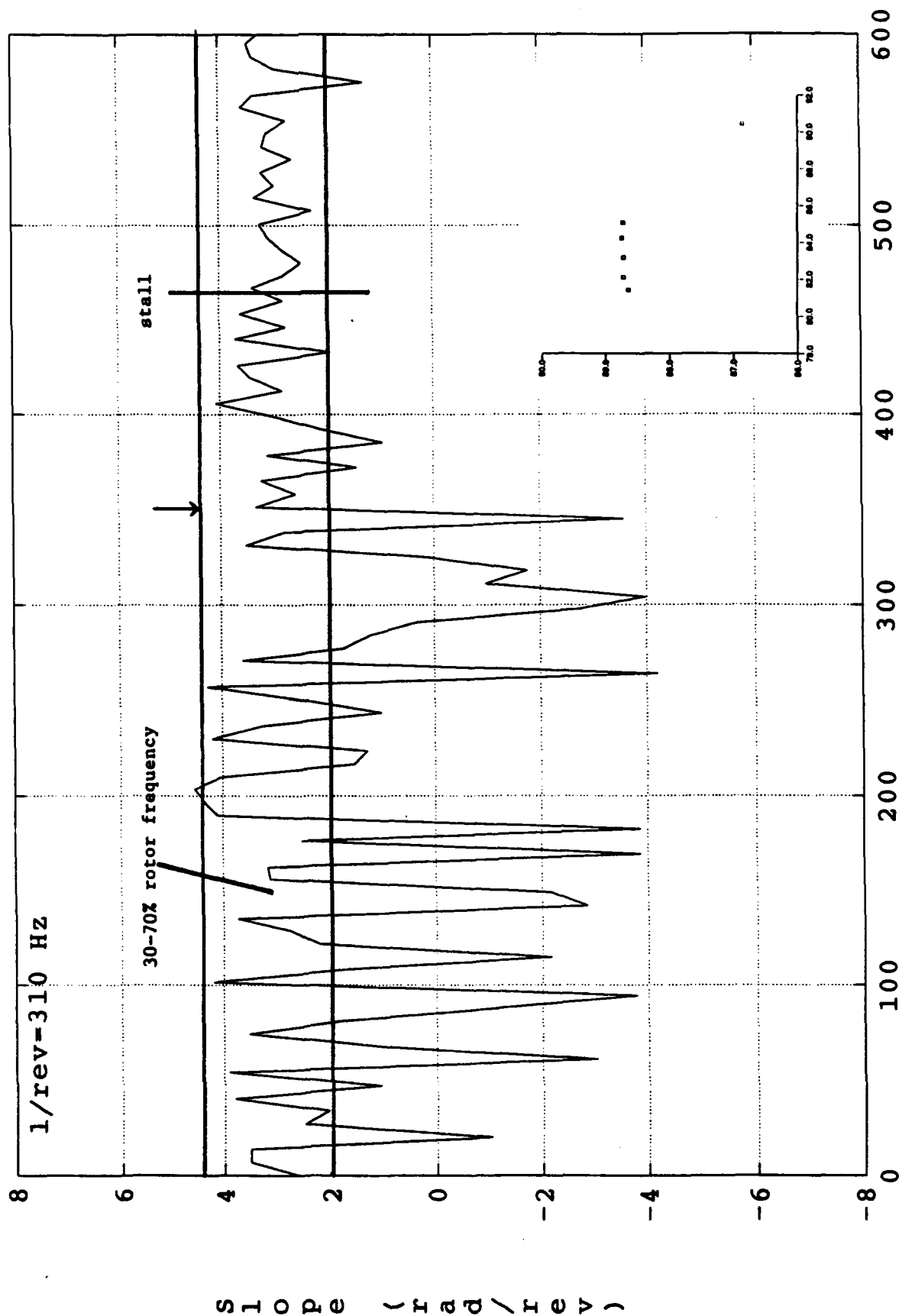
stall @ t=470



Time (rotor revs)

Figure 5.30 Slope of SFC #1 phase - 80% speed, Rotor 6

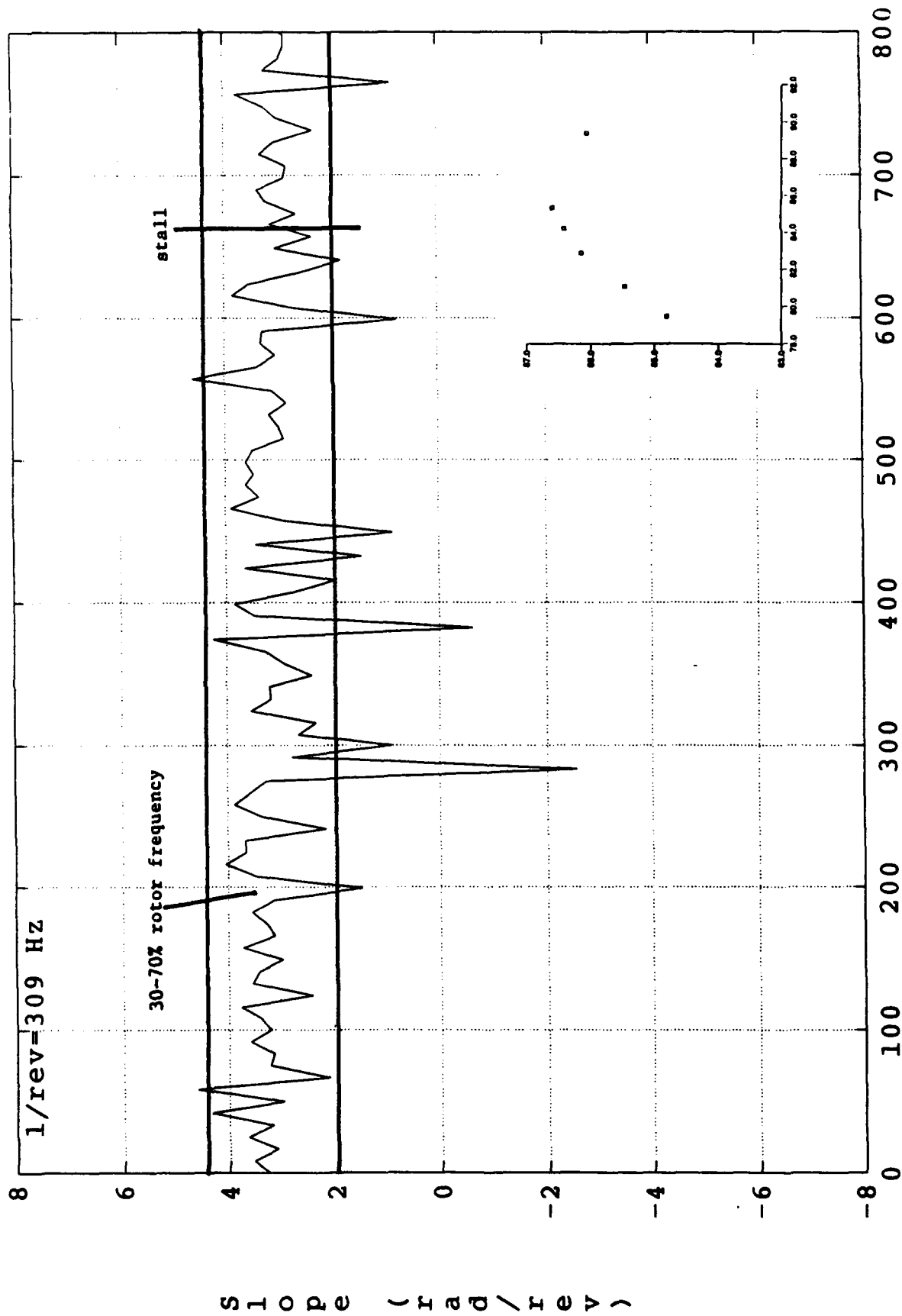
stall @ t=464



Time (rotor revs)

Figure 5.31 Slope of SFC #1 phase - 90% speed, Rotor 4

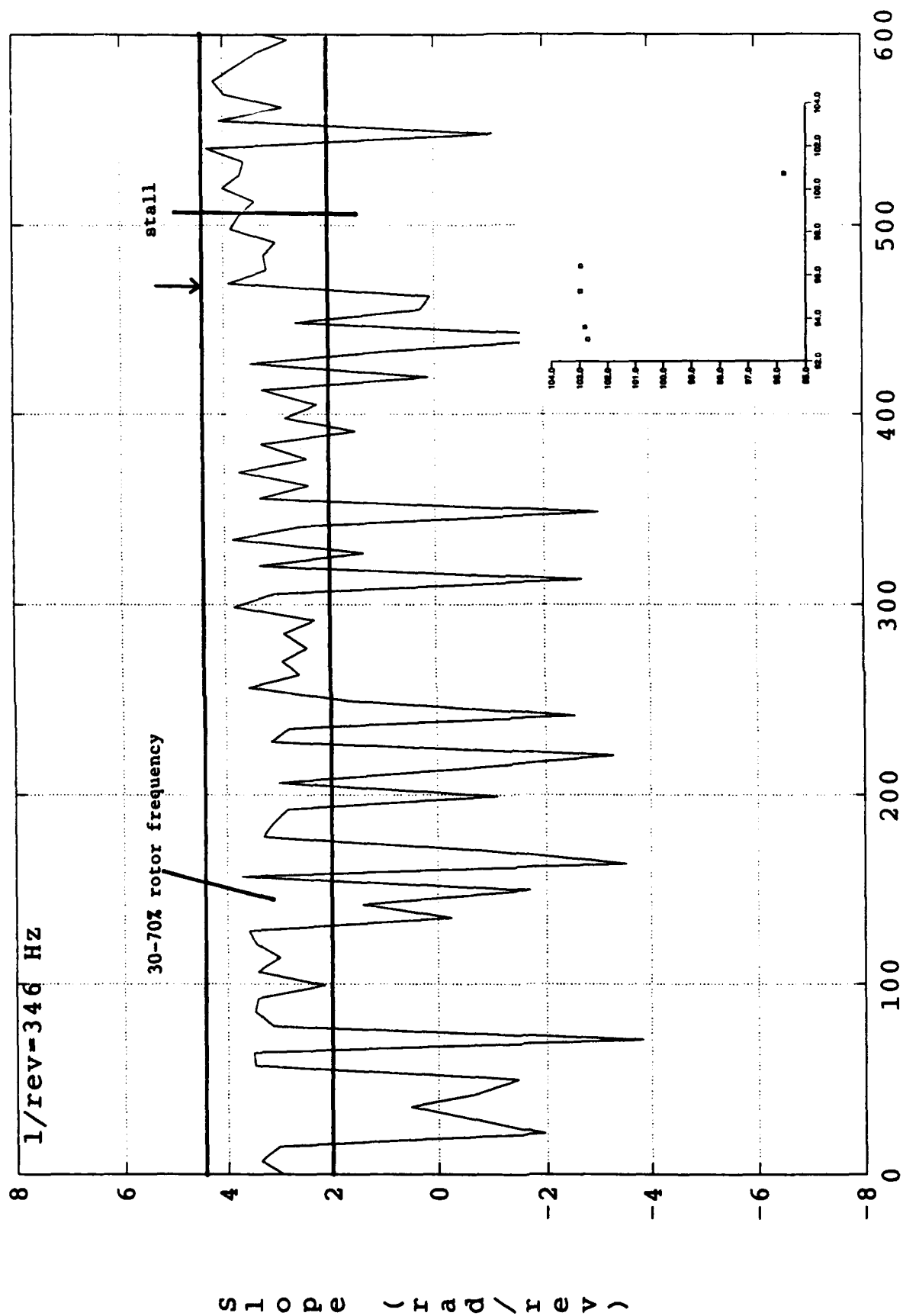
stall @ t=662



Time (rotor revs)

Figure 5.32 Slope of SFC #1 phase - 90% speed, Rotor 6

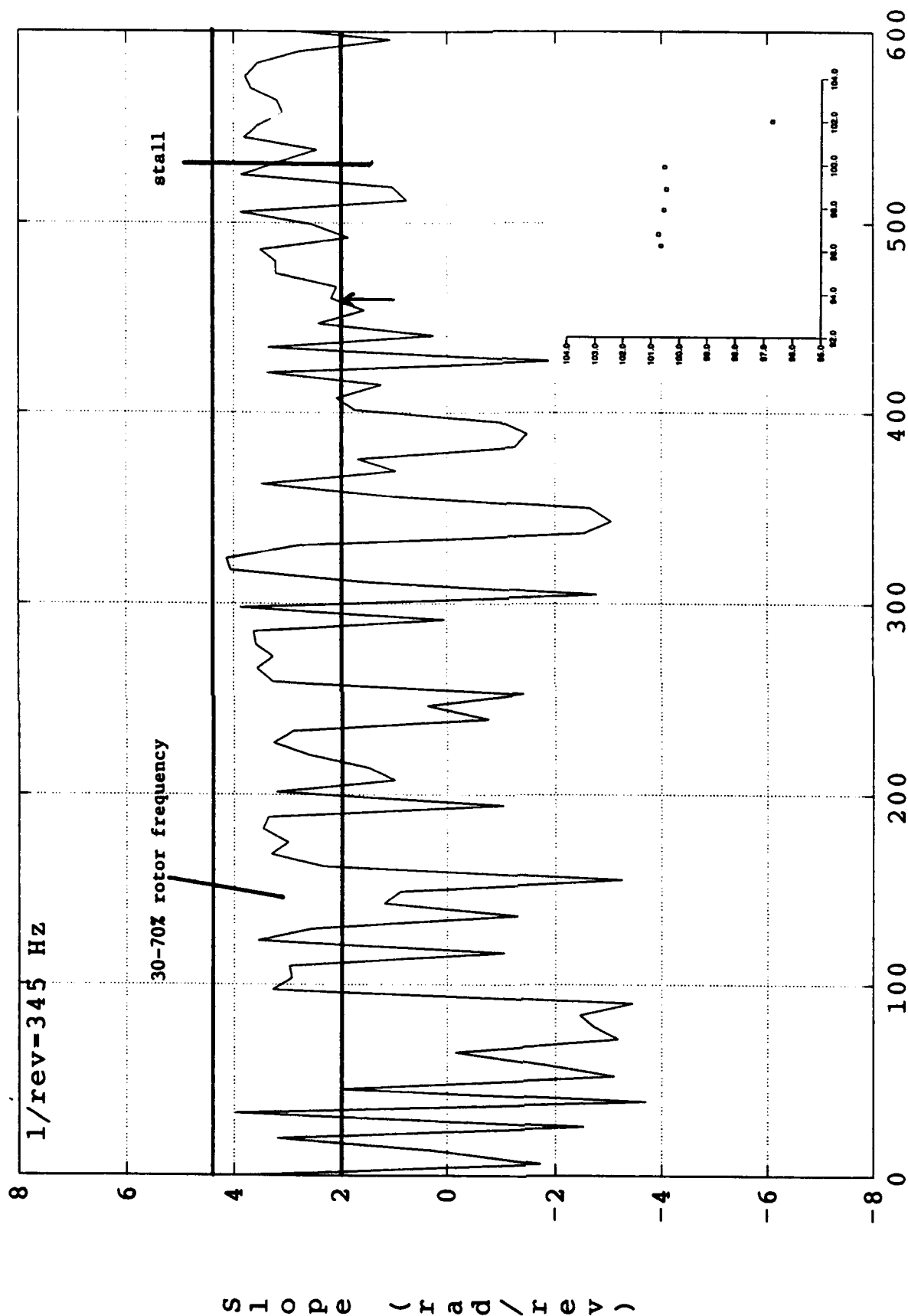
stall @ t=505



Time (rotor revs)

Figure 5.33 Slope of SFC #1 phase - 100% speed, Rotor 4

stall @ t=530



Time (rotor revs)

Figure 5.34 Slope of SFC #1 phase - 100% speed, Rotor 6

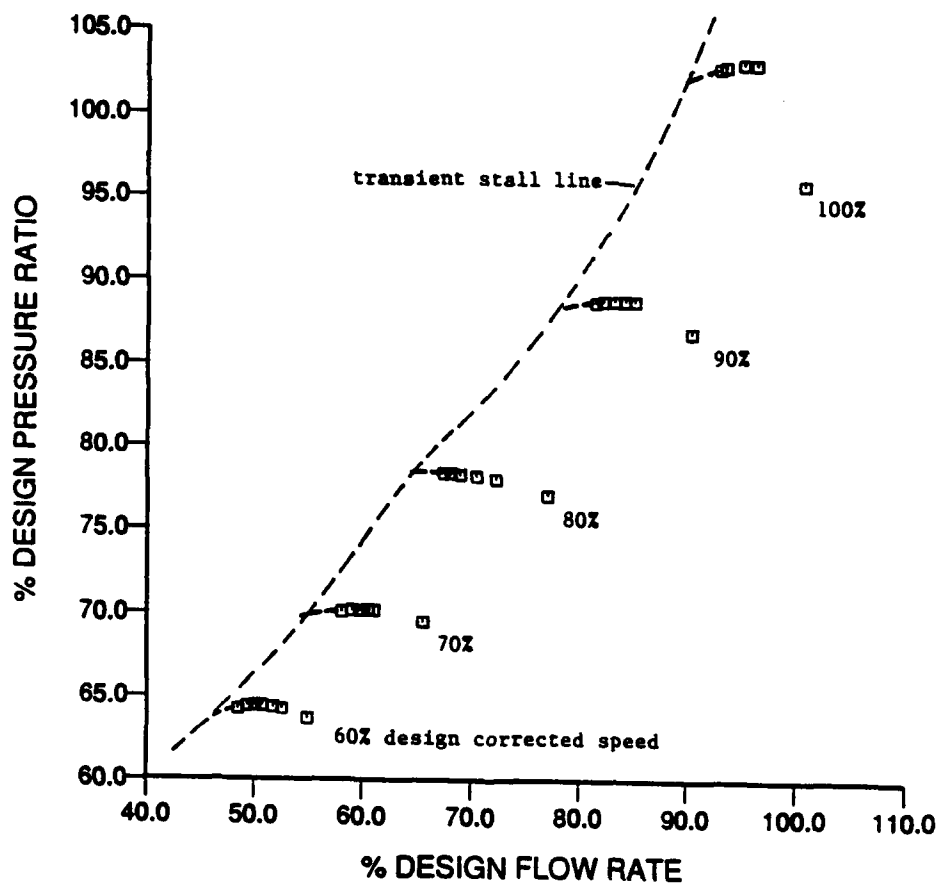


Figure 5.35 Speedline characteristics of Rotor 4 extended to show transient stall line observed during testing

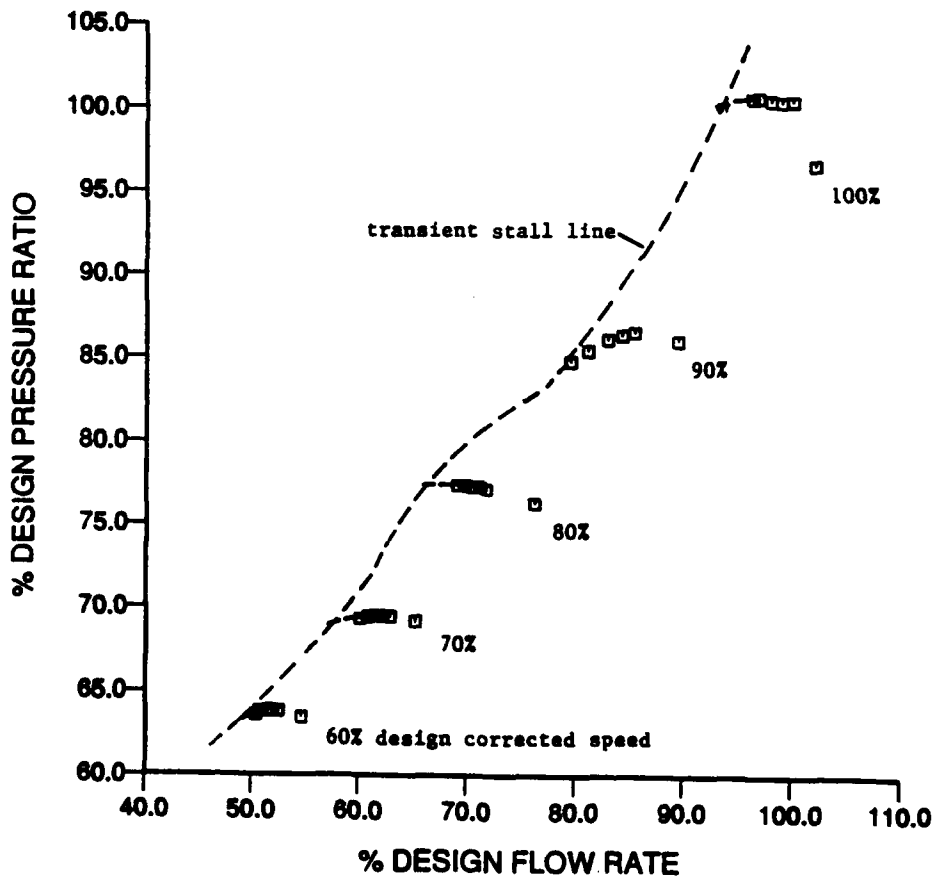


Figure 5.36 Speedline characteristics of Rotor 6 extended to show transient stall line observed during testing

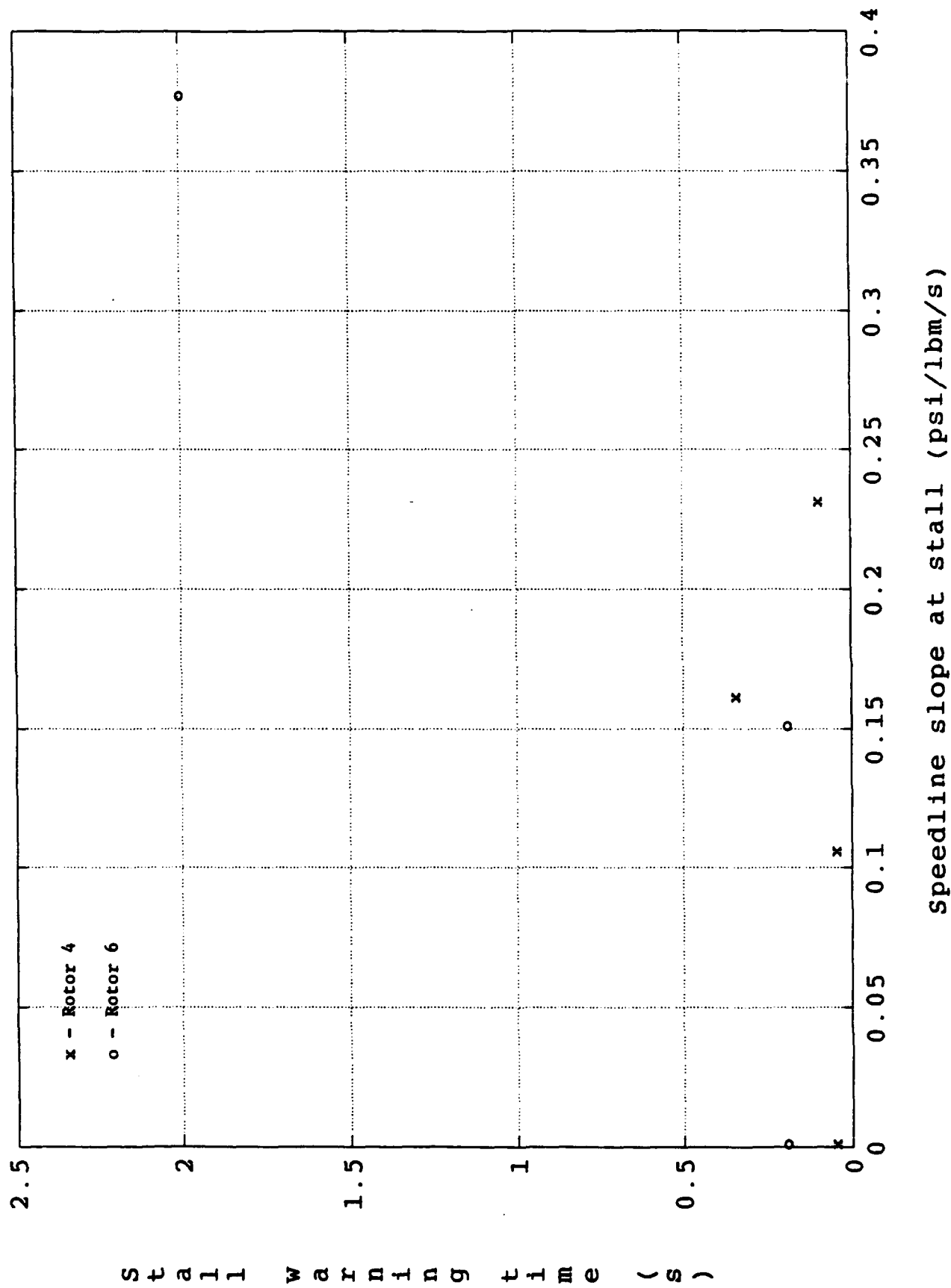
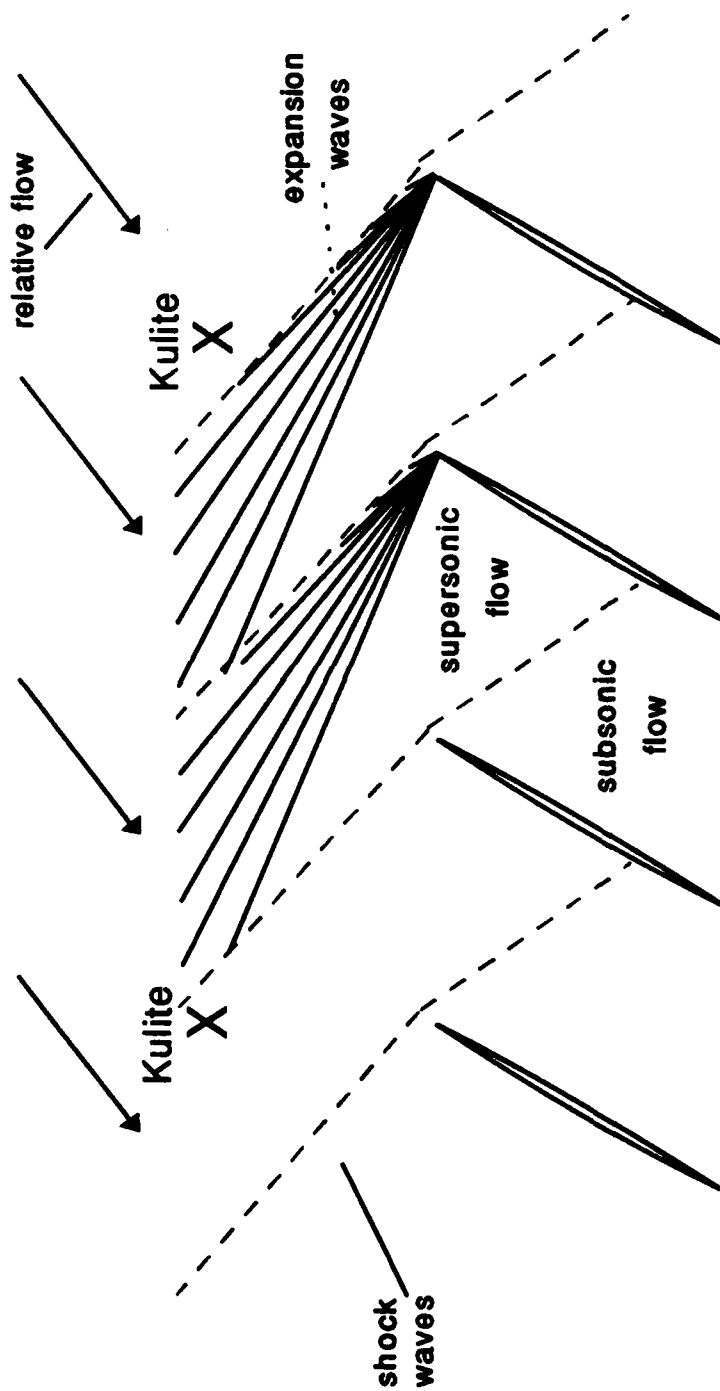


Figure 5.37 Effect of local speedline slope on stall warning time



Notes:

1. drawn to approximately 1/2-scale
2. actual blade tip chord: 3.7 inches
3. distance from leading edge tip to Kulites: 2.5 inches

Figure 5.38 Shock structure in transonic rotors at near-stall

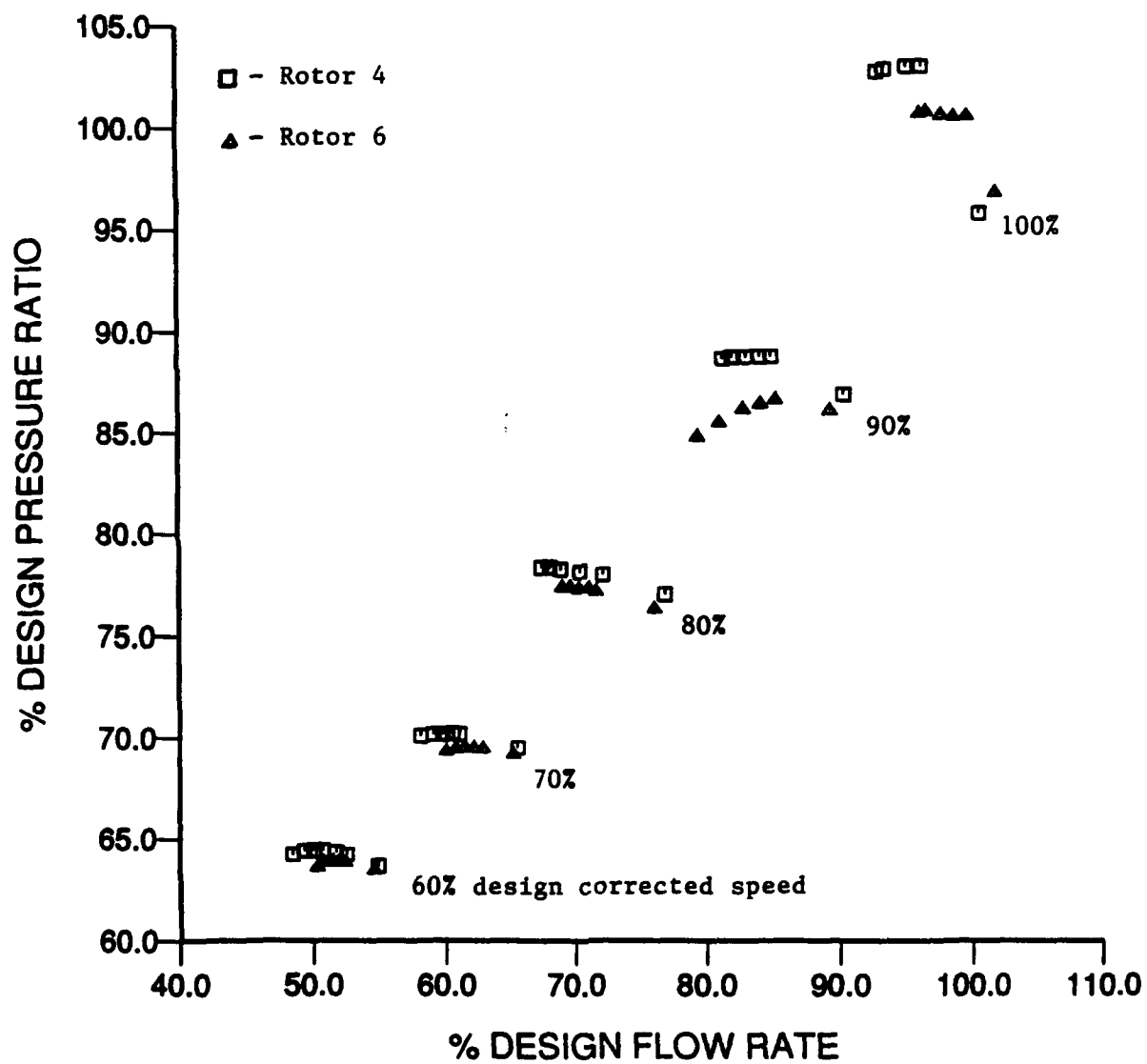


Figure 5.39 Steady-state speedline characteristics of both rotors

Appendix

Fourier Analysis

Fourier analysis plays an important role in the area of digital (or discrete) signal processing. Consequently, in addition to being covered in many mathematics books, the subject of Fourier analysis can be found in virtually all signal processing textbooks. In this appendix, some basic Fourier concepts are reviewed and directly applied to the current work. Detailed discussions of Fourier techniques as they relate to signal processing can be found in the textbooks by Oppenheim and Schaffer [32] and Stearns and Hush [33].

Fourier analysis allows for the study of linear systems based on the representation of discrete and continuous time functions in terms of sinusoids and harmonics (multiples). Consider a periodic function, $f(t)$, composed of components (each with its own amplitude and phase) which are sinusoidal and occur only at harmonics of the fundamental frequency, ω_0 . Then, the function can be represented by a Fourier series in any one of the following three forms:

$$\hat{f}(t) = \frac{a_0}{2} + \sum_{k=1}^K (a_k \cos k\omega_0 t + b_k \sin k\omega_0 t) \quad (\text{A.1})$$

$$= \frac{A_0}{2} + \sum_{k=1}^K A_k \cos(k\omega_0 t + \alpha_k) \quad (\text{A.2})$$

$$= \sum_{k=-K}^K c_k e^{jk\omega_0 t} \quad (\text{A.3})$$

where: k = harmonic number

a 's, b 's, A 's, α 's, c 's = Fourier coefficients¹

j = imaginary unit; $j^2 = -1$

$\omega_0 = 2\pi/T$; T = period

The three expressions are equivalent as evidenced by the relationships between the coefficients given in Table A.1.

Table A.1 Relationships between Fourier Coefficients

Coefficient ($k \geq 0$)	In Terms of:		
	a_k, b_k	A_k, α_k	c_k, c_{-k}
a_k	a_k	$A_k \cos \alpha_k$	$c_k + c_{-k}$ (except $a_0 = 2c_0$)
b_k	b_k	$-A_k \sin \alpha_k$	$j(c_k - c_{-k})$
A_k	$(a_k^2 + b_k^2)^{1/2}$	A_k	$2(c_k c_{-k})^{1/2}$
α_k	$-\tan^{-1} \left(\frac{b_k}{a_k} \right)$	α_k	$\tan^{-1} \left[\frac{\text{Im}(c_k)}{\text{Re}(c_k)} \right]$
c_k	$\frac{1}{2}(a_k - jb_k)$	$\left(\frac{A_k}{2} \right) e^{j\alpha_k}$	c_k
c_{-k}	$\frac{1}{2}(a_k + jb_k)$	$\left(\frac{A_k}{2} \right) e^{-j\alpha_k}$	c_{-k}

¹ $b_0 = \alpha_0 = 0$; Im, imaginary part; Re, real part.

[33]

In the present work, the complex representation is used, mainly for its simplification of the mathematics. The complex Fourier coefficients contain all of the spectra information (distribution of amplitude, phase, power, or energy over frequency) of the signal.

Now, consider the case of the present investigation indicated in Fig. 3.12. The eight transducers are equally spaced around the compressor annulus (45 degrees apart), which implies

¹Also, least-squares coefficients, as Fourier series are an application of least-squares approximations.

the functions comprising the Fourier representation are orthogonal (i.e., the exponentials in Eqn. A.3). In order to determine the presence of modal waves, the Spatial Fourier Coefficients (SFCs) must be computed at each discrete time. The spectra of the sampled signals can then be tracked over the total sample time. The SFCs can be formulated using the solution for least-squares coefficients (Stearns and Hush [33]) to obtain:

$$c_k = \frac{1}{N} \sum_{n=0}^{N-1} p(\theta_n, t) e^{\frac{-j2\pi nk}{N}} \quad (\text{A.4})$$

where: $p(\theta_n, t)$ = unsteady pressure measurement at a particular circumferential location and time

N = number of spatial measurements; $N=8$ here

k = harmonic = $\pm 1, \pm 2, \pm 3^2$

Equation (A.4) represents the discrete Fourier transform (DFT) of a periodic signal. Since the measurements are equally spaced and the measured pressures are real, the special symmetry properties of the DFT can be used; namely, c_k and c_{-k} are complex conjugates. Thus, only c_{-1} , c_{-2} , and c_{-3} need be computed (or the positive harmonics) to determine the desired amplitude and phase information. It is easily seen from Table A.1 that the c_{-k} contain the phase and one-half the amplitude information of each harmonic.

In addition to amplitude and phase, the SFCs can be used to

²Fourier analysis states that in order to compute K harmonics, the number of measurements N must be $2K+1$. Thus, with 8 measurements, only the first 3 harmonics can be resolved.

compute the power spectral densities (PSDs) of each Fourier mode. The PSD of each SFC is proportional to the square of the amplitude of the SFC, $|c_k|^2$. As discussed by Paduano [34], for applications involving analysis of modal waves, care must be taken in interpreting the PSD plots. Because the SFCs are complex and represent a spatial wave, a frequency on a PSD plot can represent a rotation frequency of the wave (which is of interest here) or a frequency of oscillation in wave amplitude. A PSD which is symmetric about zero frequency will represent the latter behavior. Thus, only PSD peaks which do not exist at identical positive and negative frequencies indicate the modal waves. As suggested by Paduano, overlapping the positive and negative frequency plots provides a convenient representation of the PSD.

VITA

Captain Keith M. Boyer was born in Utica, NY on February 21, 1961. He graduated from Notre Dame High School in June 1979 and entered the active duty Air Force on August 23rd of the same year. His first 5 years in the Air Force were spent in the electronic warfare (EW) field, both as a technician and instructor of EW principles and systems. He was selected for the Airman Education and Commissioning Program in 1984, and attended the University of Florida in Gainesville until May 1987 when he graduated with a BS in Aerospace Engineering. A distinguished graduate of Officer Training School, Captain Boyer was commissioned on August 23, 1987. He was assigned to the Aero Propulsion and Power Directorate (APPD) at Wright-Patterson AFB, OH and worked as a program manager/project engineer on several programs in the Compressor Research Facility through May 1991. For his work regarding compressor stall and recovery, he was co-recipient of the 1988 APPD Heron Award, presented annually in recognition of the most significant in-house research achievement. He entered the School of Engineering, Air Force Institute of Technology in May 1991. His follow-on assignment will be at the USAF Academy in Colorado Springs as an Instructor in the Department of Aeronautics.

Permanent Address: 2712 Brighton Place
Utica, NY 13501

REPORT DOCUMENTATION PAGE

Form Approved
OMB No. 0704-0188

Public reporting burden for this collection of information is estimated to average 1 hour per response, including the time for reviewing instructions, searching existing data sources, gathering and maintaining the data needed, and completing and reviewing the collection of information. Send comments regarding this burden estimate or any other aspect of this collection of information, including suggestions for reducing this burden, to Washington Headquarters Services, Directorate for Information Operations and Reports, 1215 Jefferson Davis Highway, Suite 1204, Arlington, VA 22202-4302, and to the Office of Management and Budget, Paperwork Reduction Project (0704-0188), Washington, DC 20503.

1. AGENCY USE ONLY (Leave blank)		2. REPORT DATE December 1992	3. REPORT TYPE AND DATES COVERED Master's Thesis	
4. TITLE AND SUBTITLE CHARACTERIZATION OF STALL INCEPTION IN HIGH-SPEED SINGLE-STAGE COMPRESSORS			5. FUNDING NUMBERS	
6. AUTHOR(S) Keith M. Boyer, Captain, USAF				
7. PERFORMING ORGANIZATION NAME(S) AND ADDRESS(ES) Air Force Institute of Technology, WPAFB OH 45433-6583			8. PERFORMING ORGANIZATION REPORT NUMBER AFIT/GAE/ENY/92D-21	
9. SPONSORING / MONITORING AGENCY NAME(S) AND ADDRESS(ES) William W. Copenhaver WL/POTX, WPAFB OH 45433			10. SPONSORING / MONITORING AGENCY REPORT NUMBER	
11. SUPPLEMENTARY NOTES				
12a. DISTRIBUTION / AVAILABILITY STATEMENT Approved for public release; distribution unlimited			12b. DISTRIBUTION CODE	
13. ABSTRACT (Maximum 200 words) Two single-stage, transonic compressor designs were tested under various undistorted operating conditions to characterize the process leading up to aerodynamic stall. The rig case was instrumented with eight high-response static pressure transducers equally spaced around the annulus for stall development detection. High-response measurements were low-pass filtered and both spatially and temporally analyzed using discrete Fourier techniques. At all speeds tested for both designs, stall inception was characterized by growth of a small amplitude rotating wave. The waves did not grow significantly until just prior to the instability, when exponential growth into fully-developed rotating stall occurred very rapidly, within 6-10 rotor revolutions. The amount of time the rotating waves could be detected prior to stall varied considerably with compressor operating condition and was largely dependent on the local slope of the compressor speedline characteristics. Stall warning times ranged from less than one-tenth of a second to more than two seconds for the same machine operated at different high speeds (above 60% design speed). The influence of compressibility effects are also discussed.				
14. SUBJECT TERMS Compressors, Axial compressors, compressor stall, stall inception, compressor stability, stall warning, transonic compressors			15. NUMBER OF PAGES 155	
			16. PRICE CODE	
17. SECURITY CLASSIFICATION OF REPORT Unclassified	18. SECURITY CLASSIFICATION OF THIS PAGE Unclassified	19. SECURITY CLASSIFICATION OF ABSTRACT Unclassified	20. LIMITATION OF ABSTRACT UL	